8-2019

Medium Mass Nuclei Using Pionless Effective Field Theory in Harmonic Oscillator Basis

Aaina Bansal
University of Tennessee

Medium-mass nuclei using pionless effective field theory in harmonic oscillator basis

A Dissertation Presented for the

Doctor of Philosophy

Degree

The University of Tennessee, Knoxville

FNU Aaina

August 2019

Acknowledgments

I am deeply grateful to my advisor, Professor Thomas Papenbrock, who has been an inspiration throughout the course of my research and studies here at the University of Tennessee; thank you so much for numerous thought provoking discussions, parts of which are spread across this dissertation and will remain with me moving forward.

I am especially thankful to my committee members, Professors Lucas Platter, Robert Grzywacz, and Robert Hinde for their insightful suggestions, and my research collaborators for their time and patience. I am also thankful to Professors Marianne Breinig and Adriana Moreo for their guidance and support. I would like to thank my fellow graduate students and postdoctoral researchers in the nuclear theory group for creating an intellectually stimulating environment which was instrumental to my growth as a graduate student. Special thanks to the staff members in the Physics and Astronomy Department for their perpetual kindness and help during my time at the University.

Last but not the least, I thank my grandparents and parents for always believing in me, even in the times I did not, my brother for being a good friend, and my partner for his unconditional support throughout my studies.

Abstract

This dissertation presents next-to-leading order (NLO) pionless effective field theory (EFT) results for ^{16}O and ^{40}Ca nuclei at a physical $m_{\pi[\mathrm{pi}]} = 140$ MeV and a heavier pion mass $m_{\pi[\mathrm{pi}]} = 806$ MeV. Here, our predictions at heavier pion mass are based on the lattice quantum chromodynamics data for $A = 2, 3$ systems. We find bound ^{16}O and ^{40}Ca nuclei at NLO with binding energies per nucleon are 9-10 MeV and 26-36 MeV at pion masses of 140 MeV and 806 MeV, respectively. The EFT potentials are regulated by finite harmonic oscillator basis. This work discusses the details of our method for three-nucleon contact interactions in addition to the short-ranged nucleon-nucleon potentials in pionless EFT. This approach facilitates many-body calculations due to ultraviolet convergence by construction. We confirm ultraviolet convergence using infrared extrapolations of our results for $A = 3, 4$ nuclei.

This work also presents our progress towards building a nucleon-nucleus EFT potential to study $A + 1$ neighbor of an A-body doubly-magic nucleus by attaching a neutron to an inert core that has structure. The low-energy coefficients of the effective nucleon-nucleus potential are optimized to differential cross sections available for (n, n) scattering processes.

Table of Contents

List of Tables

List of Figures

Chapter 1

Introduction

Neutrons, protons, and mesons are not fundamental particles as they have complicated quark and gluon structures. This dynamics is governed by the true underlying theory of the strong force i.e., Quantum Chromodynamics (QCD). However, it is a non-trivial task to compute nuclear observables beginning from the QCD Lagrangian because the strong coupling among quarks and gluons at low energies makes the problem highly non-perturbative. The increased coupling between gluons and quarks, and the self-coupling among gluons leads to the bound states like nucleons and mesons at low-energies. Thus, a nucleus really consists of many composite states of quarks and gluons interacting with each other.

When the nuclear interaction between nucleons is described in terms of quark and gluon degrees of freedom, the problem can only be solved with a computational technique called lattice QCD. In lattice QCD, the path-integrals are performed for the quark and gluon fields on a discretized four-dimensional grid in Euclidean space-time, where the possible configurations are computed using Monte-Carlo methods. The success of lattice QCD is evident in its results for hadrons. For instance, Fig. 1.1 (from Ref. [24]) shows precision results for hadron masses using lattice QCD, at physical pion mass $m_\pi \approx 140$ MeV, in comparison to the experimental data. Further, the small neutron-proton mass difference of about 1 MeV has also been successfully computed using this technique [18].

When it comes to nuclei, the richness of momentum scales of nuclear physics is not easy to capture using this "bottom-up" approach. To study the two-nucleon system, the lattice should be fine enough to resolve short-range details i.e., the lattice spacing $b_{\rm lat}$ should

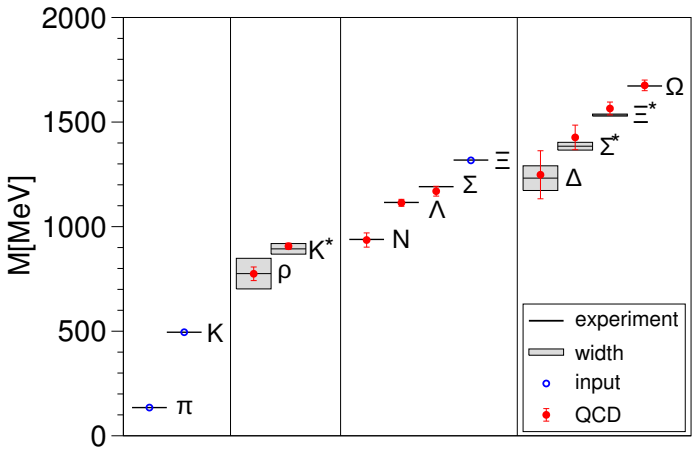

Figure 1.1: (Color online) Precise lattice QCD results for hadron masses reproduce the experimental data at physical pion mass $m_\pi \approx 140$ MeV. N represents nucleons. The vertical lines separate hadrons based on spin-parity J^P. The plot is taken from Ref. [24].

satisfy $b_{\rm lat} M_{\rm QCD} \ll 1$. In addition, the lattice-spatial volumes should be large enough to include the long-range part of the nuclear interaction which is known to be governed by pions i.e., $m_\pi L > 2\pi$ where m_π is the mass of pion, and L is the spatial extent of the lattice. Therefore, often in lattice QCD one uses pions with unphysical mass. The heavier pion masses allow practitioners to work on lattice sizes and spacings that can be realized on current supercomputers. Eventually, the idea is to approach the physical pion mass and use existing theoretical frameworks to extrapolate the lattice QCD results for nuclei to physical m_π. Further, the computational cost grows factorially with the number of nucleons A irrespective of the pion mass. Therefore, the computations of A-nucleon systems beginning from quarks and gluons on a lattice are currently limited to light nuclei (i.e., $A \leq 4$) at unphysical pion mass. Unlike the precise lattice QCD results for hadrons, the lattice QCD results for binding energy of light nuclei have significant uncertainties even at unphysical pion mass (as is also evident in Table 2.1 which shows the lattice QCD results for $A = 2, 3$ nuclei at $m_\pi = 806$ MeV).

Currently, there are two separate lattice QCD approaches to compute nuclei. The first approach uses anisotropic lattice which are longer in the temporal direction to look for plateaus in energy with increasing time in order to find bound states [13, 12, 71, 19]. The second approach, used by the HAL QCD (hadrons to atomic nuclei from lattice QCD)

collaboration, does not rely on looking for plateaus and is based on direct extraction of NN potentials from lattice simulations [43, 2, 1]. These are simply two different methods which should give same physics i.e., similar evolution of multi-nucleon systems with increasing quark masses. Unfortunately, this is not true. While the first approach finds that nuclear binding increases with increasing pion mass [12], the second approach finds that nuclear binding decreases with increasing pion mass [41]. For example, HAL QCD collaboration finds an unbound deuteron [42] at $m_\pi = 806$ MeV, while NPLQCD collaboration (using the first approach) finds an overbound deuteron and also a bound di-neutron [12, 82]. The reason for this difference is not yet understood. In spite of this unresolved conflict, there is an interest in connecting lattice QCD simulations to study nuclei with more number of nucleons (albeit at unphysical pion masses). The physical question of interest is, how will the A-body nuclei, starting from heavier pion mass extrapolate to the corresponding physical nuclei at $m_\pi \approx 140$ MeV. Until lattice QCD simulations for heavier nuclei becomes computationally feasible, there has been an effort of connecting the lattice QCD data to heavier nuclei using existing low-energy nuclear effective field theories (EFTs) and many-body methods as an the alternative approach.

Effective field theories exploit the hierarchy of energy scales in nuclear physics, as shown in Fig. 1.2 (taken from Ref. [15]). The average Fermi momentum (~ 1.35 fm^{-1} or 270 MeV) of protons and neutrons in a nucleus is comparable to the mass of the lightest meson, the pion, $m_\pi \approx 140$ MeV. Further, the two-nucleon system presents another scale due to the weakly bound deuteron (with binding energy ~ 2.2 MeV) and an unbound di-neuteron close to the zero-energy threshold. Thus, the scattering lengths in triplet S ($a_t^{np} \sim 5.4$ fm) and singlet S ($a_s^{np} \sim -23.7$ fm) channels significantly exceed the physical range of the nuclear force. The Fermi momentum and the pion mass are small in comparison to masses of the heavier mesons like ρ, ω ($\sim$ 800 MeV) or the nucleon mass $M_{\rm QCD} \approx 1$ GeV, the energy scale at which the structure of individual nucleons is resolved. Going from top to bottom (high-energy to low-energy) is viewed as decreasing the resolution scale.

Nuclear EFTs provide a theoretical framework to study nuclei starting from neutrons, protons, and pions as the nucleons inside a nucleus are not fast enough to resolve the details of the short-range interactions. Therefore, the short-distance details of the interaction can

be mimicked by a simpler form constrained by symmetries of the underlying theory, QCD. Importantly, it does not mean that low energy processes are insensitive to short-distance dynamics. Instead, EFTs systematically model the unknown details of the short-distance physics into a certain number of low energy constants (LECs) and short-range interactions. LECs are reduced to a finite number by a proper 'power counting'. The power counting in an EFT arranges all possible interactions in the order of their contribution. This contribution decreases according to the powers of Q/Λ as one goes from leading order (LO) to next-to-leading-order (NLO) and so on. Here, Q is the momentum scale of physical interest, and Λ is the breakdown scale of the theory. EFTs also enable uncertainty estimation based on neglected higher-order terms in the potential at any given order. The true advantage of the power counting is that it provides predictive power to the theory. As one can truncate the EFT expansion at a certain order, a finite number of LECs are optimized to low-energy data. Once we have the optimized potential at a particular order, it is input to the many-body methods to predict other low-energy observables along with theoretical uncertainty estimates. The EFT potentials are regularized in momentum space such that the cutoff of the interaction is higher than the breakdown scale of the theory. As the cutoff of the interaction is varied, the LECs "run" (or scale) to account for the effects of additional high-momentum states. This renormalization of the LECs ensures that the low-energy observables are cutoff independent. Thus, studying the cutoff dependence of low-energy observables and their order-by-order convergence in comparison to the experimental data are two ways that are often used to give EFT uncertainty estimates.

In an EFT, the LECs are adjusted to nuclear data at low energies. In contrast, lattice QCD will provide the numerical value of the parameters microscopically. The HAL QCD collaboration used the Brueckner-Hartree-Fock method for solving ^{16}O and ^{40}Ca nuclei with the NN potential extracted directly from lattice simulations at $m_\pi \approx 400$ MeV [41]. To anchor the unresolved short-distance physics in EFTs to the QCD Lagrangian, the NPLQCD data for the deuteron, di-neutron and triton binding energies at $m_\pi = 806$ MeV were used as an input to LO pionless EFT potential to compute nuclei like ^{6}Li [5] and ^{16}O [20]. In this work, we predict binding energy for ^{16}O and ^{40}Ca lattice nuclei, at unphysical pion mass $m_\pi = 806$ MeV, using NPLQCD results for $A = 2, 3$ as input to NLO pionless EFT. We

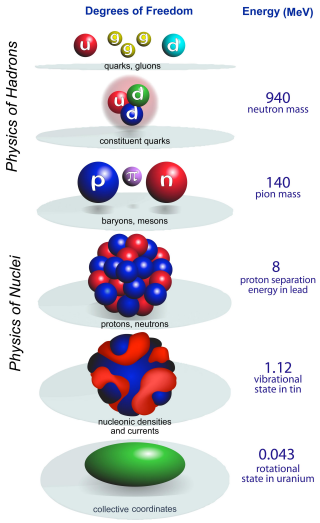

Figure 1.2: (Color online) The separate energy scales in nuclear physics and the relevant degrees of freedom due to reduced resolution with decreasing energy (Figure is taken from Ref. [15]).

also perform the first NLO pionless EFT calculations for the physical ^{16}O and ^{40}Ca nuclei. Throughout this text, by "physical" nuclei we mean nuclei at the physical pion mass.

1.1 Pionless effective field theory

Let us begin with the symmetries of the non-relativistic nucleon-nucleon (NN) interaction. The NN potential depends on the positions, momenta, spin and isospin of the interacting particles, i.e.,

$$V_{NN} = V(\vec{r}_1', \vec{r}_2', \vec{p}_1', \vec{p}_2', \vec{r}_1, \vec{r}_2, \vec{p}_1, \vec{p}_2, \boldsymbol{\sigma}_1, \boldsymbol{\sigma}_2, \boldsymbol{\tau}_1, \boldsymbol{\tau}_2) \tag{1.1}$$

where, the $\vec{r}_{1(2)}, \vec{r}_{1(2)}$ denote the initial position of particle 1(2), and $\vec{r}'_{1(2)}, \vec{r}'_{1(2)}$ denote the final position of particle 1(2). The same representation applies to full momentum space. $\boldsymbol{\sigma}_{1(2)}$ is the spin operator for spin-1/2 nucleon 1(2). Similarly, $\boldsymbol{\tau}_{1(2)}$ is the isospin operator for nucleon 1(2) where isospin projection is $\tau_z = +1/2$ for neutrons and $\tau_z = -1/2$ is for protons. In addition, I define $\vec{p}' = (\vec{p}_1' - \vec{p}_2')$ and $\vec{p} = (\vec{p}_1 - \vec{p}_2)$ as the outgoing and incoming relative momenta, respectively, with $\vec{q} = \vec{p}' - \vec{p}$, $\vec{k} = (\vec{p}' + \vec{p})/2$ being the momentum transfer and the average momentum, respectively.

(i)**Translational invariance:** It implies that interactions only depend on the incoming

and outgoing relative position of the two particles denoted by $\vec{r} = \vec{r}_2 - \vec{r}_1$ and similarly $\vec{r}' = \vec{r}_2 - \vec{r}_1$, respectively and that the total momentum is conserved. Therefore,

$$\begin{aligned} V_{NN} &= V(\vec{r'}, \vec{r}, \vec{p}'_1, \vec{p}'_2, \vec{p}_1, \vec{p}_2, \boldsymbol{\sigma}_1, \boldsymbol{\sigma}_2, \boldsymbol{\tau}_1, \boldsymbol{\tau}_2) \\ &\times \delta^{(3)}(\vec{p}'_1 + \vec{p}'_2 - \vec{p}_1 - \vec{p}_2) \end{aligned} \tag{1.2}$$

(ii) **Galilean Invariance:** Physics should remain independent of the choice of inertial frame of reference (moving with a constant velocity or stationary) i.e., the interaction depends on the initial and final relative momentum. Therefore, we have,
$V_{NN} = V(\vec{r}, \vec{r'}\vec{p'}, \vec{p}, \boldsymbol{\sigma}_1, \boldsymbol{\sigma}_2, \boldsymbol{\tau}_1, \boldsymbol{\tau}_2)$. Note that we treat nucleons non-relativistically as their typical momentum (≈ 270 MeV) is smaller than the nucleon mass $m \approx 1000$ MeV.
(iii) **Rotational Invariance:** It means that nuclear states are eigenstates of total angular momentum operator $\boldsymbol{J}$, which implies the potential might include spin-orbit coupling $\boldsymbol{L} \cdot \boldsymbol{S}$. Here, $\boldsymbol{L}$ is the total orbital angular momentum operator for two nucleons and $\boldsymbol{S}$ is the total spin operator. The total angular momentum partial wave channels are denoted by ${}^{(2S+1)}L_J$.
(iv) **Parity P (or Space reflection symmetry):** The strong force conserves parity i.e., nuclear states are eigenstates with $P = \pm 1$ parity eigenvalues. Thus, the nuclear potential should fulfill, $[\hat{P}, \hat{V}] = 0$.
(v) **Time reversal symmetry:** It requires,
$V(\vec{r}', \vec{r}, \vec{p}', \vec{p}, \boldsymbol{\sigma}_1, \boldsymbol{\sigma}_2, \boldsymbol{\tau}_1, \boldsymbol{\tau}_2) = V(\vec{r}', \vec{r}, -\vec{p}', -\vec{p}, -\boldsymbol{\sigma}_1, -\boldsymbol{\sigma}_2, \boldsymbol{\tau}_1, \boldsymbol{\tau}_2)$ allows only terms with total even number of $\vec{p}$ and $\boldsymbol{\sigma}$'s are allowed.
(vi) **Hermiticity:** To ensure real eigenvalues, Hamiltonian should be Hermitian. Therefore, $V = V^\dagger$, where $\dagger$ represents conjugate transpose of the matrix. Apart from the above symmetries, similarities between the spectrum of mirror nuclei show that isospin charge symmetry is also a good approximation i.e., nuclear potential does not distinguish between neutrons and protons.

One can use the symmetries given above to write the most general combination of operators (for scalar, vector and tensor terms) that are allowed [69],

$$\begin{aligned}\{ \quad & \mathbb{I}_{\text{spin}}, \boldsymbol{\sigma}_1 \cdot \boldsymbol{\sigma}_2, (\boldsymbol{\sigma}_1 \cdot \vec{q})(\boldsymbol{\sigma}_2 \cdot \vec{q}), (\boldsymbol{\sigma}_1 \cdot \vec{k})(\boldsymbol{\sigma}_2 \cdot \vec{k}), \boldsymbol{\sigma}_1 \cdot (\vec{q} \times \vec{k}), \boldsymbol{\sigma}_2 \cdot (\vec{q} \times \vec{k}), (\boldsymbol{\sigma}_1 + \boldsymbol{\sigma}_2) \cdot (\vec{q} \times \vec{k})\} \\ \otimes \quad & \{\mathbb{I}_{\text{isospin}}, \boldsymbol{\tau}_1 \cdot \boldsymbol{\tau}_2\} \end{aligned} \tag{1.3}$$

This procedure ensures that the underlying physics, actually responsible for the these symmetries, is accounted for in our model.

In nuclear physics, the scattering lengths of the S-wave channels are much larger than the physical range $R \approx \hbar/(m_\pi c)$ of the potential (m_π is the pion mass). The scattering of the triplet channel ${}^3S_1$ channel which corresponds to the deuteron (^{2}H) is ${}^{np}a_t = 5.42$ fm equivalent to the momentum scale $1/{}^{np}a_t \sim 36$ MeV, and the singlet channel ${}^1S_0$ (neutron-proton) scattering length is ${}^{np}a_s = -23.71$ fm corresponding to the momentum scale $1/{}^{np}a_s \sim -8.3$ MeV. These momentum scales are much lower than the physical pion mass $m_\pi = 140$ MeV, and the nucleon mass scale $M_{\text{QCD}} \approx 1$ GeV. The reason for such a disparity between S-wave scattering lengths and the QCD scale is not yet understood. In pionless EFT, we treat it as a fact of life and use the separation of scales to our advantage; as nucleons are too slow to resolve pions, one has freedom in describing the low-energy nucleon-nucleon (NN) potential. Therefore, we can approximate this short-range potential as a delta function and its derivates (only even derivatives are allowed by time-reversal symmetry) i.e.,

$$V(\vec{r}) = A_0 \delta^{(3)}(\vec{r}) + A_2(\delta^{(3)}(\vec{r})\vec{\nabla}^2 + \vec{\nabla}^2\delta^{(3)}(\vec{r}) + A_2'\vec{\nabla}\delta^{(3)}(\vec{r})\vec{\nabla} + \ldots), \tag{1.4}$$

where ellipses refer to other derivative terms. As higher partial derivates are zero at $r = 0$, the first term corresponds to S-wave channel. The Fourier transform of Eqn. (1.4) yields,

$$V(k', k) = C_0 + C_1'(\vec{p}^2 + \vec{p}'^2) + C_2'\vec{p}' \cdot \vec{p} + \ldots \tag{1.5}$$

The terms from derivates of delta function and the parameters $C_0, C_2', \ldots$ capture the effects of higher-energy processes, details of which are irrelevant because even pions are too heavy

to be resolved. Thus, using Eqns (1.3) and (1.5), the potential for spin-1/2 fermions and isospin symmetric nucleons can be written as,

$$\begin{aligned} V_{NN}(\vec{p}',\vec{p}) = & \, C_0 + \tilde{C}_0 \vec{\sigma_1}\cdot\vec{\sigma_2} \\ & + \mathrm{C}_1 q^2 + \mathrm{C}_2 k^2 \\ & + (C_3 q^2 + C_4 k^2)\vec{\sigma_1}\cdot\vec{\sigma_2} \\ & - iC_5 \frac{\vec{\sigma_1}+\vec{\sigma_2}}{2}\cdot\left(\vec{q}\times\vec{k}\right) \\ & + C_6(\vec{\sigma_1}\cdot\vec{q})(\vec{\sigma_2}\cdot\vec{q}) \\ & + C_7(\vec{\sigma_1}\cdot\vec{k})(\vec{\sigma_2}\cdot\vec{k}) + \ldots \end{aligned} \tag{1.6}$$

Note that certain combinations do not appear. For instance, in the zeroth order term in relative momentum k we do not include the other terms that have operator structures $(\boldsymbol{\tau}_1\cdot\boldsymbol{\tau}_2), (\boldsymbol{\sigma}_1\cdot\boldsymbol{\sigma}_2)(\boldsymbol{\tau}_1\cdot\boldsymbol{\tau}_2)$, because antisymmetry makes them redundant. The partial-wave decomposition of the potential (1.6) yields [28],

$$\begin{aligned} V_{NN}({}^3S_1) &= \tilde{C}_{{}^3S_1} + C_{{}^3S_1}(p^2+p'^2) + \ldots \\ V_{NN}({}^1S_0) &= \tilde{C}_{{}^1S_0} + C_{{}^1S_0}(p^2+p'^2) + \ldots \\ V_{NN}({}^3S_1 - {}^3D_1) &= C_{{}^3S_1-{}^3D_1} p^2 + \ldots \\ V_{NN}({}^3D_1 - {}^3S_1) &= C_{{}^3S_1-{}^3D_1} p'^2 + \ldots \\ V_{NN}({}^1P_1) &= C_{{}^1P_1} pp' + \ldots \\ V_{NN}({}^3P_2) &= C_{{}^3P_2} pp' + \ldots \\ V_{NN}({}^3P_1) &= C_{{}^3P_1} pp' + \ldots \\ V_{NN}({}^3P_0) &= C_{{}^3P_0} pp' + \ldots \\ &+ \ldots \end{aligned} \tag{1.7}$$

Ellipses in each partial wave represent contributions from higher order derivative terms in Eqn. (1.6), that will also introduce other partial-wave channels like ${}^1D_2$,${}^3P_2 - {}^3F_2$ and so on.

The problem with Eq. (1.5) is its infinite number of terms. This low-energy approximation is useful only if we can can truncate it to a finite number of terms. This is where the power counting scheme in EFT enters.

Kaplan, Savage, and Wise (KSW) developed the power counting scheme for using contact interactions in NN systems [46] with unnaturally large scattering lengths in the singlet and triplet S partial-wave channels. They studied the size of coupling coefficients by regularizing the potential to find systematic expansion for the S-wave NN scattering amplitudes,

$$T = \frac{4\pi}{m} \frac{1}{p\cot\delta_l - ip} \tag{1.8}$$

such that the low-energy expansion of $p\cot\delta$ (also known as the effective range expansion),

$$p\cot\delta = -\frac{1}{a} + \frac{1}{2} r_e p^2 + \ldots, \tag{1.9}$$

in the limit $pR \ll 1$ is reproduced while maintaining $ap \sim 1$ to all orders i.e, the S-wave scattering amplitudes, has an expansion of the form,

$$T = -\frac{4\pi}{m} \frac{1}{1/a + ip} \left[1 + \frac{r_e/2}{1/a + ip} p^2 + \frac{r_e/2}{(1/a + ip)^2} p^4 + \ldots \right], \tag{1.10}$$

where a, r_e and δ denote the scattering length, effective range and phase shifts, respectively. The effective range expansion shows that the scattering cross-section at very low energies is independent of the details of the potential at short distances, and only depends on the S-wave scattering length a, which in the case of NN systems, is much larger than the physical range R of the potential. It turns out that the LO contribution comes from the potentials,

$$\begin{aligned} V_{NN}^{\rm LO}({}^1S_0) &= \tilde{C}_{{}^1S_0}, \\ V_{NN}^{\rm LO}({}^3S_1) &= \tilde{C}_{{}^3S_1}, \end{aligned}$$

with NLO corrections that are also only S-wave terms,

$$\begin{aligned} V_{NN}^{\rm NLO}(^1S_0) &= C_{^1S_0}(p^2+p'^2), \\ V_{NN}^{\rm NLO}(^3S_1) &= C_{^3S_1}(p^2+p'^2). \end{aligned} \tag{1.11}$$

The remaining terms in Eqn. (1.7) only enter at next-to-next-to-leading order (N2LO) or other higher orders. The convergence of this series depends on the parameter $\alpha_{\rm EFT} = r_e/a$. For physical two-nucleon system, the parameter $\alpha_{\rm EFT}$ is roughly 0.3. Thus, the pionless EFT can be used to reproduce the NN binding energy as well as phase shifts at low energies. Pionless EFT potential reproduces the scattering length a at LO, and the effective range r_e along with a at NLO.

Lattice QCD calculations show that scattering length a is almost twice the effective range r_e at the unphysical pion mass $m_\pi \approx 806$ MeV [82, 11]. Thus, pionless EFT can be applied to the two-nucleon system at this pion mass as well, with uncertainty estimates given by $\alpha_{\rm EFT} \approx 0.5$.

Three nucleon-systems are not renormalized when computed using a LO NN potential. Thus, a three nucleon contact force NNN is required at LO [14]. The order at which three-body forces enter depends on the resolution scale built into an EFT. For instance in chiral EFT, where pion degrees of freedom are included, the first three-body forces is needed at N2LO in the EFT expansion. Three-body forces or any many-body forces are essentially a consequence of omitted high-energy degrees of freedom.

There are several equivalent ways to write the three nucleon contact [80, 27], and we use

$$V_{\rm cont}^{\rm 3NF} = \frac{c_E}{F_\pi^4 \Lambda_\chi} \sum_{j\neq i} \vec{\tau}_i \cdot \vec{\tau}_j. \tag{1.12}$$

For our convenience we make c_E dimensionless using $\Lambda_\chi = 700$ MeV and $F_\pi = 92.4$ MeV constants (as done in chiral EFT). To conclude, the full LO interaction is

$$V_{\rm LO} = V_{NN}^{\rm LO}(^1S_0) + V_{NN}^{\rm LO}(^3S_1) + V_{\rm cont}^{\rm 3NF}. \tag{1.13}$$

Our full NLO potential consists of LO potential (1.13) added to terms in Eq. (1.11). Recently, Bazak et al.[9] found that an additional four-body force is needed at NLO to renormalize the systems, consisting of upto six bosons, with increasing cutoff of the short-range EFT interactions. This was not known at the time of our research and our LO and NLO calculations of the medium-mass nuclei only include the three-body contact force (1.12).

We include the Coulomb interaction non-perturbatively at the level of single photon exchange i.e., $\alpha_{\rm em}/r$. Here, $\alpha_{\rm em}$ is the fine structure constant and r is the radial distance between the two interacting protons. We note that the additional electromagnetic corrections that enter up to NLO (as discussed in Refs. [51, 81]) are not included in our calculations.

1.1.1 Pionless EFT in few and many-body systems

The large scattering length of the two-body systems leads to universal properties in the few-body systems. Here, 'universal' means that the properties are independent of the specific form of the two-body potential. The two-body binding energy E_2 is correlated to the large positive scattering length a,

$$E_2 = \frac{\hbar^2}{ma^2} + \mathcal{O}(r_e/a) \tag{1.14}$$

For instance in nuclear physics, this holds true for loosely bound deuteron.

The separation of scales between a and r_e also leads to universal properties in the few-body systems with more than two particles. The three-body bound states show the existence of universal ratio of binding energies of the successive states as the underlying two-body scattering length $a \to \pm\infty$, also known as the Efimov effect [25]. While the ratio between the energies of successive three-body states is universal, one needs a three-body parameter to fix the energy. For instance, the three-nucleon contact with LEC $c_{\rm E}$ is adjusted to the triton binding energy. So, the three-body observables at low-energies are governed by the triplet and singlet S scattering lengths and the three-body parameter $c_{\rm E}$ (upto corrections (r_e/a)).

There also exists an approximate linear correlation between three and four-nucleon systems called the Tjon line [78], if both systems are studied using only nucleon-nucleon interaction. Thus, Platter et al.[73] argued that the alpha-particle binding energy can also

be predicted using LO pionless EFT at leading order with an uncertainty of $\mathcal{O}(r_e/a)$. For moderate cutoffs, the binding energy of the physical ^{4}He nucleus has been shown to have order-by-order convergence using pionless EFT potential as one goes from LO to NLO [47, 57] (where the convergence of the results with respect to experimental order is governed by $\alpha_{\rm EFT} = \mathcal{O}(r_e/a)$).

The heaviest nucleus that has been computed using LO pionless EFT is ^{16}O [20]. The pionless EFT approach was extended to ^{16}O based on the reasoning that the binding energy per nucleon in this nucleus ($\approx$ 8 MeV) is comparable to the binding energy per nucleon in ^{4}He nucleus ($\approx$ 7 MeV) and, that the resultant momentum scale is smaller than the pion mass. The ^{16}O nucleus at the physical and the unphysical pion mass (m_π = 806 MeV) using LO pionless EFT potentials was found to be unbound with respect to decay into alpha particles [20]. However, the ground state of the physical ^{16}O nucleus was noted to be within 30% of the experimental data. We note that the Fermi momentum of nucleons in physical nuclei is 1.35 fm^{-1} (or 270 MeV), roughly three-fourths of the momentum ($\Lambda \approx \sqrt{m m_\pi} \sim$ 370 MeV) required for non-relativistic nucleons to resolve pions. This yields an $\alpha_{\rm EFT} \approx 0.75$ which is smaller than one. Therefore, the results for medium-mass nuclei can systematically improve with addition of higher order pionless EFT potentials.

1.2 Scope of this work

Our goal was to compute nuclei such as ^{16}O and ^{40}Ca with NLO pionless EFT potential and study the cutoff dependence of these results. For lattice nuclei, these calculations connected lattice QCD data from NPLQCD collaboration to ^{16}O and ^{40}Ca nuclei at unphysical pion mass $m_\pi = 806$ MeV.

The NLO terms in the potential can be added perturbatively or non-perturbatively. In a perturbative treatment the NLO terms are added as a first-order perturbation to the solution of Schrödinger equation at leading order, and then the low-energy coefficients are adjusted to the effective range r_e in the effective range expansion (1.9). On the contrary in a non-perturbative treatment, the LO LECs are re-optimized along with the added NLO LECs such that the scattering length a and the effective range r_e are reproduced. We solved the

NLO potential with a non-perturbative method, as done previously in Refs. [50, 57]. The reason is as follows.

With the LO pionless EFT potential, all physical nuclei heavier than ^{4}He that have been computed till now (like ^{6}Li [76] and ^{16}O [20]), are found to be unbound with respect to α-particle emission. Therefore, a perturbative addition of NLO terms might make the A-body ground state energy more negative, but only because of increased binding of individual α clusters in that A-body system. Thus, we believe no finite-order perturbation theory will yield an A-body bound-state wave function that is exponentially decaying in the relative coordinate connecting the α clusters. Therefore, we think it is necessary to include the NLO terms non-perturbatively. The non-perturbative treatment of NLO terms limits us to moderate UV cutoffs (as also seen in Ref. [57]). As we shall see later, at NLO we no longer reproduce effective range r_e for interaction cutoffs larger than 650 MeV at physical pion mass.

The application of pionless EFT in nuclei as heavy as ^{40}Ca is made possible using the finite harmonic oscillator basis as the regulator for pionless EFT potentials. We call this approach oscillator EFT. The harmonic oscillator basis is widely used in many-body calculations because it provides an approximate mean-field in the nuclear shell model and is commensurate with symmetries of the atomic nucleus. We build on the method used in Ref. [16] in which chiral EFT was implemented in the harmonic oscillator basis using discrete variable representation of finite harmonic oscillator basis in momentum space. In chapter 2, we begin by reviewing the key ingredients of the approach in Ref. [16] and its limitations in the context of pionless EFT. Further, we extend the method to replace conventionally used momentum-space regulators with the finite oscillator space regulators to regulate EFT interactions, and describe the procedure used for optimization of the LECs. In addition, we discuss the effects of truncating the harmonic oscillator basis on the three-nucleon contact and its significance with respect to many-body calculations. In chapter 3, we study $A = 3, 4$ nuclei and compare our oscillator EFT results to previous works as a benchmark for our approach. We also discuss explanation for Tjon correlations using oscillator EFT framework and the infrared extrapolations of our results for $A \leq 4$ nuclei. We present our results for medium-mass nuclei at the physical and heavier pion mass using NLO pionless EFT potential

in chapter 4. In chapter 5, our method and challenges in developing nucleon-nucleus EFT are presented. There is a discussion of key results and the scope for future improvements at the end of each chapter, and the combined summary of this dissertation is presented in chapter 6.

1.2.1 My contribution

This dissertation is based on the publications [3] and [29]. In the first publication, I provided two- and three-body matrix elements regulated by the finite harmonic oscillator model space, optimized the two-body potentials to data, studied the effects of truncation of the three-body basis on the three-nucleon contact, and wrote the first draft of our paper.

The second publication studies the low-momentum scale of the A-nucleon system that governs infrared extrapolations of its ground-state properties. My contribution to this work was to find the relation between the separation energy of the lowest energy break-up channel and the parameter k_∞ in the infrared extrapolation formula for binding energy.

Chapter 2

Pionless EFT in harmonic oscillator basis

2.1 Motivation

A complete harmonic oscillator basis contains an infinite number of basis states. Numerical implementation of a many-body problem in the oscillator basis thus requires a cut on the number of oscillator states used. Consequently, the finite spherical harmonic oscillator is parameterized not only by the spacing $\hbar\omega$ between consecutive oscillator states, but also by the maximum excitation energy level $N = (2n + l)$, where n and l are the radial and angular momentum quantum numbers, respectively. The finite oscillator basis imposes effective radial hard-wall boundary conditions at

$$L = \sqrt{2(N + 3/2 + 2)}b \tag{2.1}$$

in the position space [66] and at

$$\Lambda = \sqrt{2(N + 3/2 + 2)}\hbar/b \tag{2.2}$$

in the momentum space [52]. Thus, covering only limited phase space as shown in Fig. 2.1. Here,

$$b = \sqrt{\hbar/(\mu\omega)} \tag{2.3}$$

is the oscillator length and $\mu = m/2$ is the reduced mass of the two-nucleon system. Qualitatively, L can be understood to be the classical turning point and Λ as the momentum corresponding to maximum kinetic energy for a particle of mass μ in energy eigenstate $(N+3/2)\hbar\omega$ [21]. For systems with more than two fermions, Eqns. (2.1) and (2.2) need small corrections which depend on choice of reference frame i.e., the center-of-mass frame [84] or laboratory frame [31]. Nonetheless, the key idea is to equate the lowest eigenvalue of the total kinetic energy operator of A-fermion system in an infinite-spherical well of size L and in the finite oscillator model space. The case in point is that the oscillator basis truncation, done due to computational limits, introduces additional ultraviolet cutoff Λ and an infrared cutoff $\hbar/L$.

In view of the observables computed in finite oscillator basis, the infrared cutoff modifies the tail of the bound-state wave function by enforcing it to be zero at L, and the ultraviolet cutoff limits the nuclear interaction to momentum states below Λ which often cuts off the tail of the momentum-space regulated EFT potential. Therefore, the value of any observable O in the limit $L, \Lambda \to \infty$ can be written as

$$O_\infty = O_L + \Delta O_{\rm IR} + \Delta O_{\rm UV}, \tag{2.4}$$

where, O_L is the result for that observable in the model space with infrared cutoff L and $\Delta O_{\rm IR(UV)}$ represent finite-volume effects due to limited extent of the basis in position (momentum) space.

The infrared extrapolation formulas for observables like the binding energy and the radius in Refs. [66, 34] allows one to use calculations done in finite harmonic oscillator basis to obtain infinite-volume results. In principle, these extrapolations are finite spherical well analogue to Lüscher formula [61] which only corrects for the asymptotic tail of a bound-state wave function. Thus, for the infrared extrapolations to work one needs to minimize ultraviolet corrections first.

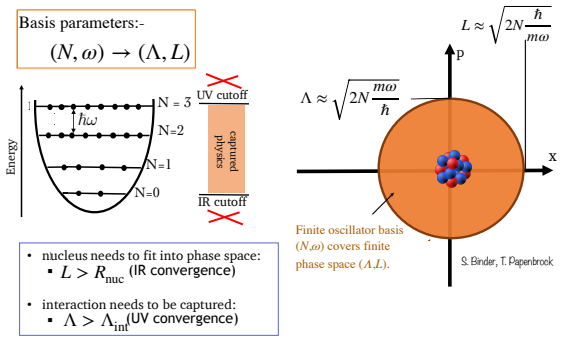

Figure 2.1: (Color online) A finite harmonic oscillator basis introduces an effective hard-wall boundary condition in position and momentum space marked by L and Λ, respectively; both of which are functions of oscillator basis parameters - N and ω. To minimize finite-volume effects, the basis parameters are chosen such that L is larger than the radius $R_{\rm nuc}$ of the nucleus, and Λ is larger than the cutoff $\Lambda_{\rm int}$ of the conventional momentum-space regulators for EFT interactions (to ensure infrared (IR) and ultraviolet (UV) convergence, respectively). In oscillator EFT, $\Lambda_{\rm int} \equiv \Lambda$ by construction. This ensures UV convergence by construction. Figure is made in collaboration with S. Binder and T. Papenbrock.

In our approach we use the finite harmonic oscillator basis to regulate EFT potentials. The main idea is that we tailor the EFT interaction to finite oscillator basis used in many-body methods. This ensures ultraviolet convergence of the observables by construction and gives $\Delta O_{\rm UV} = 0$ in Eqn. (2.4). In what follows, I describe the use of finite spherical oscillator basis in relative coordinates to regulate pionless EFT interactions. It is a two-step process. First, we express the finite oscillator space as lattice of discrete momenta which form its momentum space discrete variable representation (DVR). Next, we use the known properties of DVR to our advantage to regulate the interaction using oscillator basis.

2.2 Discrete variable representation for harmonic oscillator basis

The momentum eigenstates in finite oscillator basis $(N, \hbar\omega)$ are formed by linear combination of all harmonic oscillator states with $2n + l \leq N$. At angular momentum l, we denote the maximum radial quantum number by $N_l = (N - l)/2$. The radial wave function $\langle r, l|n, l\rangle$ of

energy eigenstate $|n,l\rangle$ of spherical harmonic oscillator is,

$$\psi_{n,l}(r) = (-1)^n \sqrt{\frac{2n!}{\Gamma(n+l+3/2)b^3}} \left(\frac{r}{b}\right)^l e^{-\frac{1}{2}\frac{r^2}{b^2}} L_n^{l+\frac{1}{2}}\left(\frac{r^2}{b^2}\right) \tag{2.5}$$

whereas in momentum space the basis function, $\langle k,l|n,l\rangle$, has the form,

$$\tilde{\psi}_{n,l}(k) = \sqrt{\frac{2n!b^3}{\Gamma(n+l+3/2)}} (kb)^l e^{-\frac{1}{2}k^2b^2} L_n^{l+\frac{1}{2}}(k^2b^2) \tag{2.6}$$

Here, $L_n^{l+1/2}$ denotes the associated Laguerre polynomial and b is the oscillator length.

For a free particle the radial wave function of momentum $\vec{k}$ in spherical basis is proportional to spherical Bessel function, i.e.,

$$\langle r,l|k,l\rangle = \sqrt{2/\pi} j_l(kr). \tag{2.7}$$

On the other hand, the completeness relation of the oscillator states yields,

$$\langle r,l|k,l\rangle = \sum_{n=0}^{\infty} \tilde{\psi}_{n,l}(k)\psi_{n,l}(r). \tag{2.8}$$

In a finite oscillator basis, the momentum operator $\hat{p}$ has a discrete set of momentum eigenstates of the form,

$$|\phi_{\mu,l}\rangle = c_{\mu,l} \sum_{n=0}^{N_l} \tilde{\psi}_{n,l}(k_{\mu,l})|n,l\rangle \tag{2.9}$$

where $c_{\mu,l}$ represents normalization constant (dependent on discrete momentum eigenvalues $k_{\mu,l}$) to ensure that the discrete momentum eigenstates $|\phi_{\mu,l}\rangle$ are orthogonal.

Binder et al.[16] showed that in each angular momentum l the roots of Laguerre polynomial $L_{N_l+1}^{l+1/2}(k^2b^2)$ are eigenstates of momentum squared operator $\hat{p}^2$ in the finite harmonic oscillator consisting of states $n = 0, 1..., N_l$ with

$$c_{\mu,l} = \frac{k_{\mu,l}b}{\sqrt{(N_l+1)(N_l+l+3/2)\tilde{\psi}_{N,l}(k_{\mu,l})}}, \tag{2.10}$$

form a DVR [60, 58] of the finite oscillator basis in momentum space. DVR by definition is a complete basis of orthogonal states for which probability is localized around the eigenvalue that it represents and have nodes at the remaining DVR points, i.e.,

$$\langle \phi_{\mu,l} | k_{\nu,l} \rangle = \delta^{\nu}_{\mu} c^{-1}_{\mu,l} \tag{2.11}$$

and the discrete eigenfunctions $\phi_{\mu,l}(k)$ can be expressed as

$$\tilde{\phi}_{\mu,l}(k) = \langle k, l | \phi_{\mu,l} \rangle = \frac{k_{\mu,l}/b}{k^2_{\mu,l} - k^2} \tilde{\psi}_{N_l+1,l}(k). \tag{2.12}$$

Figure 2.2 shows that momentum eigenstates of finite oscillator basis in the above equation form a DVR. For a detailed description of DVRs, we refer the reader to the reviews [60, 58], and some original works in quantum chemistry [38, 22, 59] and nuclear physics [7].

2.2.1 Oscillator DVR to regulate short-range interactions

Our goal is to ensure that the NN interaction in momentum space is spanned by a finite oscillator basis used in many body calculations, so that we can ensure ultraviolet convergence by construction. As we show in the following sections (see red-dashed lines in Figs. 2.3, 2.5 for example), simple projection of the original momentum-space interaction onto finite oscillator basis introduces oscillations. This effect was first noted in Ref. [16]. It is not surprising because high-energy oscillator states, that are removed, are energy and not momentum eigenstates which mix low- and high-momentum physics. This leads to significant differences between DVR interaction and $V(k', l'; k, l)$ at all momenta other than the DVR points. For instance, oscillations will invariably alter the behavior of the projected interaction at momenta smaller than the infrared cutoff $k_{0,l}$ of the finite oscillator basis in partial wave l.

Because of the DVR property in Eq. (2.11), the interaction $\hat{V}_{\rm DVR}$ in DVR basis is,

$$\langle \phi_{\mu,l'} | \hat{V}_{\rm DVR} | \phi_{\nu,l} \rangle = c_{\mu,l'} c_{\nu,l} \langle k_{\mu,l'}, l | \hat{V} | k_{\nu,l}, l \rangle \tag{2.13}$$

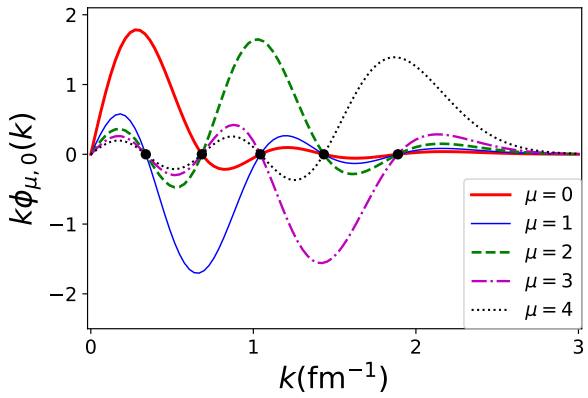

Figure 2.2: (Color online) The S-wave discrete momentum eigenfunctions $\phi_{\mu,0}(k)$ [plotted as $k\phi_{\mu,0}(k)$] for $\mu = 0, 1, ...N_0$, shown as a function of momentum for a finite harmonic oscillator basis with $N = 8$, $\hbar\omega = 22$ MeV. The solid black dots on the x-axis indicate the discrete momentum eigenvalues.

where, $V(k', l'; k, l) \equiv \langle k'l'|\hat{V}|k, l\rangle$ is the partial-wave momentum-space interaction matrix element. We note that the DVR interaction matrix elements $\langle k_{\mu,l'}, l'|\hat{V}_{\rm DVR}|k_{\nu,l}, l\rangle$ are equal to the original interaction $V(k_{\mu,l'}, l'; k_{\nu,l}, l)$ on DVR points $(k_{\mu,l'}, k_{\nu,l})$ with $\mu = 0, ..., N_{l'}$ and, $\nu = 0, ..., N_l$.

The DVR interaction $\hat{V}_{\rm DVR}$ projects the interaction to the finite oscillator basis where interaction matrix element in the finite oscillator space is

$$\begin{aligned}\langle n', l'|\hat{V}_{\rm DVR}|n, l\rangle &= \sum_{\mu=0}^{N_{l'}}\sum_{\nu=0}^{N_l}\langle n', l'|\phi_{\mu,l'}\rangle\langle\phi_{\mu,l'}|\hat{V}_{\rm DVR}|\phi_{\nu,l}\rangle\langle\phi_{\nu,l}|n, l\rangle \\ &= \sum_{\mu=0}^{N_{l'}}\sum_{\nu=0}^{N_l} c^2_{\mu,l'}c^2_{\nu,l}\tilde{\psi}_{n',l'}(k_{\mu,l'})\tilde{\psi}_{n,l}(k_{\nu,l})V(k_{\mu,l'}l'; k_{\nu,l}l),\end{aligned} \tag{2.14}$$

and reduce to zero in case of oscillator states with principal quantum numbers $n', n > N_{l'}$. In the upcoming discussion, to study the effect of DVR projection on infrared behavior of

the original interaction, we use the DVR interaction matrix element in momentum space,

$$\begin{aligned}\langle k', l'|V_{\rm DVR}|k, l\rangle &= \sum_{\mu=0}^{N_l}\sum_{\nu=0}^{N_{l'}}\langle\phi_{\nu,l'}|\hat{V}_{\rm DVR}|\phi_{\mu,l}\rangle\tilde{\phi}_{\nu,l'}(k')\tilde{\phi}_{\mu,l}(k) \\ &= \sum_{\mu=0}^{N_l}\sum_{\nu=0}^{N_{l'}} c_{\mu,l}c_{\nu,l'}\tilde{\phi}_{\nu,l'}(k')\tilde{\phi}_{\mu,l}(k)V(k'_{\nu,l'}, l'; k_{\mu,l}, l). \end{aligned} \tag{2.15}$$

In what follows we develop a method we call 'IR improvement', to improve the infrared behavior of the DVR interaction. In our approach, we demand the DVR interaction to be correct at $k = 0$ by losing the agreement with the original interaction at highest DVR point. We describe the infrared improvement for some short-range potential terms that are integral to nuclear EFTs.

2.2.2 Leading order NN contact

Let us consider the case of unregulated NN contact interaction in momentum space,

$$V(k', l' = 0; k, l = 0) = C_{\rm LO}v(k)v(k'), \tag{2.16}$$

where $C_{\rm LO}$ is the coupling strength and $v(k) = 1$. The contact interaction is active only in S-partial wave because higher partial waves have zero contribution for delta potential. The corresponding DVR interaction is

$$\langle k', 0|V^{\rm IR}_{\rm DVR}|k, 0\rangle = C_{\rm LO}v_{\rm DVR}(k')v_{\rm DVR}(k) \tag{2.17}$$

with

$$v_{\rm DVR}(k) \equiv \sum_{\mu=0}^{N_0} c_{\mu,0}\tilde{\phi}_{\mu,0}(k). \tag{2.18}$$

Figure 2.3 shows $v(k) = 1$ as the horizontal dashed-dotted line, and its DVR projection $v_{\rm DVR}$ as the dashed red line. Clearly, the DVR interaction differs from the original potential (2.16). As expected for a DVR, $v_{\rm DVR}$ coincides with the original function $v(k)$ only at the discrete DVR momenta shown as solid dots. The vertical dotted line indicates

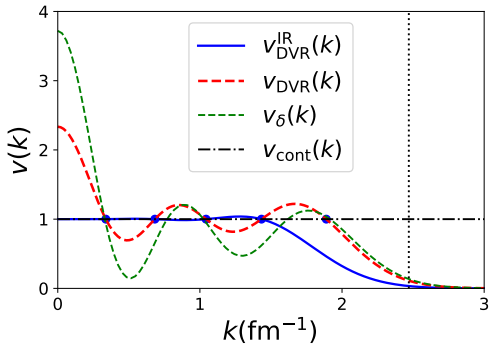

Figure 2.3: (Color online) The solid blue (red dashed) curve shows the DVR projection with (without) infrared improvement in comparison with the original function $v(k) = 1$ shown as a dashed-dotted black line. For reference, the thin green dashed curve shows the contact (i.e. a δ-function in position space) projected to finite harmonic oscillator basis $N = 8, \hbar\omega = 22$ MeV, $l = 0$. The solid blue dots represent the DVR momenta and the dotted black line marks the ultraviolet cutoff introduced by finite oscillator space.

the ultraviolet cutoff in Eq. (2.2) and is the cutoff of the DVR projection of the unregulated interaction.

Regarding the infrared properties of the DVR interaction, we find that $v(k)$ and $v_{\mathrm{DVR}}(k)$ are indeed very different at lowest momenta. As explained earlier, the finite oscillator basis introduces an infrared cutoff (set by the smallest discrete momentum), and thus one has no control over changes in the projected interaction at small momenta.

To improve the infrared behavior, we return to Eq. (2.18). This function is a superposition of functions $\tilde{\phi}_{\mu,0}(k)$ localized around $k \approx k_{\mu,0}$ with weights $c_{\mu,0}$. The key idea is to force this function to have value 1 at $k = 0$ by altering the weight $c_{N_0,0}$ of the highest-momentum DVR function $\tilde{\phi}_{N_0,0}(k)$. Doing so is in the spirit of EFT, as we improve low momentum physics by altering the interaction at higher momenta. Thus, we define new coefficients

$$\begin{aligned} \bar{c}_{\mu,0} &\equiv c_{\mu,0}, && \text{for } \mu = 0, \ldots, N_0 - 1 \\ \bar{c}_{N_0,0} &\equiv \left(1 - \sum_{\nu=0}^{N_0-1} \tilde{\phi}_{\nu,l}(0) c_{\nu,0}\right) / \tilde{\phi}_{N_0,0}(0), && \end{aligned} \tag{2.19}$$

and consider the infrared improved DVR potential

$$v^{\rm IR}_{\rm DVR}(k) = \sum_{\mu=0}^{N_0} \bar{c}_{\mu,0} \tilde{\phi}_{\mu,0}(k). \tag{2.20}$$

By construction, it fulfills $v^{\rm IR}_{\rm DVR}(k) = 1$ for discrete momentum $k = 0$ and lowest N_0 discrete momenta $k_{\mu,0}$ with $\mu = 0, 1, \ldots N_0 - 1$. The infrared-improved contact is shown as the solid blue line in Fig. 2.3. Along with infrared improvement at $k = 0$, the oscillations in the DVR projection $v_{\rm DVR}$ are reduced substantially. We find that the curvature of small oscillations in the function $v^{\rm IR}_{\rm DVR}(k)$ at $k = 0$ is inversely proportional to basis size i.e., it varies as N^{-1}. As is also apparent in the Figure 2.3, the maximum difference between functions $v(k)$ and $v^{\rm IR}_{\rm DVR}(k)$ due to remaining oscillations is about 10% i.e., this effect in the LO potential is already of the order of the error at NLO in pionless EFT calculations. Therefore, we do not need to worry about the residual oscillations in the infrared improved interactions. We also show the $\delta(r)$ function evaluated exactly in the oscillator basis using a green dashed curve. This curve exhibits the strongest oscillations (and particularly large deviations at small momenta) from $v(k) = 1$. We note that the integration measure $\int_0^\infty k^2 dk$ reduces the resultant effect of oscillations when interaction matrix elements in oscillator basis are computed. However, a correct infrared behavior of the interaction is important to study low-energy phase shifts.

To summarize, the infrared-improved DVR contact interaction in momentum space is

$$\langle k', 0 | V^{\rm IR}_{\rm DVR} | k, 0 \rangle = C_{\rm LO} v^{\rm IR}_{\rm DVR}(k') v^{\rm IR}_{\rm DVR}(k), \tag{2.21}$$

where $v^{\rm IR}_{\rm DVR}(k) v^{\rm IR}_{\rm DVR}(k')$ is the non-local cutoff regulator function introduced by finite harmonic oscillator basis. We plot the matrix elements of this interaction in Figure 2.4. The interaction is almost constant till it begins to approach zero at the UV cutoff of the finite harmonic oscillator basis with $N = 8$, $\hbar\omega = 22$ MeV. In what follows, we discuss infrared improvement for NLO terms in Eqn. (1.11).

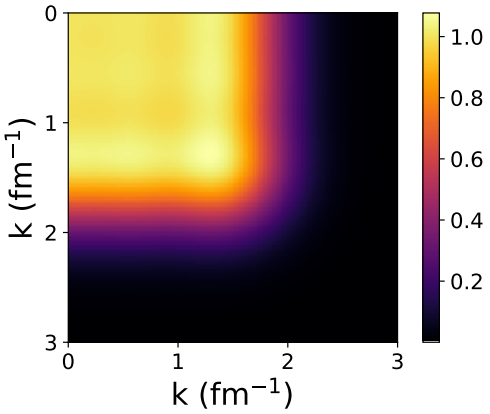

Figure 2.4: (Color online) The infrared-improved DVR contact interaction $V_{\mathrm{DVR}}^{\mathrm{IR}}$ plotted in momentum space. The x- and y-axes represent incoming and outgoing relative momentum, respectively, in fm^{-1}.

2.2.3 Next-to-leading order NN potential

We now turn to the infrared improvement of the NLO S- wave interaction,

$$V(k', l' = 0; k, l = 0) = C_{\mathrm{NLO}} \left\{ w(k) + w(k') \right\} \tag{2.22}$$

with

$$w(k) \equiv k^2. \tag{2.23}$$

Here, C_{NLO} is the coupling strength. The interaction is not separable, and the DVR interaction has momentum-space matrix elements

$$\langle k', 0 | \hat{V}_{\mathrm{DVR}} | k, 0 \rangle = C_{\mathrm{NLO}} \left[w_{\mathrm{DVR}}(k) + w_{\mathrm{DVR}}(k') \right] \tag{2.24}$$

with

$$w_{\mathrm{DVR}}(k) = \sum_{\mu=0}^{N_0} c_{\mu,0} k_{\mu,0}^2 \tilde{\phi}_{\mu,0}(k). \tag{2.25}$$

Figure 2.5 shows the original function $w(k)$ and its DVR projection $w_{\mathrm{DVR}}(k)$ as the dashed-dotted black and dashed red line, respectively. As expected, they coincide at the DVR points (shown as dots).

It is clear that w_{DVR} has the wrong value and the wrong curvature at $k = 0$. We correct it by demanding $\langle k_{\mu,0}, 0|\hat{V}^{\mathrm{IR}}_{\mathrm{DVR}}|k, 0\rangle = V(k_{\mu,l}, 0; k, 0)$ at $k = 0$ which effectively changes the weights $c_{N_0-1,0}$ and $c_{N_0,0}$ to new values $\bar{c}_{\mu,l}$ that satisfy,

$$\begin{aligned} \sum_{\mu=0}^{N_0} \tilde{\phi}_{\mu,0}(0)\bar{c}_{\mu,0} &= 1, \\ \sum_{\mu=0}^{N_0} \tilde{\phi}_{\mu,0}(0)\bar{c}_{\mu,0}k^2_{\mu,0} &= 0. \end{aligned} \tag{2.26}$$

In other words, the infrared-improved interaction is

$$w^{\mathrm{IR}}_{\mathrm{DVR}}(k) = \sum_{\mu=0}^{N_0} \bar{c}_{\mu,0}k^2_{\mu,0}\tilde{\phi}_{\mu,l}(k) \tag{2.27}$$

with

$$\begin{aligned} \bar{c}_{\mu,0} &= c_{\mu,0}, && \text{for } \mu = 0, \ldots, N_0 - 2 \\ \bar{c}_{N_0-1,0} &= \frac{\sum_{\nu=0}^{N_0-2} \tilde{\phi}_{\nu,0}(0)c_{\nu,0}\left(k^2_{N_0,0} - k^2_{\nu,0}\right) - k^2_{N_0,0}}{\tilde{\phi}_{N_0-1,0}(0)\left(k^2_{N_0-1,0} - k^2_{N_0,0}\right)}, \\ \bar{c}_{N_0,0} &= \frac{\sum_{\nu=0}^{N_0-2} \tilde{\phi}_{\nu,0}(0)c_{\nu,0}\left(k^2_{N_0-1,0} - k^2_{\nu,0}\right) - k^2_{N_0-1,0}}{\tilde{\phi}_{N_0,0}(0)\left(k^2_{N_0,0} - k^2_{N_0-1,0}\right)}. \end{aligned} \tag{2.28}$$

The function $w^{\mathrm{IR}}_{\mathrm{DVR}}$ from Eq. (2.27) is shown as a solid blue line in Fig. 2.5. It agrees at $N_0 - 2$ DVR points with $w(k)$ and has the correct infrared behavior. The infrared-improved

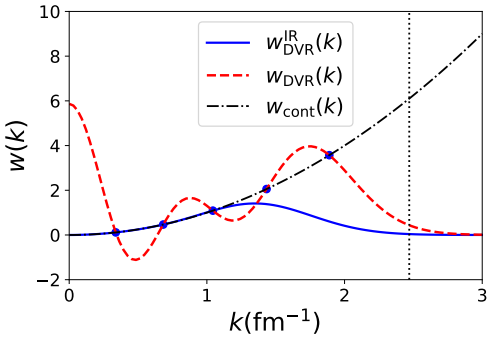

Figure 2.5: (Color online) The solid blue (dashed red) curve shows the NLO interaction term tailored to finite harmonic oscillator basis through DVR with (without) infrared improvement. The solid blue dots represent discrete momentum eigenvalues in the model space $N = 8, \hbar\omega = 22$ MeV, and $l = 0$. The dotted black line depicts the effective sharp cutoff Λ introduced by finite harmonic oscillator basis and the dashed-dotted black line plots the interaction in continuous momentum basis.

interaction has matrix elements

$$\langle \phi_{\mu,0} | V^{\mathrm{IR}}_{\mathrm{DVR}} | \phi_{\nu,0} \rangle = C_{\mathrm{NLO}} \bar{c}_{\mu,0} \bar{c}_{\nu,0} \left(k^2_{\mu,0} + k^2_{\nu,0} \right) .$$

Figure 2.6 shows this interaction as a matrix in momentum space.

Before moving on to the three nucleon contact, I take a small detour to discuss the infrared improvement of other interaction terms that are also quadratic in momentum, but are demoted to higher order terms in KSW counting. I emphasize that we do not use these higher order terms in computing nuclei later.

2.2.4 Higher order short-range NN interactions

In P-wave, the original momentum space interaction is of the form $V(k', 1; k, 1) = C_P g(k) g(k')$ with interaction strength C_P and $g(k) = k$. We fix the slope of the oscillatory DVR function,

$$g_{\mathrm{DVR}}(k) = \sum_{\mu=0}^{N_1} c_{\mu,1} \tilde{\phi}_{\mu,1}(k) k_{\mu,1} \tag{2.29}$$

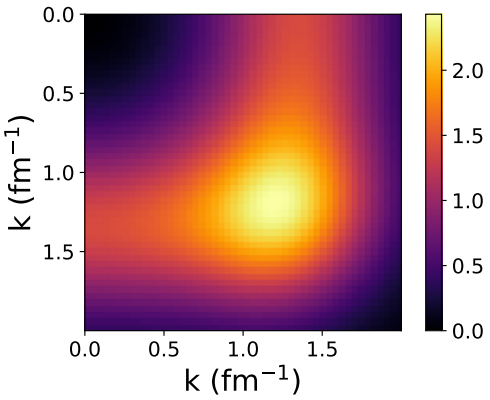

Figure 2.6: (Color online) Momentum space matrix elements of the NLO S-wave interaction in Eqn. (1.11) regulated by the model space $N = 8$ and $\hbar\omega = 22$ MeV. The x- and y-axes are in fm^{-1}.

at $k = 0$ by changing $c_{N_1,1}$ to

$$\bar{c}_{N_1,1} = \frac{\left(1 - \sum_{\mu=0}^{N_1-1} c_{\mu,1}\tilde{\phi}'_{\mu,1}(0)k_{\mu,1}\right)}{\tilde{\phi}'_{N_1,1}(0)k_{N_1,1}} \tag{2.30}$$

to get infrared-improved oscillator regulator,

$$g^{\rm IR}_{\rm DVR}(k) = \sum_{\mu=0}^{N_1} \bar{c}_{\mu,1}\tilde{\phi}_{\mu,1}(0)k_{\mu,1}. \tag{2.31}$$

Here the prime ($'$) on discrete momentum eigenfunction denote its derivative in momentum space. The solid line in Figure 2.7 shows that the infrared-improved function $g^{\rm IR}_{\rm DVR}(k)$ which has reduced oscillations in comparison to simple DVR projection $g_{\rm DVR}(k)$ (shown by dashed curve) of the original function $g(k)$ (represented by dashed-dotted line).

Similarly, we consider the infrared-improved function of the short-range tensor term $V(k', 2; k, 0) = C_{SD}k'^2$ that couples S- and D-partial waves with coupling strength C_{SD}.The DVR interaction matrix element in momentum space is

$$\langle k', 2|\hat{V}^{\rm DVR}|k, 0\rangle = C_{SD} f_{\rm DVR}(k')v_{\rm DVR}(k) \tag{2.32}$$

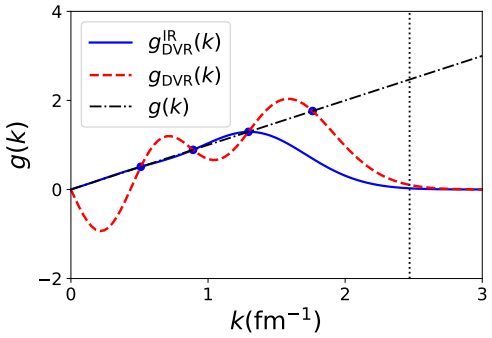

Figure 2.7: (Color online)The solid line is finite oscillator regulator function $g^{\rm IR}_{\rm DVR}(k)$. The dashed-dotted black line plots the original function $g(k)$ in $l = 1$ partial wave which coincides with the projected function $g_{\rm DVR}(k)$ (shown by dashed curve) at solid dots that represent the discrete DVR momenta $k_{\mu,1}$ in the model space $N = 8, \hbar\omega = 22$ MeV. The dotted black line depicts the effective sharp cutoff Λ introduced by finite harmonic oscillator basis.

where, $f_{\rm DVR}(k') = \sum_{\mu=0}^{N_2} c_{\mu,2}\tilde{\phi}_{\mu,2}(k')k^2_{\mu,2}$. While can use Eq. (2.20) to fix the infrared behavior of $v_{\rm DVR}$, we need to correct the curvature of $f_{\rm DVR}$ at $k = 0$ by altering $c_{N_2,2}$ to

$$\bar{c}_{N_2,2} = \frac{\left(2 - \sum_{n=0}^{N_2-1} c_{\mu,2}\tilde{\phi}''_{\mu,2}(0)k^2_{\mu,2}\right)}{\tilde{\phi}''_{N_2,2}(0)k^2_{N_2,2}}. \tag{2.33}$$

Thus, the oscillator regulator for $l = 2$ function $f(k) = k^2$ is

$$f^{\rm IR}_{\rm DVR}(k) = \sum_{\mu=0}^{N_2} \phi_{\mu,2}(k')\bar{c}_{\mu,2}k^2_{\mu,2} \tag{2.34}$$

Here, two primes($''$) denote double derivative of the DVR eigenfunction with respect to momentum. In Figure 2.8, the solid line shows the infrared-improved function $f^{\rm IR}_{\rm DVR}(k)$ in comparison to the original function $f(k)$ and its DVR projection $f_{\rm DVR}(k)$ are shown by dashed-dotted and dashed curves, respectively. The solid dots show DVR points in chosen model space $N = 8$, $\hbar\omega = 22$ MeV and $l = 2$.

To summarize, the momentum space matrix element of oscillator regulated tensor term is

$$\langle k', 2|V^{\rm IR}_{\rm DVR}|k, 0\rangle = C_{SD} f^{\rm IR}_{\rm DVR}(k')v^{\rm IR}_{\rm DVR}(k), \tag{2.35}$$

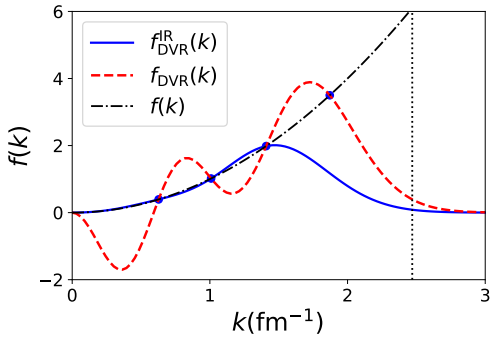

Figure 2.8: (Color online)The solid line is the finite oscillator regulator function $f^{\rm IR}_{\rm DVR}(k)$. The dashed-dotted black line plots the original function $f(k)$ in $l = 2$ partial wave which coincides with the projected function $f_{\rm DVR}(k)$ (shown by dashed curve) at solid dots that represent the discrete DVR momenta $k_{\mu,2}$ in the model space $N = 8, \hbar\omega = 22$ MeV. The dotted black line depicts the effective sharp cutoff Λ introduced by finite harmonic oscillator basis

2.2.5 Three-nucleon contact

We consider the three-body contact

$$V(k', p'; k, p) = C_{NNN} \tag{2.36}$$

with its LEC C_{NNN} as three-nucleon (NNN) contact in Eqn. (1.12) has no functional dependence on Jacobi momenta. The momenta k, k' denote the incoming and outgoing relative momentum between particles 1 and 2, respectively, while p, p' are the incoming and outgoing momentum of particle 3 relative to the center of mass of particles 1 and 2, respectively. We use following definition of Jacobi momenta,

$$\begin{aligned} \vec{k} &= \frac{1}{\sqrt{2}}(\vec{p_1} - \vec{p_2}), \\ \vec{p} &= \sqrt{\frac{2}{3}}\left(\frac{1}{2}(\vec{p_1} + \vec{p_2}) - \vec{p_3}\right) \end{aligned} \tag{2.37}$$

where, $\vec{p}_1$, $\vec{p}_2$ and $\vec{p}_3$ are momentum of particles 1, 2 and 3, respectively, in laboratory coordinates. We prefer the above normalization because the effective mass associated with each Jacobi momenta is equal to the nucleon mass m. This leads to identical oscillators

for each Jacobi momenta with the oscillator length $\bar{b} = \sqrt{\hbar/m\omega}$. We note that it differs from the oscillator length (2.3) used in case of NN potential. We recall that the contact interaction is active only for zero Jacobi orbital angular momentum states; thus we ignore the orbital angular momentum label in what follows. Also, the matrix element in Eq. (2.36) is antisymmetric only under the exchange of particle 1 and 2. While one needs to fully antisymmetrize the potential under exchange to solve the Schrödinger equation, it is not relevant for the purposes of regulating the NNN contact with oscillator basis. In what follows, we discuss two different non-local oscillator regulators for the NNN force.

Cutoff in Jacobi momenta

In this case, we regulate the incoming Jacobi momenta k and p individually (and similarly for the outgoing Jacobi momenta). Thus for this type of cutoff, the interaction between incoming and outgoing two-particle states in Jacobi basis has separable regulators as can be seen from its DVR projection,

$$\langle k', p'|\hat{V}^{\text{sq}}_{\text{DVR}}|k, p\rangle = C^{\text{sq}}_{NNN} v_{\text{DVR}}(k')v_{\text{DVR}}(p')v_{\text{DVR}}(k)v_{\text{DVR}}(p). \tag{2.38}$$

Here, v_{DVR} is as in Eq. (2.18), except now with the new oscillator length $\bar{b}$. Thus, the infrared improvement of the NNN contact is identical to the NN contact discussed before. Therefore for this regulation scheme, the oscillator regulated NNN contact is simply

$$\langle k', p'|\hat{V}^{\text{sq}}_{\text{DVR}}|k, p\rangle = C^{\text{sq}}_{NNN} v^{\text{IR}}_{\text{DVR}}(k')v^{\text{IR}}_{\text{DVR}}(p')v^{\text{IR}}_{\text{DVR}}(k)v^{\text{IR}}_{\text{DVR}}(p) \tag{2.39}$$

where $v^{\text{IR}}_{\text{DVR}}(k)$ is calculated using Eq. (2.20) with oscillator length $\bar{b}$. Figure 2.9 plots the function $v^{\text{IR}}_{\text{DVR}}(k)v^{\text{IR}}_{\text{DVR}}(p)$ in harmonic oscillator model space with $N = 8$ and $\hbar\omega = 22$ MeV. Note that we have renamed the LEC as C^{sq}_{NNN} in Eq. (2.38) because of the square shape of the interaction in the Jacobi basis.

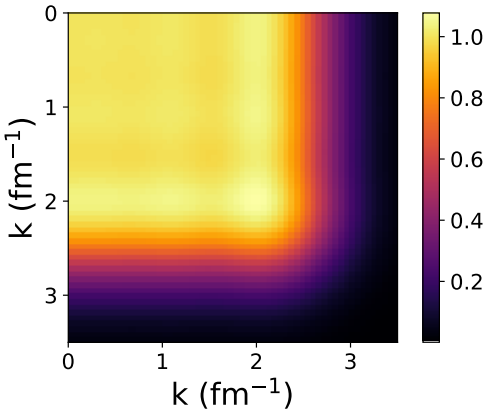

Figure 2.9: (Color online) Momentum space matrix elements $v^{\rm IR}_{\rm DVR}(k)v^{\rm IR}_{\rm DVR}(p)$ in harmonic oscillator model space with $N = 8$ and $\hbar\omega = 22$ MeV as a function of the two incoming Jacobi momenta k and p.

Hyperspherical cutoff

Often the cutoff of the NNN force is in the hyper momentum (For example, see Refs. [27, 67]). Thus, we introduce the hyper-radial momentum ρ and the hyperangle α as

$$\begin{aligned} k &= \rho\cos\alpha, \\ p &= \rho\sin\alpha, \end{aligned} \tag{2.40}$$

which govern hyper-radial quantum number n and hyper-spherical angular quantum number K, respectively. The hyper-radial wave function of the six-dimensional oscillator for energy eigenstate $(2n + K + 3)\hbar\omega$ in hyper-momentum space $\tilde{\Psi}_{n,K}(\rho)$ is proportional to $\rho^K e^{-\frac{\rho^2\bar{b}^2}{2}} L_n^{K+2}(\rho^2\bar{b}^2)$. Here, $L_n^{K+2}(\rho^2\bar{b}^2)$ is an associated Laguerre polynomial (For more details of D-dimensional hyper spherical oscillators see Refs. [4, 65]).

We recall that the NNN contact in Jacobi position coordinates (η_1, η_2) is $\delta^(3)(\vec{\eta}_1)\delta^(3)(\vec{\eta}_2)$ with vanishing orbital angular momentum. Consequently, in hyper-spherical momentum coordinates it should correspond to an isotropic hyper-radial contact of the form $\delta(\rho)/\rho^5$. In other words, in the context of NNN contact only hyper-angular momentum $K = 0$

eigenstates of the six-dimensional harmonic oscillator

$$\tilde{\Psi}_n(\rho) = \bar{b}^3 \sqrt{\frac{2n!}{\Gamma(n+3)}} e^{-\frac{\rho^2\bar{b}^2}{2}} L_n^2(\rho^2\bar{b}^2), \tag{2.41}$$

corresponding to energy $(2n+3)\hbar\omega$, are relevant.

It follows that the hyper-radial DVR for the six-dimensional finite oscillator with zero hyper-angular momentum and maximum energy quanta $(N+3)\hbar\omega$ is formed by zeros of the Laguerre polynomial $L^2_{N_0+1}(\rho^2\bar{b}^2)$, where $N_0 = N/2$ (Note that in three-body Jacobi basis $N_K = (N-K)/2$). The momentum eigenfunction corresponding to eigenvalue ρ_μ is

$$\Phi_\mu(\rho) = C_\mu \sum_{n=0}^{N_0} \tilde{\Psi}_n(\rho_\mu)\tilde{\Psi}_n(\rho). \tag{2.42}$$

Here, C_μ is a normalization constant. Analogous to Eq. (2.10), we find

$$C_\mu = \frac{\rho_\mu \bar{b}}{\sqrt{(N_0+3)(N_0+1)}\tilde{\Psi}_{N_0}(\rho_\mu\bar{b})}. \tag{2.43}$$

Thus, the DVR projection of NNN contact is

$$\langle\rho'|U_{\rm DVR}|\rho\rangle = u_{\rm DVR}(\rho')u_{\rm DVR}(\rho) \tag{2.44}$$

with

$$u_{\rm DVR}(\rho) = \sum_{\mu=0}^{N_0} C_\mu \tilde{\Phi}_\mu(\rho). \tag{2.45}$$

As before, the simple DVR projection of the interaction needs infrared improvement. We generalize the solution (2.19) to improve the low-momentum behavior of the DVR interaction at hyper-radial momentum $\rho = 0$ by demanding $u^{\rm IR}_{\rm DVR}(0) = 1$,

$$\begin{aligned} \bar{C}_\mu &\equiv C_\mu, && \text{for } \mu = 0, \ldots, N_0 - 1 \\ \bar{C}_{N_0} &\equiv \left(1 - \sum_{\nu=0}^{N_0-1} \tilde{\Phi}_\nu(0) C_\nu\right) / \tilde{\Phi}_{N_0}(0) \end{aligned} \tag{2.46}$$

and arrive at the infrared-improved function

$$u^{\rm IR}_{\rm DVR}(\rho) = \sum_{\mu=0}^{N_0} \bar{C}_\mu \tilde{\Phi}_\mu(\rho). \tag{2.47}$$

Thus, the infrared-improved potential is

$$\langle \rho' | U^{\rm IR}_{\rm DVR} | \rho \rangle = C^{\rm sp}_{NNN} u^{\rm IR}_{\rm DVR}(\rho') u^{\rm IR}_{\rm DVR}(\rho). \tag{2.48}$$

Here $C^{\rm sp}_{NNN}$ is the corresponding coupling strength. Figure 2.10 compares Eq. (2.47) of the infrared-improved contact (the solid blue line) with the contact in Eq. (2.45) lacking infrared improvement (the dashed red line). At momenta smaller than infrared cutoff, the latter exhibits large deviations from original contact interaction function $u(0) = 1$. Both the curves coincide at DVR points in hyper-radial momentum, represented by solid blue dots.

The codes for many-body calculations typically use nuclear potential input in Jacobi coordinates and therefore, we transform the matrix elements in Eq. (2.48) to the Jacobi basis. Since the DVR in the Jacobi momenta essentially provides us with a Gauss-Laguerre integration that is exact for polynomials of degree $2N_0$ in k and in p, one can exactly integrate the basis functions in Eq. (2.41) to get,

$$\langle \phi_{\nu',0} \phi_{\mu',0} | \hat{U}^{\rm IR}_{\rm DVR} | \phi_{\mu,0} \phi_{\nu,0} \rangle = C^{\rm sp}_{NNN} \bar{u}_{\mu'\nu'} \bar{u}_{\mu\nu} \tag{2.49}$$

where IR improved function $u^{\rm IR}_{\rm DVR}$ is exactly mapped in Jacobi momentum space with $\bar{u}_{\mu\nu} = c_{\mu,0} c_{\nu,0} u^{\rm IR}_{\rm DVR}\big(\sqrt{k^2_{\mu,0} + p^2_{\nu,0}}\big)$. We note that while calculating $c_{\mu,0}$ via Eq. (2.10) and in finding discrete Jacobi momenta $k_{\mu,0}$ that are obtained from roots of Laguerre polynomial $L^{1/2}_{N_0}(k^2\bar{b}^2)$ we use oscillator length $\bar{b}$. Figure 2.11 plots DVR interaction matrix elements in Eq. (2.49) in Jacobi momentum space (when finite oscillator in each Jacobi momentum is allowed maximum energy of $8\hbar\omega$ at $\hbar\omega = 22$ MeV). We label the corresponding LEC with superscript "sp" based on the spherical shape of the regular in Jacobi momentum space.

In what follows we explain the advantage of using the hyper-spherical cutoff, over the square cutoff for the three-nucleon force, in reference to many-body calculations.

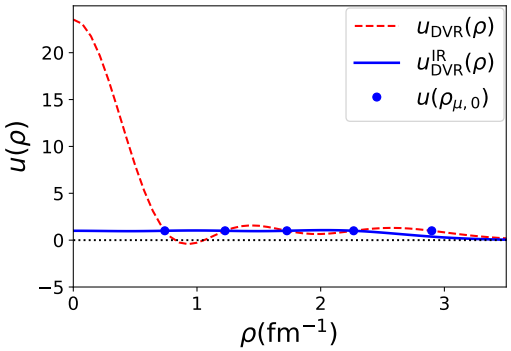

Figure 2.10: (Color online) The solid blue and dashed red curves show the three-nucleon contact in the DVR basis in hyperspherical coordinates with and without infrared improvement, respectively. The former is close to $u(\rho) = 1$ at low momentum. The solid blue dots represent the DVR momenta ρ_μ for $\mu = 0, \ldots, N_0$ when $2N_0 = 8$ and $\hbar\omega = 22$ MeV.

2.2.6 Hyper-spherical vs square cutoff

The basis size of three-body matrix elements are a bottleneck for many-body methods. So when we use no-core shell model in Jacobi coordinates to compute $A \leq 4$ nuclei, a triangular truncation of the type

$$\mu + \nu \leq N \tag{2.50}$$

is used to reduce the number of matrix elements of the NNN force. Here, μ and ν are the principal harmonic oscillator quantum numbers in Jacobi basis for the NNN system and $(N+3/2)\hbar\omega$ is the maximum energy allowed for each of the two Jacobi oscillators. Therefore, it is important to analyze our hyper-spherical and square regulators for NNN contact in context of this truncation.

We begin with the square regulator discussed in Section 2.2.5. Since it regulates each incoming and outgoing momentum individually, the resultant infrared-improved NNN contact potential in Eq. (2.38) has non-zero matrix elements for all Jacobi oscillator states (μ, ν) that satisfy $\mu + \nu \leq 2N$. Therefore when the truncation (2.50) is enforced in many-body calculations, we miss the matrix elements in three-nucleon Jacobi oscillator basis states that have $(\mu+\nu) > N$. To study its impact we use the remaining interaction matrix elements [after employing the truncation (2.50)] in oscillator basis to reconstruct the regulator function

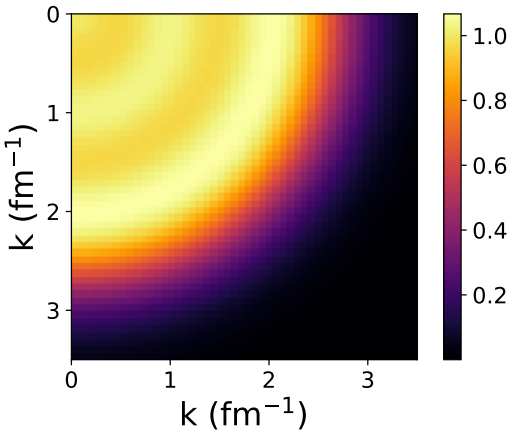

Figure 2.11: (Color online) Size of momentum space matrix elements $\bar{u}(k,p) = c_{\mu,0}c_{\nu,0}u^{\rm IR}_{\rm DVR}\left(\sqrt{k^2+p^2}\right)$ in harmonic oscillator model space $N = 8, \hbar\omega = 22$ MeV,$l_1, l_2 = 0$. x- and y- axis represent Jacobi momenta in fm^{-1}.

in incoming (or outgoing) Jacobi momentum space i.e,

$$v^{\rm IR}_{\rm trunc}(k,p) = \sum_{\mu=0}^{N_0}\sum_{\nu=0}^{N_0-\mu} \bar{c}_{\mu,0}\phi_{\mu,0}(k)\bar{c}_{\nu,0}\phi_{\mu,0}(p) \tag{2.51}$$

Note that here $\phi_{\mu,0}(k)$ and $\bar{c}_{\mu,0}$ are eigenfunctions and infrared-improved weights, respectively, for DVR in Jacobi coordinates of the three-nucleon system. The important point to note here is that the function $v^{\rm IR}_{\rm trunc}(k,p)$, which we retrieve after truncation, is no longer the original infrared-improved regulator $v^{\rm IR}_{\rm DVR}(k)v^{\rm IR}_{\rm DVR}(p)$.

In Figure 2.12 we plot function $v^{\rm IR}_{\rm trunc}(k,0)$ for three different model spaces, $N = 6, \hbar\omega = 26.63$ MeV (dashed-dotted green curve); $N = 8, \hbar\omega = 22$ MeV (dashed blue curve), and $N = 8, \hbar\omega = 18.74$ MeV (solid magneta line) which correspond to three separate regulators with the ultraviolet cutoff ≈ 487 MeV. From this Figure we learn that after the truncation (2.50) is imposed on the NNN potential with square cutoff, the regulator effects at the same ultraviolet cutoff are not limited to high momenta; as one would expect from an EFT potential. Instead, we find large oscillations at low-momentum that is proportional to basis size N. It is clear we no longer have a pure contact interaction. As a result, the ground-state energy of ^{4}He nucleus also exhibits a strong dependence on basis size N when

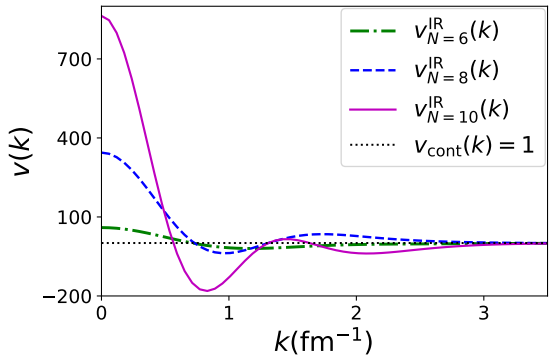

Figure 2.12: (Color online) The oscillator regulator $v^{\rm IR}_{\rm trunc}(k,0)$ of NNN interaction (2.51), reconstructed only from interaction matrix elements in remaining harmonic oscillator basis states after truncation (2.50). The dashed-dotted green line plots this function in model space $N=6$ and $\hbar\omega=26.63$ MeV; dashed blue line in $N=8$ and $\hbar\omega=22$ MeV, and solid magenta line in $N=10$ and $\hbar\omega=18.74$ MeV. All three cases have the same cutoff $\Lambda\approx 487$ MeV. The dotted black line shows the unregulated momentum space function $v(k)=1$.

computed using truncated momentum space matrix elements

$$\langle k',p'|U^{\rm IR}_{\rm trunc}|k,p\rangle = C^{\rm sq}_{NNN} v^{\rm IR}_{\rm trunc}(k',p') v^{\rm IR}_{\rm trunc}(k,p). \tag{2.52}$$

Our goal is to keep three-nucleon basis size computationally feasible without altering the NNN contact at low-momentum. Thus, we also tried using the NNN potential (2.38) regulated by finite model space with half the oscillator states in each Jacobi coordinate i.e., $\mu,\nu\leq N/2$. Doing so restricts NNN matrix elements to Jacobi basis states with combined maximum excitation energy of $(N+3)\hbar\omega$. Although it is commensurate with the maximum energy quanta allowed in basis truncation (2.50), we found that even for this adaptation of square cutoff of the NNN contact ^{4}He binding energy increases with increasing model space size N (at constant ultraviolet cutoff).

On the contrary, the truncation (2.50) is exact for hyper-spherical cutoff i.e., a NNN contact regulated by finite hyper-spherical basis with maximum excitation energy $(N+3)\hbar\omega$, has zero strength in three-body Jacobi basis states with $\mu+\nu>N$ by design. This is straightforward to see when we compare the energy eigenvalue formula in both the representations of the two-particle oscillator basis for vanishing Jacobi orbital angular

momenta and zero hyper angular momentum, respectively. If we constrain the maximum energy in the hyper-spherical basis to $(N+3)\hbar\omega$, the truncation (2.50) automatically follows.

Therefore, the NNN contact with hyper-spherical oscillator regulator remains intact when the additional three-body basis truncation (2.50) is employed while computing nuclei with mass number $A > 2$ in Jacobi coordinates. Thus, the NNN contact in the oscillator basis with hyper-spherical cutoff is favorable in view of many-body calculations and this is what we use in rest of our work, unless specified otherwise. In what follows, we discuss variation of the interaction cutoff in oscillator EFT.

2.3 Varying cutoff of the oscillator regulator

In oscillator EFT one needs to compute interaction matrix elements at only one cutoff and nucleon mass, due to the scaling relations we derive in this section. The cutoff of the interaction regulated by a finite harmonic oscillator depends on the basis parameters N and $\hbar\omega$. It is understood that keeping the model space size as small as possible is favorable when computing many-body systems. In what follows, we fix the number of oscillator shells by choosing $N = 8$ and vary the ultraviolet cutoff (which is the same as interaction cutoff) by changing oscillator spacing $\hbar\omega$ (this in turn changes oscillator length b). We select values of $\hbar\omega$ such that it yields interaction ultraviolet cutoff $\Lambda_{\rm UV} > \Lambda_{\rm break}$, and spatial extent of the finite basis L (2.1) is larger than the radius of nuclei we want to compute. We find that NN and NNN matrix elements of oscillator pionless EFT simply scale with $\hbar\omega$.

Below we derive simple scaling relations that hold at fixed N. From Eqns. (2.10) and (2.6) we find $\tilde{\psi}_{n,l}(k) \propto b^{3/2}$, $c_{\mu,l} \propto b^{-3/2}$, and $k_{\mu,l} \propto b^{-1}$. The discrete momentum $k_{\mu,l}$ is inversely proportional to the oscillator length because at fixed $N_0 = N/2$, the roots of the generalized Laguerre polynomial $L^{l+1/2}_{N_0+1}(k^2b^2)$ remain constant. As a result, changes in the oscillator spacing $\hbar\omega$ or the nucleon mass m simply rescales the matrix elements of the NN

potential at LO and NLO, and the NNN contact as,

$$\begin{aligned} V_{\rm LO} &\propto C_{\rm LO} b^{-3} \propto C_{\rm LO} \left(m\hbar\omega\right)^{3/2}, \\ V_{\rm NLO} &\propto C_{\rm NLO} b^{-5} \propto C_{\rm NLO} \left(m\hbar\omega\right)^{5/2}, \\ V_{NNN} &\propto C_{NNN} b^{-6} \propto C_{NNN} \left(m\hbar\omega\right)^{3}, \end{aligned} \tag{2.53}$$

respectively.

We keep the scaling with respect to the nucleon mass m explicit because it will be useful for computing interaction matrix elements at unphysical pion mass in the context of lattice nuclei. Thus in our approach, we only had to compute interaction matrix elements for one set of nucleon mass and oscillator spacing (or ultraviolet cutoff). For other cutoffs and pion masses the above relations are used.

So far we have presented the details of calculating oscillator regulated interaction matrix elements of pionless EFT. Now we need to adjust the LECs to low-energy observables, to encode effects of high-energy dynamics that is not included explicitly in the EFT. In what follows, we describe the procedure used to obtain LECs in pionless EFT potential at LO and NLO.

2.4 Calibration

In this Section, we adjust the LECs of pionless EFT to data in Table 2.1. To compute phase shifts directly using oscillator EFT matrix elements as input, we follow Ref. [75], which is based on Jacobi (or J)-matrix approach [39]. At the back end, this method begins by expanding continuum wave function as a linear combination of square integrable oscillator states. The set of simultaneous equations are made finite by decoupling the finite model space of size N_l+1 in which potential is active, from remaining oscillator states $N_l+1, N_l+2, ...\infty$. Thus, oscillator EFT potentials are a natural fit for this method.

In case of binding energies, it is important to remember that LECs should be optimized such that the 'infinite-volume' result for the optimized LEC values reproduces data. In other words, we need to make sure the computed binding energy is ultraviolet and infrared

Table 2.1: Relevant values of physical and lattice QCD data (all in MeV), namely the pion mass m_π, the nucleon mass m, the di-neutron binding energy B_{nn}, the deuteron binding energy B_d, the triton binding energy B_t, the singlet and triplet scattering lengths ${}^{np}a_s$ and a_t, respectively, the singlet and triplet effective ranges ${}^{np}r_s$ and r_t, respectively.

	Nature		Lattice	
m_π	139.5 ± 0.1	[70]	$806. \pm 1$	[12]
m	$939. \pm 1$	[64]	$1634. \pm 18$	[12]
B_{nn}	–		15.9 ± 4	[12]
B_d	2.2245		19.5 ± 5	[12]
B_t	8.482	[83]	53.9 ± 10.7	[12]
${}^{np}a_s{}^{-1}$	-8.31	[23]	84.7 ± 18	[11]
${}^{np}r_s{}^{-1}$	71.75	[23]	174.6 ± 25	[11]
$a_t{}^{-1}$	36.4	[23]	$108. \pm 13$	[11]
$r_t{}^{-1}$	112.18	[23]	217.8 ± 46	[11]

converged. In our oscillator EFT approach, we have ultraviolet convergence by construction because interaction is regulated by finite model space which we choose to be $N = 8$ (we consider other model spaces separately in Appendix. A). The Hamiltonian, i.e. the sum of kinetic and potential energy, is evaluated in model spaces of size $N = 8, 10, 12, \ldots$. By construction the interaction matrix elements, for all oscillator states with $N > 8$, are zero. The increase in the model space for the kinetic energy expands the phase-space coverage along position axis and better captures the exponential tail of the bound state wave function. This yields infrared convergence, see Ref. [16] for details.

In Jacobi coordinates, the NN system reduces to one-body problem and is therefore easy to solve. By the virtue of more number of particles, for nuclei with mass number $A = 3, 4$ the eigenvalue problem is slightly more complex. We use no-core shell model [68] to compute $A \leq 4$ nuclei. In no-core shell model, all the nucleons are active in the chosen model space; interacting through two- and three-body potentials. Andreas Ekström performed these calculations using no-core shell model in Jacobi coordinates with the infrared-improved two- and three-body matrix elements, that I provided, as input.

Before moving further, we briefly discuss the theoretical uncertainties. There are three sources of uncertainties in our calculations, (i) missing higher-order terms in the truncated EFT interaction, (ii) the finite-volume effects of the model space, and (iii) uncertainties in

the LECs due to uncertainty in the input used for optimization. In KSW power counting, the uncertainty from neglected higher-order terms at LO is $\alpha_{\rm EFT}$ and $\alpha_{\rm EFT}^2$ at NLO. As we discussed before, $\alpha_{\rm EFT}$ for few-body systems can be calculated using effective range and scattering length based on universal properties that are known for these systems. We use the data in Table 2.1 to get $\alpha_{\rm EFT} \sim 1/3$ for the atomic case, and ≈ 0.5 at unphysical pion mass ($m_\pi = 806$ MeV). Based on the above power counting, the EFT uncertainty in the value of any observable O is expected to be of the form [33]

$$\Delta O = O_0 \left(c_1 \alpha_{\rm EFT} + c_2 \alpha_{\rm EFT}^2 + \ldots \right) . \tag{2.54}$$

where the coefficients c_k are observable dependent and are expected to have natural size. We note that for atomic nuclei only uncertainties (i) and (ii) are relevant. On the other hand, at unphysical pion mass uncertainty in lattice QCD input has the largest contribution. In our work, we choose central values of the lattice QCD data in Table 2.1 to optimize the EFT potential.

In what follows, we tune coupling strengths to virtually converged deuteron and triton binding energy results and low-momentum phase shifts. We analyze cutoff dependence of LECs by changing oscillator spacing in model space $N = 8$. We discuss this separately for atomic nuclei at physical and lattice nuclei at unphysical pion mass.

Physical pion mass

For atomic nuclei, we use the deuteron's binding energy, the effective-range expansion of the S-wave phase shifts, and the phase shifts of CD-Bonn potential [62] to constrain the LECs of the NN interaction. The NNN force is adjusted to the triton (^{3}H) binding energy.

At LO we have two LECs associated with NN contact interactions and one for the NNN contact. In $^3S_1$ partial wave, the LEC is adjusted to reproduce the deuteron binding energy. The coupling strength in the singlet S channel for the NN contact is optimized through a χ^2 fit to neutron-proton (np) CD-Bonn phase shifts for relative momenta $p_{\rm rel} \in [3, 10]$ MeV. For the phase shift data we employ theoretical uncertainties in the objective function that are consistent with the power counting in pionless EFT. After optimizing the LO singlet S

coupling coefficient, we use the effective range expansion (1.9) to predict scattering length. The scattering length that we obtain at various ultraviolet cutoffs agrees with data within 30%, which is within the LO pionless EFT uncertainty estimate discussed earlier. Table 2.2 shows the values of the LECs at LO for potentials defined in model spaces with $N = 8$ for different cutoffs.

The NN LO LECs are consistent with analytical estimate as discussed below. Consider a contact interaction with a non-local regulator function $v(k, \Lambda)$,

$$V(k', k) = C_0 v(k', \Lambda) v(k, \Lambda). \tag{2.55}$$

As usual, Λ is the cutoff of the interaction. To analytically derive the size of the interaction strength C_0, we start with step-function regulator $v(k, \Lambda) = \Theta(\Lambda - k)$ and solve the Schrödinger equation in momentum space. In doing so, we integrate over the angular coordinates in the usual three dimensional integration measure $\int dk^3/(2\pi)^3$ to compare analytical result to LECs obtained in harmonic oscillator EFT, which by construction only considers radial momentum integration $\int k^2 dk$ in each partial wave. In the limit $\Lambda \gg \kappa, a^{-1}$, where κ is the neutron-proton binding momentum and a is the triplet S channel scattering length, we get,

$$C_0 \approx \frac{1}{m_N \Lambda} \tag{2.56}$$

Here, m_N is nucleon mass. Similarly, for a Gaussian regulator $v(k, \Lambda) = e^{\frac{-1}{2}\frac{k^2}{\Lambda^2}}$ we find,

$$C_0 \approx \frac{2}{m_N \Lambda \sqrt{\pi}} \tag{2.57}$$

At a cutoff $\Lambda \approx 487$ MeV, we get $C_0 \approx -0.22 \times 10^{-5}$ MeV^{-2} for the hard cutoff and $C_0 \approx -0.25 \times 10^{-5}$ MeV^{-2} for the Gaussian regulator. We find similar value of the LEC $\tilde{C}_{^3S_1}$ for the same cutoff (see Table 2.2). In an EFT, different regulators yield slightly different coupling strengths to reproduce same low-energy observables; which in our case are the binding energy and the scattering length. The same reasoning upholds while varying the cutoff of the interaction for a fixed regulator. This is also evident from analytical formula of LEC in Eqns. (2.56) and (2.57); for both regulators $C_0 \propto 1/\Lambda$. Similarly, for the oscillator

Table 2.2: The leading order LECs $\tilde{C}_{^3s_1}$ and $\tilde{C}_{^1s_0}$ (both in 10^{-5}MeV^{-2}), and c_E (dimensionless) for atomic nuclei (with nucleon mass $m = 939$ MeV) at different cutoffs Λ (in MeV) obtained from varying the oscillator frequency $\hbar\omega$ (in MeV), for interactions in a model space with $N = 8$.

$\hbar\omega$	Λ	$\tilde{C}_{^3s_1}$	$\tilde{C}_{^1s_0}$	c_E
5	232.35	−1.006988	−0.597220	−0.163306
10	328.59	−0.624098	−0.431559	−0.671882
22	487.38	−0.379465	−0.296100	−0.238514
40	657.19	−0.266381	−0.221703	−0.091625

regulator (where the cutoff is a function of oscillator spacing) the LO LECs $\tilde{C}_{^3S_1}$ and $\tilde{C}_{^1S_0}$ in Table 2.2 are roughly proportional to $(\hbar\omega)^{-1/2}$. Thus, we conclude that oscillator regulators are similar to the conventional momentum-space regulator functions.

Now we turn to the NLO potential. According to the KSW counting we have three LECs from LO contacts, and two additional LECs attached to the NLO NN contacts in S-partial wave. It is important to note that we adjust the NLO interaction non-perturbatively. This implies that we refit LO LECs alongside the new LECs. So, in the triplet S channel we simultaneously adjust the two LECs ($\tilde{C}_{^3S_1}$, $C_{^3S_1}$) to reproduce the deuteron binding energy and the charge radius (1.976 fm). In the singlet S channel the LECs ($\tilde{C}_{^1S_0}$, $C_{^1S_0}$) are fit to the np CD-Bonn phase shifts for energies $E_{\text{rel}} \in [0.01, 0.1]$ MeV. In the context of the effective range expansion, the optimized NN interaction fixes the scattering length and effective range. Next, our collaborator Andreas Ekström adjusted the NNN contact coefficient to triton binding energy using the optimized NLO NN LECs and the our two- and three-body matrix elements. We repeat the same procedure at four different cutoffs and the results are presented in Table 2.3.

Figure 2.13 shows the phase shifts from pionless EFT at LO (blue dot-dashed line) and NLO (red dashed line), and compares them to those of the CD-Bonn potential (black line). The phase shift plots illustrate the quality of the infrared-improved potentials. The oscillations that were observed in Refs. [16, 86] are reduced, which allowed us to reliably optimize pionless EFT LECs to reproduce low-energy data. Clearly, the LO potentials reproduce phase shifts for momenta $p_{\text{rel}} \lesssim {a_{s,t}}^{-1}$, while the NLO interactions extends the

Table 2.3: The next-to-leading order LECs $\tilde{C}_{^3s_1}$ and $\tilde{C}_{^1s_0}$ (both in 10^{-5}MeV^{-2}), and $C_{^3s_1}$ and $C_{^1s_0}$ (both in 10^{-10}MeV^{-4}), and c_E (dimensionless) for atomic nuclei (with nucleon mass $m = 939$ MeV) for different cutoffs Λ (in MeV) obtained from varying the oscillator frequency $\hbar\omega$ (in MeV), for interactions in a model space with $N = 8$.

$\hbar\omega$	Λ	$\tilde{C}_{^3s_1}$	$C_{^3s_1}$	$\tilde{C}_{^1s_0}$	$C_{^1s_0}$	c_E
5	232.35	−1.001248	−0.039732	−0.718772	1.124941	0.533367
10	328.59	−0.919696	1.078144	−0.588224	0.725705	−0.274206
22	487.38	−0.809378	0.772254	−0.612966	0.727724	−0.008170
40	657.19	−0.866529	0.689544	−0.605710	0.590509	−0.061330

range to $p_{\text{rel}} \lesssim {r_{s,t}}^{-1}$. The uncertainty in our results are consistent with expectation from EFT at LO $[\mathcal{O}(\frac{p_{\text{rel}}}{\Lambda_{\text{break}}})]$ and NLO $[\mathcal{O}\big(\frac{p_{\text{rel}}^2}{\Lambda_{\text{break}}^2}\big)]$, as confirmed by the blue and red shaded areas, respectively. In addition, the LO and NLO phase shifts at different cutoffs lie within the estimated error bands. We note that the estimate of uncertainty in Fig. 2.13 at each order is scaled by a constant factor of natural size such that the uncertainty in phase shifts at LO spans the actual data and NLO uncertainty (as done in Ref. [26] and can be understood as the largest $|c_k|$ in Eq. (2.54)).

After having tested our approach on physical nuclei, we turn to calibrating the potential at an unphysical pion mass. Most of the steps remain the same except now, experimental data, that was used to adjust LECs in the case of physical nuclei, is replaced by data from LQCD calculations in second column of Table 2.1.

Unphysical pion mass ($m_\pi = 806$ MeV)

For lattice nuclei, we use lattice QCD results for the deuteron and the di-neutron binding energy, and the effective range expansion to tune LECs for interaction terms in the two-nucleon sector. Similar to the physical case, the coupling strength of the NNN-contact is adjusted to reproduce the binding energy of lattice triton. As is apparent from Table 2.1, the lattice QCD data has significant uncertainties which will translate to bands of coupling strengths that are equally plausible for any chosen cutoff and regulator function. We choose to use central values as input to optimize LECs. The nucleon mass is 1634 MeV at this

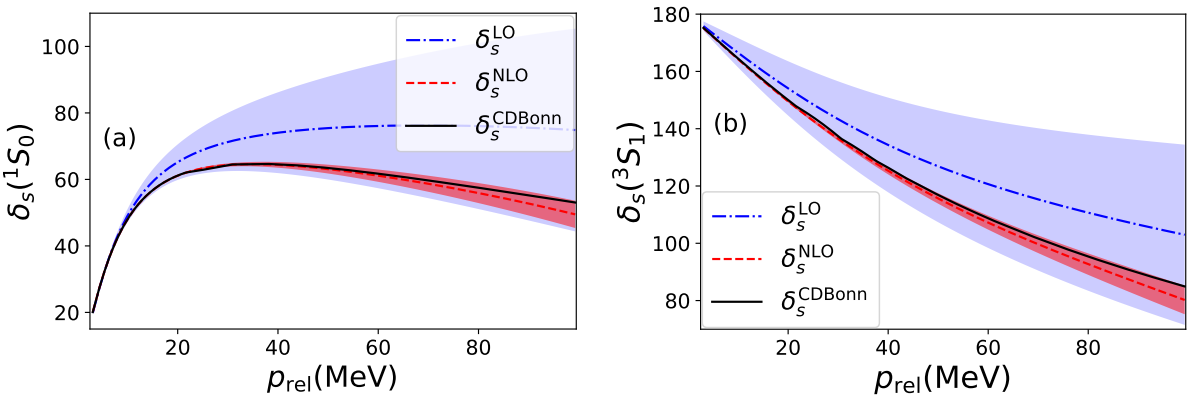

Figure 2.13: (Color online) Phase shifts in the partial waves ${}^1S_0$ (panel (a)) and ${}^3S_1$ (panel (b)) from IR improved potentials at NLO (red dashed) and LO (blue dot-dashed), respectively, in a model space $N = 8, \hbar\omega = 22$ MeV, $l = 0$. The black curves show neutron-proton phase shifts of the CD-Bonn potential. The blue (biggest) and red(smallest) shaded area correspond to EFT uncertainty at LO and NLO, respectively.

pion mass. We obtain the two- and three-body matrix elements by simply employing scaling relations in Eqns. (2.53) to the interaction matrix-elements at the physical pion mass.

We begin with the LO interaction. The LEC in the triplet S channel is adjusted to the deuteron binding energy. Since di-neutron is no longer unbound (unlike nature), we infer the singlet S LEC from di-neutron binding energy. The NNN contact is adjusted to the central value of the triton binding energy. Table 2.4 shows the values of the LO LECs at various cutoffs in a model space with $N = 8$.

Next we turn to the NLO potential. We use data available on the effective range expansion parameters calculated by Beane et al.[11]. In that work, the location of the bound-state was used to constrain the effective range expansion in $k\cot\delta$ to determine the scattering length and the effective range. We obtain the NLO interaction by performing a simultaneous fit to the binding energy and the scattering length in the singlet and triplet S channels. After optimizing the NLO NN interaction, we adjust the coupling strength of the NNN contact to the triton binding energy. The results of the fit are shown in Table 2.5.

Figure 2.14 shows the phase shifts for lattice nuclei obtained at LO (dashed-dotted line) and at NLO (dashed lines). The phase shifts from the effective range expansion (1.9) is shown as a solid black line with grey uncertainty estimates from lattice QCD. The blue

Table 2.4: The LO LECs $\tilde{C}_{^3s_1}$ and $\tilde{C}_{^1s_0}$ (both in 10^{-5}MeV^{-2}), and c_E (dimensionless) for lattice nuclei (with nucleon mass $m = 1634$ MeV) for different cutoffs Λ (in MeV), for oscillator EFT interactions in a model space with $N = 8$.

$\hbar\omega$	Λ	$\tilde{C}_{^3s_1}$	$\tilde{C}_{^1s_0}$	c_E
5	306.52	−1.013613	−0.904019	−1.731712
10	433.48	−0.502300	−0.460312	−0.433930
22	642.96	−0.251429	−0.236527	−0.086293
40	866.97	−0.158373	−0.151299	−0.025688

(biggest) and red (smallest) shaded area correspond to the EFT uncertainties at LO and NLO, respectively, for the interaction optimized to central values of binding energy and effective range expansion parameters in each channel. As expected, the NLO interaction expand the range of momenta for which our results agree with lattice QCD effective range expansion in comparison to LO result in both the channels. Nevertheless (unlike the physical case), at NLO this overlap with the effective range expansion does not extend to momenta as high as ${}^{np}r_{s(t)}^{-1}$ in singlet(or triplet) S channel.

In the following section, we study the effective range parameter r_e (in the effective range expansion (1.9)) for the optimized NLO NN potential at increasingly large cutoffs in our method.

Large UV cutoffs and the Wigner bound

Based on Wigner's bound [85] on the derivative of phase shifts with respect to momentum, Phillips and Cohen[72] showed that the effective range r_e obeys the inequality

$$r_e \leq 2\left(R - \frac{R^2}{a} + \frac{R^3}{3a^2}\right). \tag{2.58}$$

Here, R is the radial extent of the potential, beyond which the short-ranged potential is zero and r_e is the effective range in effective range expansion. As the physical range R is inversely proportional to the ultraviolet cutoff Λ, Wigner's bound [85] shows that at increasingly large cutoffs the effective range parameter cannot be reproduced.

Table 2.5: The NLO LECs $\tilde{C}_{^3s_1}$ and $\tilde{C}_{^1s_0}$ (both in 10^{-5}MeV^{-2}), and $C_{^3s_1}$ and $C_{^1s_0}$ (both in 10^{-10}MeV^{-4}), and c_E (dimensionless) for lattice nuclei (with nucleon mass $m = 1634$ MeV) for different momentum cutoffs Λ (in MeV) for interactions in a model space with $N = 8$.

$\hbar\omega$	Λ	$\tilde{C}_{^3s_1}$	$C_{^3s_1}$	$\tilde{C}_{^1s_0}$	$C_{^1s_0}$	c_E
5	306.52	−0.736443	−1.034289	−1.216789	1.180748	−1.719559
10	433.48	−0.632458	0.246988	−0.854814	0.760970	−0.430321
22	642.96	−0.449998	0.177545	−0.691412	0.423704	−0.076720
40	866.97	−0.387445	0.118521	−0.853482	0.471613	−0.106436

To verify this relation for the oscillator regulated NLO NN pionless EFT potential, we repeatedly optimize the NLO NN LECs in the singlet S channel to the low-energy phase shifts for cutoffs between 200-6000 MeV. Figure 2.15 shows the singlet S effective range (red curve) that we get using optimized NLO in finite harmonic oscillator basis with $N = 8$, while corresponding Wigner's bound (2.58) is shown by solid dots. We see that the EFT in the harmonic oscillator basis obeys the Wigner bound. For very large cutoffs the effective range approaches zero. It is important to note that for physical nuclei, we are unable to reproduce the effective range of the NN interaction beyond $\Lambda_{\text{UV}} \approx 650$ MeV. In the lattice case, we could not reproduce the central triton binding energy in LQCD data using NLO potentials regulated by oscillator frequencies $\hbar\omega > 40$.

2.5 Conclusions

We briefly summarize the key results of this chapter. We used the momentum-space DVR for finite harmonic oscillator basis to implement pionless EFT. The DVR projection of original potential introduces large oscillations which leads to incorrect behavior of the EFT potential at very low energies. In Ref. [16], these oscillations were remedied to some extent by employing external momentum-space regulator functions with momentum cutoff much larger than ultraviolet cutoff (2.2) of the finite oscillator basis. We on the other hand, developed a method called infrared improvement in which the DVR potential at zero momentum was corrected using highest DVR point. The hallmark of our approach is that we tailor the

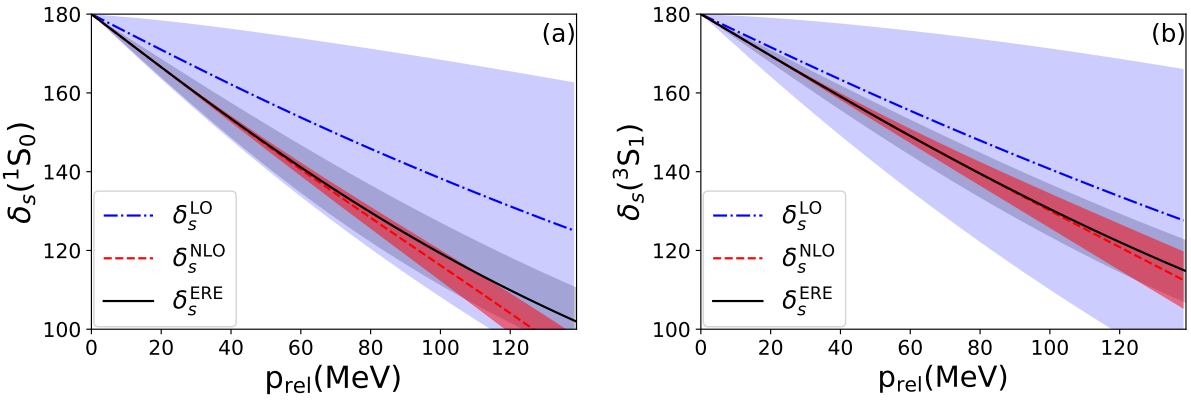

Figure 2.14: (Color online) Phase shifts for lattice nucleons at $m_\pi = 806$ MeV in the partial waves $^1S_0$ (panel (a)) and $^3S_1$ (panel (b)) from IR improved potentials at NLO (red dashed) and LO (blue dot-dashed), respectively, in a model space $N = 8, \hbar\omega = 22$ MeV. The black curves shows the effective range expansion from lattice QCD [11] with corresponding systematic plus statistical uncertainties shown as a grey band. The blue (biggest) and red (smallest) shaded area correspond to EFT uncertainties at LO and NLO, respectively, once the interaction is optimized to the central values of the binding energy and the effective range expansion parameters from lattice QCD results by Beane et al.[11].

interaction to finite harmonic oscillator basis by using oscillator space itself as the regulator. We showed in great detail how to implement this for NN and NNN potentials.

In Appendix B, we explore an alternative to infrared improvement. We develop a momentum-space DVR for oscillator basis for which $k = 0$ is a DVR point. We found that with this DVR we could optimize the pionless EFT potential to low-energy phase shifts but the infrared-improved potentials used in the rest of our work have better agreement with data.

In particular, we discovered that in the case of NNN contact the finite hyper-spherical oscillator basis is the ideal regulator because it exactly imitates the truncation (2.50) employed on three-body basis states while performing many-body calculations in Jacobi coordinates.

The infrared-improved potential indeed yield smooth NN phase shift at low energies. Thus, allowing accurate optimization of LECs to binding energy of deuteron (also di-neutron at unphysical pion mass) and effective range expansion. In our approach, the cutoff of the potential can be varied by either changing the model space size N or oscillator spacing

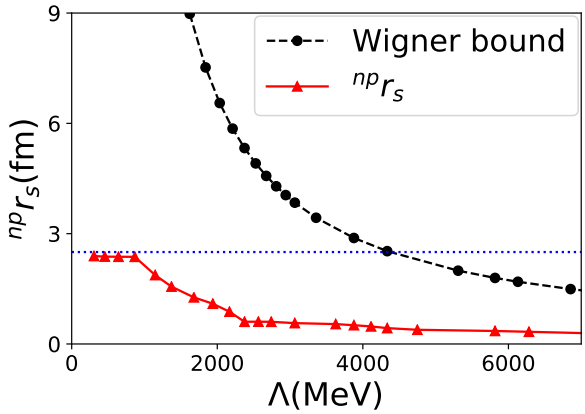

Figure 2.15: The computed neutron-proton effective range in the singlet S wave (red line) as a function of the ultraviolet cutoff in comparison to the physical value shown by dotted line. The black dashed line shows Wigner's bound.

$\hbar\omega$. The oscillator regulated interactions with identical cutoff but different combinations of basis parameters simply translate to different regulator functions. To facilitate many-body computation, we keep N fixed and vary cutoff by changing oscillator spacing. Doing so also has an advantage that we need to compute interaction matrix elements at one cutoff and nucleon mass, because of the scaling relations (2.53). For consistency, we also optimized oscillator EFT interaction for different number of oscillator states at same cutoff $\Lambda \approx 487$ MeV. We found that different number of oscillator states at same cutoff is equivalent to different regulators for the NN and NNN potentials. These results are presented in Appendix A.

We are limited to cutoffs below 650 MeV (at physical pion mass) because beyond that physical range of the oscillator NN potential becomes too small to reproduce effective range parameter in low energy expansion (1.9) for NN scattering, see Figure 2.15. This gives us a moderately large window of cutoffs (200-650 MeV) to study cutoff dependence of many-body results at physical pion mass. For lattice nuclei, for oscillator frequencies $\hbar\omega > 40$, we could not reproduce the central triton binding energy in LQCD data. Thus, for lattice nuclei we are limited to higher cutoff of about 860 MeV.

Since finite oscillator regulated NN interaction breaks down at a moderate ultraviolet cutoff of about 650 MeV at physical pion mass (and 860 MeV at heavier pion mass), we limit

our many-body calculations to these cutoffs. In the following section, we use the optimized LO and NLO pionless EFT interactions to compute ground-state properties of alpha particle at physical and unphysical pion mass as a benchmark for our approach.

Chapter 3

Nuclei with mass number $A \leq 4$

3.1 Atomic nuclei ^{3,4}He

First, we use LO pionless EFT potential as an input to the no-core shell model in Jacobi coordinates. We study the light nuclei with and without the NNN contact. Our results for the binding energy and the point-proton radius of triton, ^{3}He and ^{4}He nuclei are shown in Table 3.1.

The binding energy and radius both exhibit strong cutoff dependence for all the three nuclei, when calculated using only NN interaction at LO. Not only that, the binding energy of the triton and the alpha particle also exhibit a linear correlation parametrized by the cutoff (commonly known as Tjon line) as shown by solid line in Fig. 3.1. It is clear that one needs the NNN contact already at LO to make the results renormalization group invariant i.e., independent of the cutoff, as was first demonstrated by Bedaque et al. [14]. Once the NNN force is included, the alpha particle binding energy and radius show a milder cutoff dependence. This remaining variation is consistent with the 30% uncertainty from neglected higher order terms at LO. We find an under bound ^{4}He with respect to its experimentally known binding energy $E(^4\text{He}) = 28.3$ MeV which is consistent with results at similar cutoffs in Ref. [49].

We repeat our calculations using NLO pionless EFT interaction without NNN force. These results are shown in top part of Table 3.2. Also, the blue dots in Figure 3.1 show that the resultant triton and alpha binding energies are correlated via the Tjon line again

Table 3.1: Binding energies (in MeV) and point-proton radii (in fm^{-1})of $A \leq 4$ nuclei using NN and $NN + NNN$ pionless EFT interactions at LO and defined in model space $N = 8$.

LO NN							
$\hbar\omega$	Λ	$E(^3\text{H})$	$r(^3\text{H})$	$E(^3\text{He})$	$r(^3\text{He})$	$E(^4\text{He})$	$r(^4\text{He})$
5	232.35	8.65	1.78	8.04	1.89	26.81	1.79
10	328.59	13.34	1.31	12.49	1.37	45.45	1.28
22	487.38	23.69	0.91	22.46	0.95	88.06	0.87
40	657.19	38.31	0.69	36.65	0.71	149.88	0.65
LO $NN + NNN$							
$\hbar\omega$	Λ	$E(^3\text{H})$	$r(^3\text{H})$	$E(^3\text{He})$	$r(^3\text{He})$	$E(^4\text{He})$	$r(^4\text{He})$
5	232.35	8.482	1.79	7.87	1.90	26.05	1.79
10	328.59	8.482	1.46	7.71	1.60	22.40	1.44
22	487.38	8.482	1.29	7.54	1.46	17.66	1.46
40	657.19	8.482	1.23	7.41	1.42	17.55	1.42

at NLO. This result is similar to the observation made in Ref.[73] using several realistic NN potentials. Although the cutoff dependence of the alpha particle binding energy is not as large as it is with LO NN potential only, its still not consistent with expected uncertainty of 10% at NLO in pionless EFT. From our results in Table 3.2 with NNN contact included, it is clear that the NNN force remedies this issue. Moreover, ^{4}He and other nuclei at all cutoffs lie within 10% of experimental data [$E(^3\text{He}) = 7.5$ MeV, $E(^3\text{H}) = 8.48$ MeV].

3.2 Lattice nuclei ^{3,4}He

We begin with the LO potential. Table 3.3 exhibits our results for light lattice nuclei (i.e., mass number $A \leq 4$) using only LO NN potential in comparison to our results after including NNN force. The NN interaction produces binding energies that almost double over the considered cutoff range. Similar to the atomic case, the binding energies of the triton and the alpha particle form a Tjon line as shown by the dashed-dotted curve in Figure 3.1. Once we include the NNN contact, this dependence reduces and the LO ^{4}He results at all cutoffs are within 50% (LO EFT uncertainty at this pion mass) of the lattice ^{4}He binding energy datum, $E(^4\text{He}) = 107 \pm 24.2$ MeV [12].

Table 3.2: Binding energies (in MeV) and point-proton radii (in fm^{-1}) of $A \leq 4$ nuclei using NN and $NN + NNN$ pionless EFT interactions at NLO and defined in model space $N = 8$.

NLO NN							
$\hbar\omega$	Λ	$E(^3\text{H})$	$r(^3\text{H})$	$E(^3\text{He})$	$r(^3\text{He})$	$E(^4\text{He})$	$r(^4\text{He})$
5	232.35	7.94	1.82	7.35	1.97	25.03	1.80
10	328.59	10.11	1.49	9.34	1.61	36.24	1.34
22	487.38	8.62	1.62	7.90	1.82	30.39	1.41
40	657.19	8.97	1.62	8.30	1.77	29.95	1.53
NLO $NN + NNN$							
$\hbar\omega$	Λ	$E(^3\text{H})$	$r(^3\text{H})$	$E(^3\text{He})$	$r(^3\text{He})$	$E(^4\text{He})$	$r(^4\text{He})$
5	232.35	8.482	1.80	7.88	1.93	27.52	1.79
10	328.59	8.482	1.59	7.75	1.75	27.30	1.43
22	487.38	8.482	1.63	7.77	1.83	29.30	1.44
40	657.19	8.482	1.65	7.82	1.82	27.35	1.58

There is no data for the point-proton radius of lattice ^{4}He from lattice QCD calculations. Therefore, we compare our result to Ref. [20], the only other calculation available at this time. For the cutoff range that we consider, our result is within EFT uncertainty of their radius calculations. Having said that, the point-proton radius in our calculations is on the larger side and does not fall as quickly as their results with increasing cutoff.

Now we use the NLO interaction to recompute these nuclei. Table 3.4 compares our NLO binding energy and point-proton radius for light lattice nuclei using only NN part of the potential against those which include NNN force. For the results with only NN interactions we make two observations. First, the NLO triton and alpha particle binding energies are related via Tjon correlation (similar to the atomic case) as marked by rightward triangles in Figure 3.1. Second, the variation in the ^{4}He binding energy with changing cutoff is much higher than the expected 25% from neglected higher order terms in EFT interaction. After including the NNN force, the cutoff variation reduces further and the ^{4}He binding energy falls closer to lattice QCD data.

We remind ourselves that lattice QCD data in Table 2.1 (which we use to optimize EFT) has significant uncertainties. When we repeat our calculations for upper and lower limits of input binding energies, ^{4}He binding energy varies between 140 MeV and 60 MeV. This

Table 3.3: Binding energies (in MeV) and point-proton radii (in fm^{-1}) of $A = 3, 4$ lattice nuclei at $m_\pi = 806$ MeV using NN and $NN + NNN$ pion-less EFT interactions at LO in model space $N = 8$.

LO NN							
$\hbar\omega$	Λ	$E(^3\text{H})$	$r(^3\text{H})$	$E(^3\text{He})$	$r(^3\text{He})$	$E(^4\text{He})$	$r(^4\text{He})$
5	306.52	64.3	1.57	64.5	1.57	142.7	1.62
10	433.48	76.6	1.13	75.6	1.13	177.5	1.17
22	642.96	99.1	0.78	97.6	0.79	249.6	0.80
40	866.97	127.4	0.60	125.5	0.60	344.7	0.60
LO $NN + NNN$							
$\hbar\omega$	Λ	$E(^3\text{H})$	$r(^3\text{H})$	$E(^3\text{He})$	$r(^3\text{He})$	$E(^4\text{He})$	$r(^4\text{He})$
5	306.52	53.9	1.55	53.1	1.55	98.9	1.57
10	433.48	53.9	1.13	52.9	1.13	88.5	1.15
22	642.96	53.9	0.84	52.5	0.85	70.8	1.05
40	866.97	53.9	0.72	52.2	0.74	68.3	1.09

implies that the uncertainty in computed observables due to uncertainty in lattice QCD input is much larger than the uncertainty from truncation of EFT potential. Nevertheless, we limit our simple uncertainty estimates for all lattice nuclei to the case where LECs are fit to central values of input lattice QCD data.

In the following section, we explain the Tjon correlation [78] between binding energies of $A = 3$ and $A = 4$ nuclei when computed using leading order pionless EFT NN potential in oscillator basis.

3.3 Explanation for Tjon correlation

We use the scaling relations in Eq. (2.53) to explain the increase in binding of the three-nucleon system with increasing cutoff of the NN interaction (also known as Thomas effect [77]) where we vary the cutoff of the interaction by changing oscillator spacing $\hbar\omega$ at fixed N. It can further be extended to analytically understand the Tjon line [78] which is the linear correlation between the triton and ^{4}He binding energies, parameterized by an interaction cutoff.

Table 3.4: Binding energies (in MeV) and point-proton radii (in fm^{-1}) of $A = 3, 4$ lattice nuclei at $m_\pi = 806$ MeV using NN and $NN + NNN$ pionless EFT interactions at NLO in model space $N = 8$.

NLO NN							
$\hbar\omega$	Λ	$E(^3\text{H})$	$r(^3\text{H})$	$E(^3\text{He})$	$r(^3\text{He})$	$E(^4\text{He})$	$r(^4\text{He})$
5	306.52	65.2	1.57	64.4	1.57	142.5	1.61
10	433.48	75.8	1.12	74.8	1.13	176.3	1.16
22	642.96	85.4	0.84	84.0	0.88	217.2	0.82
40	866.97	64.6	1.07	63.7	1.21	139.9	1.23
NLO $NN + NNN$							
$\hbar\omega$	Λ	$E(^3\text{H})$	$r(^3\text{H})$	$E(^3\text{He})$	$r(^3\text{He})$	$E(^4\text{He})$	$r(^4\text{He})$
5	306.52	53.9	1.55	53.1	1.55	99.0	1.55
10	433.48	53.9	1.14	52.9	1.16	89.9	1.17
22	642.96	53.9	1.04	52.7	1.13	89.7	1.34
40	866.97	53.9	1.17	53.1	1.29	109.7	1.33

We recall that the oscillator spacing $\hbar\omega(\equiv \frac{\hbar^2}{\mu b^2})$ is the unit of energy eigenvalues in oscillator basis, where μ is the reduced mass of two nucleons. Therefore, the Schrödinger equation for two nucleons interacting via LO NN potential, in either singlet or triplet S channel, can be expressed as,

$$\frac{\hbar^2}{mb^2}\left(\hat{t}_2 + m\hbar\frac{C_{\text{LO}}}{b}\hat{v}_2\right)|\psi_2\rangle = E_2|\psi_2\rangle. \tag{3.1}$$

Here, $\hat{t}_2$ and $\hat{v}_2$ are dimensionless matrices of the kinetic and potential energies, respectively. Subscript '2' represents the number of nucleons in the system that this equation describes. Thus,

$$\left(\hat{t}_2 + m\hbar\frac{C_{\text{LO}}}{b}\hat{v}_2\right)|\psi_2\rangle = \frac{E_2}{\hbar\omega}|\psi_2\rangle \approx 0. \tag{3.2}$$

In the limit of an infinite scattering length or a zero-energy eigenstate, the approximation of the Schrödinger equation to zero is exact. It is also a valid approximation for model spaces $E_2 \ll \hbar\omega$. In the above equation, the coefficient of $\hat{v}_2$ is the only scale dependent quantity which leads to the conclusion,

$$\frac{C_{\text{LO}}}{b}m\hbar = \text{const.} \tag{3.3}$$

This relation implies $C_{\rm LO} \propto (\hbar\omega)^{-1/2}$ for an oscillator regulated LO pionless EFT NN potential; equivalent to the relation $C_{\rm LO} \propto (m\Lambda)^{-1}$ in momentum-space formulation of pionless EFT (recall that earlier we found same relation for step and Gaussian regulators) at infinite scattering length.

We examine the Schrödinger equation for an A-body system, in light of the $\hbar\omega$ dependence of the LO low-energy coefficient. For the dimensionless kinetic energy matrix $\hat{t}_A$ and the potential energy matrix $\hat{v}_A$ of the A-nucleon system, interacting via the same LO NN interaction, Eq. (3.1) can be generalized to

$$\begin{aligned} E_A|\psi\rangle &= \frac{\hbar^2}{mb^2}\left(\hat{t}_A + m\hbar\frac{C_{\rm LO}}{b}\hat{v}_A\right)|\psi_A\rangle \\ &= \hbar\omega\hat{h}_A|\psi_A\rangle. \end{aligned} \tag{3.4}$$

Due to relation (3.3), the resultant A-body Hamiltonian matrix $\hat{h}_A$ is dimensionless and scale independent. Consequently, the A-nucleon binding energy

$$E_A \propto \hbar\omega. \tag{3.5}$$

This derivation clearly illustrates Thomas effect [77] i.e., the binding energy of $A = 3$ nuclei increases with increasing cutoff (or decreasing spatial range) of the NN interaction, and demonstrates that NN interaction alone will not renormalize any $A \geq 3$ system (as was first studied in Ref. [14]).

An artifact of the large two-nucleon scattering length, Eqn. (3.5) also explains the Tjon correlation [78] between the binding energies of the $A = 3$ and $A = 4$ nuclei, both of which inherently depend on cutoff the two nucleon interaction [73]. Although our simple derivation is invalid for lattice nuclei, as $E_2 \approx 0$ or $E_2 \ll \hbar\omega$ are not good approximations for Eqn. (3.2) at heavier pion mass, we still expect the Thomas effect and the Tjon line for the lattice case because two-nucleon scattering length remains large (almost double) in comparison to the effective range ${}^{np}r_s$ (or ${}^{np}r_s$). Figure 3.1 shows the Tjon line formed by triton and ^{4}He binding energy, computed using LO NN interaction, for both atomic (solid line) and lattice (dashed-dotted line) case; this plot uses results from Tables 3.1 and 3.3.

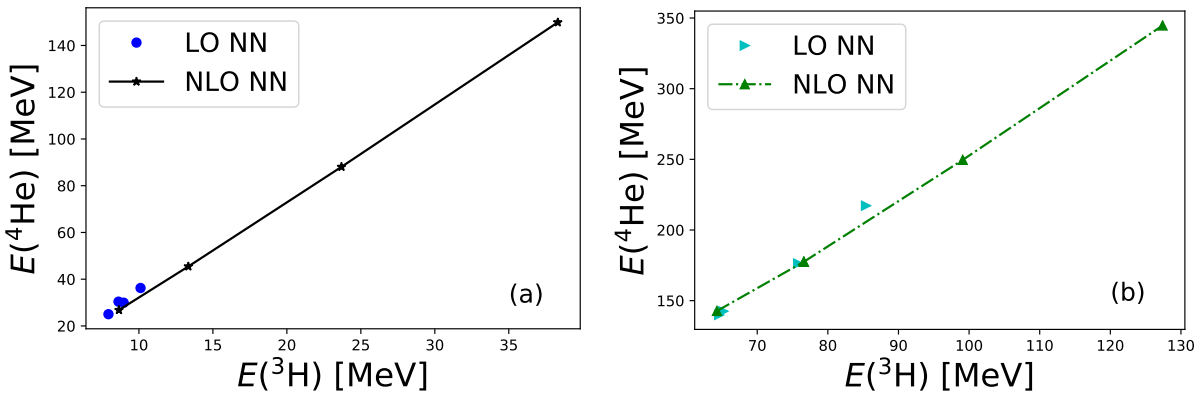

Figure 3.1: (Color online) Correlation between the triton and ^{4}He binding energies, computed in LO and NLO with NN interactions from pionless EFT for the physical nuclei in Panel(a) and for the lattice nuclei in Panel(b). Black stars (solid dots) show the Tjon correlation at physical pion mass using LO (NLO) NN pionless EFT potential, and rightward (upward) triangles show the same at an unphysical pion mass of 806 MeV with LO (NLO) NN potential. Different points correspond to different ultraviolet cutoffs.

Previous studies hints that the binding energy of nuclei with mass numbers $A \geq 4$ are also governed by the unnaturally large scattering length of two-nucleon systems and the three-body force to renormalize three body system, with no additional four- or higher many-body forces required at leading order. For instance, the LO binding energy calculation of ^{6}Li [76] and ^{6}He [48] converge with respect to interaction cutoff. It is encouraging that our simple analysis also suggests the same. Note that the scaling relation (3.5) holds true for nuclei with mass number $A > 4$. Therefore, in the future we can use our oscillator EFT potential to compute $A = 5, 6, ...$ nuclei to investigate existence of generalized Tjon line in A-fermion systems; which has already been successful for similar contact EFT study of systems containing upto six bosons [8].

3.4 Infrared extrapolations and oscillator EFT

The finite oscillator basis introduces an effective hard-wall at a radius L (2.1) and Λ (2.2) in coordinate and momentum space, respectively. Thus, when solving for nuclei one has to worry about performing infrared extrapolations [30] and ultraviolet extrapolations [52] to remove finite-volume effects. The ultraviolet extrapolations are more difficult because

they depend on the short-range behavior of the interaction. To remedy this, we successfully tailored EFT interaction and the regulator to harmonic oscillator basis. In this section, we focus on infrared extrapolations of the binding energy of $A = 2, 3$ and 4 nuclei computed using oscillator EFT potential.

The infrared extrapolation are required because Dirichlet boundary condition at $r \approx L$, changes the curvature of bound-state wave function, which is otherwise exponentially decaying. The resultant infrared correction to the binding energy is [30],

$$E(N_{\max}) = E_\infty + a_0 e^{-2k_\infty L} \tag{3.6}$$

Here, E_∞, k_∞ and a_0 are fit to binding energy calculations $E(N_{\max})$ for at least three separate model space sizes which correspond to different L's. The relation between $N_{\max}$ and L depends on number of particles and many-body basis i.e., whether it is a product space [32] (as we have in coupled-cluster method) or no-core shell model space [84] (where truncation is on the total energy that is a many-body operator). In case of deuteron, the fit parameter k_∞ is related to the deuteron binding energy [34],

$$B = \frac{\hbar^2 k_\infty^2}{2\mu}. \tag{3.7}$$

Here, μ is the reduced mass of the NN system.

In this paragraph, we discuss the physical significance of k_∞ in case of an A-body nucleus in a no-core shell model space (similar study for many-body systems on a cubic lattice is found in the work by König and Lee[53]). In the no-core shell model space, the truncation on the total energy implies an effective hard-wall boundary condition on translationally invariant hyper-radius $\vec{\rho}^2 = \sum_{i=1}^{A-1} \vec{\rho}_i^2$ such that,

$$\sum_{i=1}^{A-1} \vec{\rho}_i^2 = \sum_{j=1}^{A} \vec{r}_i^2 - A\vec{R}_{\rm cm}^2. \tag{3.8}$$

Here, $\vec{r}_i$ is the position vector of nucleon i, ρ_i represents Jacobi coordinates, and $\vec{R}_{\rm cm} = \sum_{i=1}^{A} \vec{r}_i/A$ is the center-of-mass coordinate for A nucleons. Thus, we can choose between

different normalizations for $(A-1)$ Jacobi coordinates and the resultant center-of-mass coordinate that fulfills Eqn. (3.8). In the no-core shell model, one works with democratic Jacobi coordinate where reduced mass corresponding to each Jacobi and the center-of-mass coordinate is the nucleon mass m. Thus, all Jacobi oscillators have the same oscillator length.

To understand the infrared extrapolation, we define the coordinate $\vec{\rho}_1$ that connects subsystems of the lowest break-up channel. For instance, for a triton separating into a deuteron and a neutron we have $\vec{\rho}_1 = \sqrt{2/3}\Big(\vec{r}_3 - (\vec{r}_1 + \vec{r}_2)/2\Big)$, and for alpha particle separating to triton and proton we have, $\vec{\rho}_1 = \sqrt{3/4}\Big(\vec{r}_4 - (\vec{r}_1 + \vec{r}_2 + \vec{r}_3)/3\Big)$. Thus, in the asymptotic limit i.e., $\rho_i \to \infty$, the A-nucleon wave function will fall as $e^{-k_1\rho_1}/\rho_1$. Thus, $\vec{k}_1 = \vec{k}_{\rm sep}$ where $\vec{k}_{\rm sep}$ gives the lowest separation energy S,

$$S = \frac{\hbar^2 k_{\rm sep}^2}{2m}. \tag{3.9}$$

where m is the nucleon mass (due to our choice of democratic Jacobi coordinates). Thus, we find that the fit parameter k_∞ is the separation momentum $k_{\rm sep}$ of the lowest-energy decay channel in A-nucleon system and shares relation (3.9) with the corresponding separation momentum. This insight is my contribution to our paper [29].

We expect k_∞ in case of the deuteron, the triton and the alpha particles to reproduce the theoretical lowest separation momentum of these nuclei from our NLO potentials, as oscillator potentials are ultraviolet converged. Our EFT potential is tailored to model space $N = 8$, we increase L (2.1) of the oscillator basis by including kinetic energy matrix of size $N_{\rm max} \geq 8$ in the Hamiltonian. We note that ultraviolet cutoff of the interaction remains unchanged because basis states in the Hamiltonian with energy $E > N\hbar\omega$ continue to have zero interaction strength. We have three fit parameters $(k_\infty, a_0, E_\infty)$ for binding energy extrapolation formula. Therefore, the first set of values for these three parameters are obtained using the results in the model spaces $N_{\rm max} = 8, 10$ and 12. $N_{\rm max} = 60$ is the largest model space size that we used for the infrared extrapolations.

Let us first consider deuteron at NLO. Figure 3.2 plots the energy difference $\Delta E \equiv E(N_{\rm max}) - (E_{\rm exp})$ as a function of L in Eq. (2.1). We find that ΔE converges exponentially with respect to L for both the oscillator spacings we considered. Solid blue squares (solid

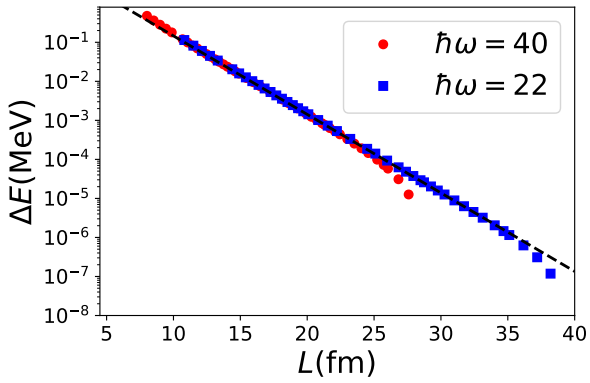

Figure 3.2: Difference of the deuteron binding energy in a finite space of size L and the infinite-space result for $\hbar\omega = 40$ MeV (solid red dots) and 22 MeV (solid blue squares) for our NLO oscillator EFT potential in model space $N = 8$. The dashed black line shows $a_0 \exp(-2k_\infty L)$ where $k_\infty \equiv 0.2316$ fm^{-1} is the separation momentum.

red dots) show the results for $\hbar\omega = 40$ MeV (22 MeV) which exactly overlap with black dashed line representing $\exp(-2k_\infty L)$ with actual separation momentum $\sqrt{2\mu E_{\rm exp}}/\hbar = 0.2316$ fm^{-1}. Indeed, infrared extrapolation yields a very accurate deuteron separation momentum, which has better agreement that the result in Ref. [66].

Now we look at our results for triton using NLO oscillator potential at one of the cutoffs ($\hbar\omega = 22$ MeV). We remind the reader that for $A \geq 3$ nuclei in no-core shell model space, the effective hard-wall at L is slightly different from Eqn. (2.1). So, we use L for varying $N_{\rm max}$ from Ref. [84]. Figure 3.3 compares our result no-core shell results $E(N_{\rm max})$ in finite oscillator space (shown as black squares) with the extrapolated value E_∞ (shown as red circles) as a function of L. From the second data point onwards i.e., $N_{\rm max} \geq 14$, the infrared extrapolated energy yields the infinite volume result at NLO.

Further, we compare the k_∞ from our infrared extrapolations to separation momentum $k_{\rm sep}$ in the lowest break-up channel for triton i.e., to deuteron and a neutron. In light of equation (3.9), the corresponding separation energy is,

$$\frac{\hbar^2 k_{\rm sep}^2}{2m} = E(^3{\rm H}) - E(^2{\rm H}), \tag{3.10}$$

where $E(^3{\rm H})$ and $E(^2{\rm H})$ are our NLO results for triton and deuteron binding energies, respectively at fixed L. Figure 3.4 compares the k_∞ from extrapolation with the theoretical

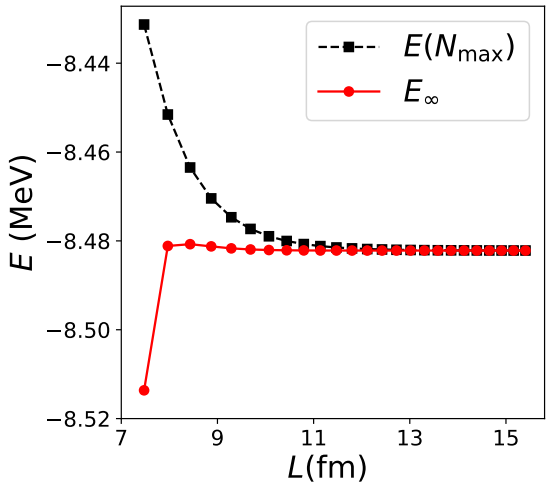

Figure 3.3: (Color online) Ground-state energy (black squares) of ^{3}H computed in a model space of $N_{\max}+1$ shells and compared to the infrared extrapolated result E_∞ (red circles).

value of $k_{\rm sep}$ as a function of L. The two curves never overlap i.e, both quantities are slightly different. We do not understand the reason for this small discrepancy.

Now, we repeat the analysis for our no-core shell model results for ^{4}He nucleus at NLO at oscillator spacing $\hbar\omega = 40$ MeV. The lowest break-up channel for alpha particle is to triton and a proton. Thus, the separation momentum $k_{\rm sep}$ will satisfy

$$\frac{\hbar^2 k_{\rm sep}^2}{2m} = E(^4\mathrm{He}) - E(^3\mathrm{H}). \tag{3.11}$$

Here, $E(^4\mathrm{He})$ and $E(^3\mathrm{H})$ are the theoretical result for the ^{4}He and the triton binding energy, respectively. Figure 3.5 compares the NCSM results $E(N_{\max})$ for the alpha particle with E_∞ from extrapolation as a function of L (all dependent on $N_{\max}$). As the basis size increases, both curves approach each other and the change in extrapolated energies (shown by red curve) also reduces. However, convergence is not fully achieved in accessible model spaces. Next, we compare the theoretical separation momenta and k_∞ obtained from infrared extrapolation in Figure 3.6. Similar to the case of triton, both quantities are comparable but not exactly the same. We do not understand the reason for this difference; here it could be because the extrapolated parameters are not fully converged or due to proximity of the breakup channel through which the alpha particle decays to the ^{3}He nucleus and a neutron.

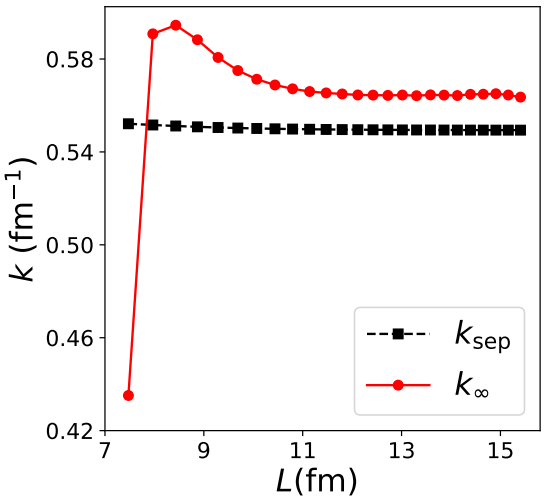

Figure 3.4: (Color online) Separation momentum (black squares) of ^{3}H computed in a model space of $N_{\max}+1$ shells and compared to the infrared extrapolated result k_∞ (red circles).

3.5 Conclusions and Open Questions

We used the pionless EFT potential in oscillator basis to study ground state properties of $A = 3, 4$ nuclei, at physical and unphysical pion mass (see Tables 3.1, 3.2, 3.3, and 3.4). With full LO and NLO potentials, the cutoff dependence ^{4}He binding energy is within our expectation from simple EFT uncertainty estimates and are close to experimental data for the atomic case, and lattice QCD data for lattice ^{4}He.

At LO without three nucleon contact, large cutoff dependence for light nuclei. For both physical and lattice nuclei, we confirm linear correlation between triton and alpha particle binding energy (see Figure 3.1). Moreover, due to scaling relations (2.53) at fixed N, oscillator EFT provides us with an analytical explanation for Tjon correlation at physical pion mass. Using the non-perturbative NLO NN potential, we find that the cutoff dependence of the $A = 3, 4$ nuclei reduces significantly and results come closer to data, but the variation with cutoff is greater than the EFT uncertainties at this order for both pion masses.

We studied the quality of infrared extrapolations for binding energies of $A = 2, 3$ and 4 nuclei at NLO using Eqn. (3.6). In addition we showed that the extrapolation fit

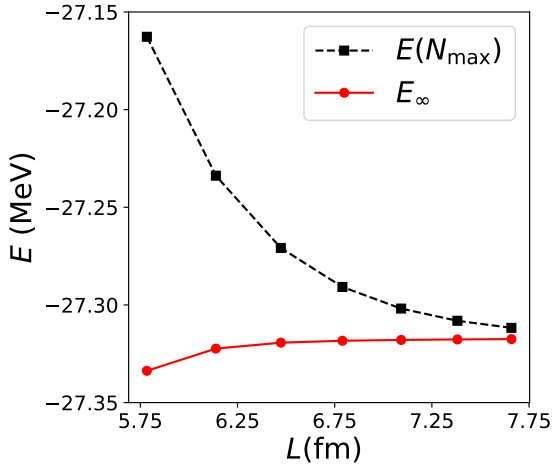

Figure 3.5: (Color online) Ground-state energy (black squares) of ^{4}He computed in a model space of $N_{\max}+1$ shells and compared to the infrared extrapolated result E_∞ (red circles).

parameter k_∞, for the A-body nucleus in democratic Jacobi coordinates, corresponds to the separation momentum $k_{\rm sep}$ for the lowest energy break-up channel of that nucleus such that the separation energy S is given by (3.9). For the deuteron, there is a great agreement between the deuteron separation momentum and k_∞ (shown in Figure 3.2). In the case of the triton the extrapolated energy E_∞ converges quickly with model space size. However, the k_∞ from extrapolation predicts slightly higher separation momentum for its separation into deuteron and a neutron (see Figs. 3.3 and 3.4). For the alpha particle, we find that the no-core shell model binding energies are not fully converged even in the largest model space that we considered; the extrapolated energy E_∞ shows small changes as data points for larger model spaces are included in the fit (see Figure 3.5). The parameter k_∞ from extrapolation, although close to the separation momentum $k_{\rm sep}$ (for break-up into triton and a proton), are also not the same (see Figure 3.5). It remains an open question why $k_{\rm sep}$ and k_∞ in nuclei $A=3,4$ do not match, given that there are no missing ultraviolet corrections.

Our simple explanation for Tjon correlations between $A=3$ and $A=4$ fermion systems, hints at the existence of generalized Tjon line correlations for heavier systems (when the underlying two-fermion system has a large scattering length and the two-body bound state is close to threshold); there also exists empirical evidence for it [17]. Such correlations have

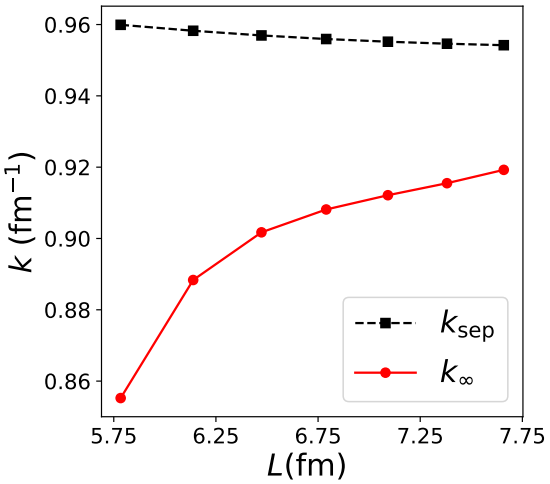

Figure 3.6: (Color online) Separation momentum (black squares) of ^{4}He computed in a model space of $N_{\max}+1$ shells and compared to the infrared extrapolated result k_∞ (red circles).

already been successfully studied in systems with up to six-bosons [8]. In the future, we can use LO oscillator EFT potentials to study $A = 5, 6, \ldots$ nuclei and verify this.

Further, it is clear that we needed infrared improvement for pionless EFT implementation in the harmonic oscillator basis; otherwise we cannot reliably reproduce low-energy phase shifts. However, its relevance in the context of nuclear structure calculations is an open question. Relation (3.9) suggests that the lowest momentum scale that is relevant for the ground state property of an A-nucleon system is really the separation momentum for lowest energetic break-up channel. For most nuclei, this separation momentum is larger than the deuteron binding energy. Our infrared extrapolations for the triton and the alpha particle also support this argument. So, it is hard to say how sensitive the ground state properties of bound nuclei are to the behavior of the interaction close to $k = 0$ momentum.

Chapter 4

Medium-mass nuclei using pionless EFT

4.1 Results for ^{16}O and ^{40}Ca

We use the finite oscillator basis regulated pionless EFT potentials to compute ^{16}O and ^{40}Ca nuclei with the coupled-cluster method [55, 6, 37], performed in the coupled-cluster singles and doubles (CCSD) approximation. The computational complexity of many-body methods, like no-core shell model, increases factorially with increasing number of nucleons. The coupled cluster method reduces it to a polynomial cost and therefore is at the forefront of the ongoing effort to push nuclear structure calculations to heavy nuclei using EFT potentials. In coupled cluster one computes the Hamiltonian $\bar{H}$, obtained by performing a similarity transformation on the starting Hamiltonian H, such that the A-body product state in single-particle basis becomes the eigenstate of the similarity-transformed Hamiltonian. In CCSD, the similarity transformed Hamiltonian only decouples 1particle-1hole ($1p-1h$) and $2p-2h$ excitations from the A-body reference state in second quantization. Coupled cluster calculations are performed in the laboratory coordinates. This is important because oscillator EFT interactions are tailored to a finite oscillator space in Jacobi coordinates and the number of matrix elements increase significantly when transforming from the center-of-mass coordinates to single-particle basis in the laboratory frame. Therefore, in practice separate truncation on the maximum energy of a single particle - $N_1\hbar\omega$ - and of three

particles - $N_3\hbar\omega$ - is employed on allowed oscillator basis states in laboratory coordinates. Our expectation is that the oscillator EFT interaction yields converged many-body results with respect to truncations N_1 and N_3. As we shall see, this is indeed fulfilled for some oscillator spacings.

Since coupled cluster calculation is performed in laboratory coordinates, the intrinsic Hamiltonian is translationally invariant,

$$H_{\text{in}} = T - T_{\text{cm}} + V_{NN} + V_{NNN} \tag{4.1}$$

Here, T denotes the total kinetic energy and T_{cm} is the kinetic energy of center of mass. We note that the center-of-mass coordinate is not referenced by the Hamiltonian (4.1).

The coupled-cluster method works efficiently when there is a clear gap between the starting A-nucleon product state in a single particle basis and its particle-hole (p-h) excitation. We recall that NLO pionless interactions are pure S-wave interactions which do not include spin-orbit force that is important to explain known shell-closures beyond ^{40}Ca nucleus, in the nuclear shell-model picture. Thus, we only compute ^{4}He, ^{16}O and ^{40}Ca nuclei at physical and heavier pion mass. At LO, coupled cluster calculations of ^{16}O and ^{40}Ca nuclei do not stabilize because we get unbound nuclei with respect to α-particle emission. Other works also found that ^{6}Li [76] and ^{16}O [20] nuclei are not self-bound when computed using LO pionless EFT interaction. Therefore, we only discuss our NLO results for medium-mass nuclei.

The presence of NNN forces increases the computational cost by orders of magnitude in comparison to the solutions with only NN Hamiltonians. So, the NNN contact in CCSD calculations was implemented in the normal-ordered two-body approximation [36]. The idea behind this approximation is that the contributions from three-body operators can be accurately approximated as contributions by one-particle and two-particle operators acting on the A-body Hartree-Fock reference state (as reference state already has some correlations of the A-body system in comparison to zero vacuum). Thus, the NNN contact has contributions to only Hartree-Fock energy (which is really vacuum energy for the non-trivial vacuum) and to one- and two-body matrix elements that are normal ordered with

respect to the A-body reference state. In chiral EFT, where NNN forces enter at N2LO, this approximation works very well [74]. To make sure that it remains so with our NLO pionless EFT potentials, which has a three-nucleon contact at LO, we compare our CCSD results for ^{4}He with results from no-core shell model that includes all Ap-Ah excitations on zero vacuum. I note that the coupled cluster calculations discussed in the following sections were performed by our collaborators at Oak Ridge National Laboratory.

4.1.1 Atomic nuclei

In CCSD we get 27.5, 27.2, 29.0, and 27.5 MeV using our oscillator regulated NLO interactions in model space size $N = 8$ and oscillator spacings $\hbar\omega = 5$, 10, 22, and 40 MeV, respectively. We compare ^{4}He results given above to the virtually exact no-core shell model results in Table 3.2. Thus concluding that the normal-ordered two-body approximation used for NNN contact is accurate and that the missing $3p$-$3h$ excitations only results in differences of about 1%. We find that the ^{4}He binding energy converges rapidly with N_3. The converged CCSD results reported above are computed in a model space with $N_1 = N_3 = 12$.

The NLO results for ^{16}O and ^{40}Ca are shown in Table 4.1. We find that both nuclei are bound at NLO and that the difference between CCSD and Hartree-Fock (which only decouples $1p$-$1h$ excitations) binding energies of these nuclei is roughly 10%. The reason for the small correlation energy could be the absence of coupling between S- and D-waves at NLO in pionless EFT. We present calculations for two separate model spaces to check convergence of the computed results with respect to N_1 and N_3 i.e., $N_1 = N_3 = 12$ and $N_1 = N_3 = 14$, where $N_3 = 14$ is currently the largest model space for three-nucleons that is computationally feasible. While for ^{16}O calculations the maximum change in binding energy with size of model space is about 3 MeV, for ^{40}Ca we find almost 10% change at 657 MeV interaction cutoff. We observe that only at $\hbar\omega = 22$ MeV, the binding energy for both ^{16}O and ^{40}Ca is converged with respect to truncation N_3 in the three-body basis. For other oscillator spacings the ^{16}O nucleus converges faster than ^{40}Ca. We do not understand the $\hbar\omega$ dependence in N_3 convergence of our results.

We note the particularly high binding energies for ^{40}Ca and ^{16}O nuclei at the lowest cutoff 232 MeV. To understand this result, we calculate the Fermi momentum k_F using

Table 4.1: Binding energy of ^{16}O, ^{40}Ca for model space truncations as indicated, as a function of the cutoff Λ (or the oscillator spacing $\hbar\omega$). All quantities in units of MeV. A star (*) indicates that the energy is approximate and did not yet converge after 1000 iterations of the CCSD equations.

		^{16}O		^{40}Ca	
$\hbar\omega$	Λ	$N_1, N_3 = 12$	$N_1, N_3 = 14$	$N_1, N_3 = 12$	$N_1, N_3 = 14$
5	232.35	174.1	174.8	562.5	569.2
10	328.59	136.8	136.2	421.8	415*
22	487.38	143.1	143.1	405.8	405.8
40	657.19	144.7	146.2	372.2	400.0

binding energy per nucleon in the free gas limit using the relation

$$p_F = \sqrt{\frac{10}{3m}\frac{E}{A}} \tag{4.2}$$

Here, m is the nucleon mass. For ^{40}Ca we find $k_F \approx 210$ MeV and for ^{16}O we get $k_F \approx 185$ MeV; both of which are only slightly smaller than the interaction cutoff of $\Lambda \approx 232$ MeV at $\hbar\omega = 5$ MeV. It implies that the interaction with the lowest cutoff cannot scatter nucleons on, or close to, the Fermi-sphere to momentum states that lie outside. Thus, we limit our analysis of EFT uncertainties and cutoff dependence to calculations done in oscillator spacings higher than 5 MeV.

For oscillator spacings $\hbar\omega = 10, 22$ and 40 MeV, we find the variation in binding energies of ^{16}O and ^{40}Ca nuclei with respect to cutoff is 10%. Also, for these cutoffs, our results show approximately 15% difference from experimental data, $E(^{16}\text{O}) = 127.6$ MeV and $E(^{40}\text{Ca}) = 342.1$ MeV. It is also interesting that the computed binding energies are close to results of Ref. [16], obtained using NLO chiral EFT potential (which unlike pionless EFT includes pions explicitly). In Figure 4.1, we plot the binding energy per nucleon as a function of the ultraviolet cutoff. The dashed lines indicate the probable inconsistency of the results at cutoff 232 MeV because of the closeness between the Fermi momentum and the interaction cutoff. For higher cutoffs it is no longer the case, and our finding is that the NLO pionless

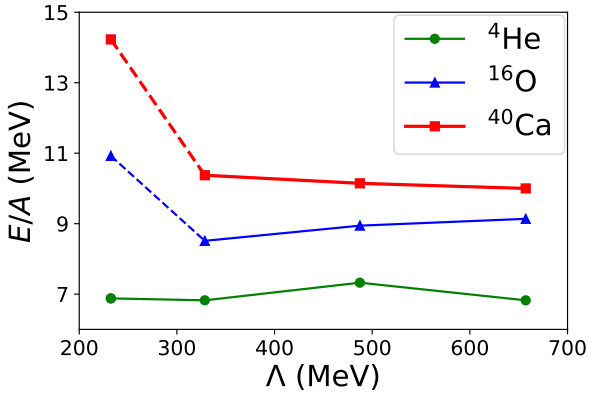

Figure 4.1: (Color online) Binding energy per nucleon for atomic ^{16}O (blue triangles), ^{40}Ca (red squares) nuclei against ultraviolet cutoff of the NLO interaction in the model space $N = 8, l = 0$ from CCSD calculations.

EFT binds ^{16}O and ^{40}Ca nuclei with roughly 9 and 10 MeV binding energy per nucleon, respectively.

In what follows, we use our results to solve the Bethe-Weizsäcker formula

$$E(A) = a_V A - a_S A^{2/3} - a_C \frac{Z^2}{A^{1/3}}. \tag{4.3}$$

for a_V, a_S, a_C, the volume, surface, and Coulomb parameters, respectively. The liquid drop model takes into account bulk properties like volume energy and surface tension to describe nuclear binding energy, where the nucleus with mass number A is treated as a uniform sphere of radius $R \propto A^{1/3}$. The known parameter values are $a_V = 15.49$ MeV, a_S= 17.23 MeV, $a_C = 0.693$ MeV, which are obtained from a global fit for nuclei spread across nuclear chart. The bulk model is not really a good approximation for light nuclei like ^{4}He. Indeed, experimental data for ^{4}He, ^{16}O, and ^{40}Ca gives $a_V = 9.2$ MeV, $a_S = 3.4$ MeV, and an unphysical attractive Coulomb term. As ^{4}He is probably too light to perform a three parameter fit of a bulk formula, we only use our results for ^{16}O and ^{40}Ca at $\hbar\omega = 22$ MeV. To reduce Eq. (4.3) to two parameters we omit the Coulomb term. This yields $a_V = 13.5$ MeV and $a_S = 11.5$ MeV, closer to the empirical values of $a_V \approx 16$ MeV and $a_S \approx 18$ MeV. It is important to remember that the liquid drop model does not include single-particle effects

which lead to nuclear shell structure and therefore, our use of only doubly-magic nuclei is not the most accurate way to calculate bulk parameters.

4.1.2 Lattice nuclei

We re-check the CCSD approximations at heavier pion mass using the NLO potential to compute the ^{4}He binding energy, and compare CCSD results with the no-core shell model results in Table 3.4. In a model space with $N_1 = N_3 = 12; N = 8$, we find $E(^4\text{He}) = 98.0$, 89.0, and 88. MeV at $\hbar\omega = 5$, 10, and 22 MeV, respectively. For these oscillator spacings our CCSD results are in good agreement with the no-core shell model results of Table 3.4. This reveals that the normal-ordered two-body approximation of the NNN potential is 99% accurate, and the neglected triples excitations has very small effect at these cutoffs. On the contary, at $\hbar\omega = 40$ MeV we find a ^{4}He binding energy of 99.5 MeV, which differs from the NCSM result by about 10%. To better understand this discrepancy, we performed CCSD calculation for ^{4}He nucleus with zero NNN coupling strength, and found that it exactly matches NCSM result for NLO NN potential (in Table 3.4). Thus, we find that at $\hbar\omega = 40$ MeV the normal-ordered two-body approximation breaks down. As the normal-ordered two-body approximation is expected to get better with increasing mass number [74], we go on to compute ^{16}O and ^{40}Ca and add additional 10% in the error budget for the results at this frequency. As for the atomic case, CCSD results differ from Hartree-Fock energies only by 10% (revealing a small correlation energy).

We find that lattice ^{16}O and ^{40}Ca nuclei are self-bound at NLO. Our predictions for the binding energy of these nuclei are shown in Table 4.2. For $\hbar\omega = 10$ MeV (i.e., cutoff 433 MeV not shown in the Table), we find $E(^{16}\text{O}) = 371$ MeV and $E(^{40}\text{Ca}) = 832$ MeV. This estimates the Fermi momentum $k_F(^{16}\text{O}) \sim 353$ MeV, and $k_F(^{40}\text{Ca}) \sim 336.58$ MeV in the free Fermi gas limit. These Fermi momenta are close to the cutoff of the interaction at this frequency. Therefore, we believe the oscillator EFT interactions for oscillator spacings $\hbar\omega < 10$ are not equipped to capture physics of lattice ^{16}O and ^{40}Ca. On the other hand, at $\hbar\omega = 22$ MeV we observe binding energy per nucleon for ^{16}O and ^{40}Ca to be about 26 MeV and 30 MeV, respectively. This yields a Fermi momentum of roughly 400 MeV, which is well below the interaction cutoff 640 MeV at this frequency.

Table 4.2: Binding energies of the lattice nuclei ^{16}O, ^{40}Ca for model space truncations as indicated, as a function of the cutoff Λ (or the oscillator spacing $\hbar\omega$). All quantities in units of MeV.

		^{16}O		^{40}Ca	
$\hbar\omega$	Λ	$N_1, N_3 = 12$	$N_1, N_3 = 14$	$N_1, N_3 = 12$	$N_1, N_3 = 14$
22	642.96	429.5	429.5	1187.0	1168.5
40	866.97	547.8	546.0	1252.0	1422.0

Once again our calculations reveal $\hbar\omega$ dependent convergence with respect to three-particle basis size set by N_3. From cutoff variation we find approximately 25% EFT uncertainty which yields $\Delta E_{\rm NLO}(^{16}{\rm O}) \approx 120$ MeV and $\Delta E_{\rm NLO}(^{40}{\rm Ca}) \approx 290$ MeV. At $\hbar\omega = 40$ MeV, there is an additional 10% uncertainty due to inaccuracy of normal-ordered two-body approximation for NNN contact in CCSD. For the uncertainties above, we take 15.9 MeV, 19.5 MeV and 53.9 MeV to be the exact binding energies for the deuteron, di-neutron and triton at $m_\pi = 806$ MeV. These estimates do not include contributions from uncertainty in lattice QCD input, which really is the most dominant uncertainty in case of lattice nuclei. Nevertheless, we find it validating that our binding energy per nucleon is comparable to 25 MeV seen in lattice QCD data for the ^{4}He nucleus [11].

We use our results for ^{16}O and ^{40}Ca at $\hbar\omega = 22$ MeV and $\hbar\omega = 40$ MeV as input to Bethe-Weizsäcker formula (4.3) (omitting the Coulomb term) and solve for surface and volume parameters for lattice nuclei. This yields $a_V \approx 35$ to 40 MeV and $a_S \approx 14$ to 22 MeV.

4.2 Summary and Outlook

We presented first ever calculations for ^{16}O, and ^{40}Ca nuclei using pionless EFT potential at NLO where the pionless EFT potential is regulated by the finite oscillator basis. While at LO ^{16}O and ^{40}Ca are not bound with respect to decay into alpha particles, non-perturbative NLO correction makes these nuclei bound at physical and heavier pion mass. Except for the calculations for which Fermi momentum is borderline to the interaction cutoff, the binding

energy variation with the cutoff are 10% for atomic and 25% for lattice nuclei, the same as observed in the ^{4}He atomic and lattice nucleus at NLO, respectively.

For the atomic case, our results for NLO binding energy are

$$\begin{aligned} E(^{16}\mathrm{O}) &= 143 \pm 15 \text{ MeV}, \\ E(^{40}\mathrm{Ca}) &= 405 \pm 41 \text{ MeV}. \end{aligned} \tag{4.4}$$

In addition, our results are within 20% of exprimental data ($E(^{16}\mathrm{O}) = 127.6$ MeV and $E(^{40}\mathrm{Ca}) = 342.1$ MeV). Interestingly, our NLO pionless EFT results are comparable to NLO chiral EFT results for these nuclei that were reported in Ref. [16]. For a moderate range of cutoffs 330-650 MeV, we find ^{16}O and ^{40}Ca nuclei to have very mild cutoff dependence. On performing a fit for liquid drop model using our ^{16}O and ^{40}Ca results, we found volume paramater $a_V \approx 16$ MeV, and surface parameter $a_S \approx 17$ MeV, which are close to the known values $a_V = 15.49$ MeV, a_S= 17.23 MeV.

From lattice ^{16}O and ^{40}Ca results, we find binding energy per nucleon to be between 26-33 MeV, and 29-36 MeV, respectively for these nuclei. We report these values are close to the binding energy per nucleon from lattice QCD data for ^{4}He nucleus (≈ 25 MeV). For lattice nuclei we find, $a_V \approx 35$ to 40 MeV and $a_S \approx 14$ to 22 MeV for volume and surface parameters in Bethe-Weizsäcker formula. Since lattice QCD calculations are still limited to light nuclei, our results are predictions for the binding energy of ^{16}O and ^{40}Ca at unphysical pion mass $m_\pi = 806$ MeV can serve as a benchmark for future lattice QCD calculations.

The successes above are not without limitations of our approach. We are limited to small cutoff range of 600-850 MeV to study cutoff dependence of lattice ^{16}O and ^{40}Ca nuclei, The lower cutoffs are ruled out due to Fermi momentum's proximity to the cutoff, and at higher cutoffs we fail to optimize NLO potential to lattice QCD data for $A = 2, 3$ systems (probably due to non-perturbative addition of NLO terms). We also note that our current uncertainty estimates do not take into account the significant uncertainty in lattice QCD input (see Table 2.1). To conclude, we have the machinery in place to extrapolate binding energies for medium-mass nuclei at heavier pion masses that are relevant to lattice QCD.

However, further progress relies on the precision of lattice QCD calculations for $A = 2, 3$ systems, that we use as input to pionless EFT.

There also remains an open question in the context of usefulness of oscillator EFT in the presence of NNN force. The main idea behind formulation of EFT interactions in the oscillator basis was to achieve ultraviolet convergence by construction. So that one can simply use infrared extrapolation to obtain infinite-volume result for the observables being computed. We have seen that this approach certainly works in the expected way when many-body calculations are done in Jacobi coordinates (see section 3.4). Unfortunately, the antisymmetrization of translationally invariant wave functions becomes computationally intensive as the number of particles increase. Consequently, computations for most of the $A > 4$ nuclei are done in laboratory coordinates; as we also do in our coupled cluster calculations. We know from Ref. [16] that infrared extrapolation with respect to N_1 works, when many-body observables are computed using NLO chiral EFT potential tailored to oscillator basis in Jacobi coordinates. In contrast to NLO pionless EFT, three nucleon force is absent in NLO chiral EFT potential. Therefore, we had to employ another truncation $N_3\hbar\omega$ on the total energy of three-nucleons in laboratory coordinates. The resultant CCSD results for medium-mass nuclei in Tables 4.1 and 4.2 have $\hbar\omega$ dependent convergence with varying basis truncations N_1 and N_3. Thus, a systematic understanding of such a behavior in laboratory coordinates is important for reliable infrared extrapolation in our framework when a NNN force is present.

Chapter 5

Progress towards Nucleon-Nucleus Effective field theory

5.1 Abstract

We studied the elastic neutron scattering of the closed-core ^{16}O nucleus as an effective two-body problem. The ground state of this nucleus was considered to be a product state of A nucleons with correct point-proton radius. We attempted to construct an effective potential for the incoming nucleon that is optimized to neutron-core elastic scattering cross-sections to predict low-lying excitations in $A+1$ isotope, where A is the number of nucleons in the core. For example, we view ^{17}O nucleus as $^{16}\mathrm{O} + n$, where n represents a neutron. The ^{17}O nucleus is bound with respect to ^{16}O by approximately 4.1 MeV and the first excitation of the ^{16}O nucleus, which we do not explicitly account for in our approach, is roughly 6 MeV. Thus, the low-lying excitations $1/2^+, 5/2^-, 3/2^+, 7/2^-$ of the ^{17}O nucleus at $0.8, 3.84, 5.08, 5.69$ MeV energies, respectively, can in principle be described by the optimized N-A potential.

Our goal is to build systematically improvable nucleon-nucleus potentials that can simultaneously explain data for $A(n,n)A$ scattering process and the low-lying bound states of the $A+1$ nucleus.

5.2 Motivation

Many-body methods like coupled-cluster [54, 37] and In-medium similarity renormalization group method (IM-SRG) [40, 79] solves the many body Hamiltonian by performing a similarity transformation (unitary transformation in case of IMSRG) instead of brute force diagonalization. For instance, coupled cluster performs a similarity transformation

$$\bar{H} = e^{-\hat{T}} H e^{\hat{T}} \tag{5.1}$$

on the starting Hamiltonian H in single-particle basis (which could be Hartree-Fock or harmonic oscillator basis as in nuclear shell-model approach). Here, $\hat{T}$ is the cluster operator of the form

$$\hat{T} = \hat{T}_1 + \hat{T}_2 + \hat{T}_3 + \ldots + \hat{T}_A, \tag{5.2}$$

where,

$$\begin{aligned} \hat{T}_1 &= \sum_{ia} t_i^a a_a^\dagger a_i, \\ \hat{T}_2 &= \sum_{iajb} t_{ij}^{ab} a_a^\dagger a_b^\dagger a_j a_i, \end{aligned} \tag{5.3}$$

and so on. Here, $a_a^\dagger$ creates a particle in single particle state i and a_a annihilates a particle in state a. The indices $i, j, \ldots (\leq A)$ are for single-particle states occupied in the non-trivial vacuum and $a, b, \ldots (\text{suchthat} A < a, b, \ldots < \Omega)$ represent higher states that are initially empty. Thus, $a_a^\dagger a_i$ shifts nucleon from single-particle state i to state a, which creates a hole(h) in the reference state and a particle(p) in the valence space. It is clear that cluster operator $\hat{T}_n$ generates n-particle-n-hole (np-nh) excitations of the A-body product state,

$$|\Phi_0\rangle = \prod_{i=1}^{A} a_i^\dagger |0\rangle \tag{5.4}$$

which is made the non-trivial vacuum via "normal-ordering". Normal-ordering means that all operators that annihilate the reference state (5.4) are to the right of the creation operators.

To find the similarity transformation, one computes cluster amplitudes $t_{ij\ldots}^{ab\cdots}$ by demanding that the respective p-h excitations are decoupled from the reference state so that the A-body product state becomes eigenstate of the similarity transformed hamiltonian $\bar{H}$ (The singles and doubles approximation we used previously basically means that we truncate the expansion $\hat{T}$ to $\hat{T}_1 + \hat{T}_2$ i.e., $\langle \Phi_i^a | \bar{H} | \Phi_0 \rangle = 0$ and $\langle \Phi_{ij}^{ab} | \bar{H} | \Phi_0 \rangle = 0$).

Similarly, in IM-SRG one performs a unitary transformation (so unlike coupled cluster $\bar{H}$ is hermitian in IM-SRG) by using generators that continuously drive the coupling between ground state and higher p-h excitations to zero. Empirically, the decoupling at $2p$-$2h$ level yields 90% of the correlation energy and $3p$-$3h$ increases that percentage to 99% irrespective of the number of particles or the potential governing the dynamics in the physical system at hand (as long as the first excitation state of the A-body nucleus is well separated from the A-body product state).

We study nucleon-nucleus systems as a nucleon attached to the A-body nucleus. The A-body product state is considered to be an exact ground state i.e., it is decoupled from all excitations up to and including Ap-Ah excitations. We view the corresponding similarity-transformed Hamiltonian $\bar{H}$ to be a renormalization group transformation that renormalizes the underlying NN EFT potential to account for the effects of many-body correlations on the low-energy observables. Thus, our key assumption is that the net effect of the similarity transformation in the many-body methods is a reference-state-dependent renormalization of the LECs in the starting NN EFT potential which only changes the short-distance physics. In what follows, I discuss our initial ideas and some of our preliminary results.

5.3 Ingredients of nucleon-nucleus effective field theory

As the reference state is the exact ground state for A-body nucleus, we partition the Hilbert space of orthonormalized single-particle states $\psi_p(\vec{r})$ with $p = 1 \ldots \Omega$ into the nucleus and valence nucleon orbitals, where the valence nucleon can only occupy Hilbert space with $p = A+1, A+2, \ldots \Omega$. Thus, the normal-ordered Hamiltonian H_N for elastic scattering of

an incoming nucleon N from the A-body nucleus is

$$H_N = \sum_{ab} f_b^a a_a^\dagger a_b \tag{5.5}$$

where, subscript $a, b, \ldots$ denote the valence states. The matrix elements f_b^a are dependent on the underlying NN EFT potential via

$$\sum_i \langle ia|V_{NN}|ib\rangle \tag{5.6}$$

Similarly, a NNN contact contributes via $\sum_{ij}\langle ija|V_{NNN}|ijb\rangle$ to include effects from the non-trivial vacuum. It is important to note that we do not include the most general Hamiltonian. For instance, the term $\frac{1}{4}\sum_{abci} v_{ci}^{ab} a_a^\dagger a_b^\dagger a_i a_c$, which includes contributions from $2p$-$1h$ excitations of the core, is not included.

We begin with a doubly-magic core to keep the problem simple. For doubly-magic nuclei with mass number A, the total orbital angular momentum $L_A = 0$ and, all the nucleons with spin-up are paired to the spin-down nucleons which results into total spin $S_A = 0$. Thus, when we sum over all i in Eq. (5.6) for one-pion exchange NN potential acting between valence and core nucleons,

$$V(\vec{q}) \propto \vec{\tau_i} \cdot \vec{\tau_a} \frac{(\vec{q}\cdot\vec{\sigma}_i)(\vec{q}\cdot\vec{\sigma}_a)}{m_\pi^2 + q^2}, \tag{5.7}$$

the net contribution reduces to zero. In addition, we restrict ourselves to elastic scattering of neutrons to avoid inclusion of the Coulomb potential.

Let us look at the NN contact interaction

$$V_{\text{cont}} = C_s \delta^{(3)}(\vec{r}_a - \vec{r_i}). \tag{5.8}$$

The resultant contribution is

$$\begin{aligned}\sum_i \langle ia|V_{NN}|ib\rangle &= \sum_i \int d^3r_i d^3r_a \psi_i^*(\vec{r}_i)\psi_a^*(\vec{r}_a)\delta^{(3)}(\vec{r}_a - \vec{r_i})\psi_i(\vec{r}_i)\psi_b(\vec{r}_b) \\ &= c_s \int d^3r \psi_a^*(\vec{r})\rho(\vec{r})\psi_b(\vec{r})\end{aligned} \tag{5.9}$$

where, $\rho = \sum_i \psi_i^*(\vec{r})\psi_i(\vec{r})$ is the density of the core and c_s is the renormalized LEC for nucleon-nucleus potential. Similarly, the contribution from NNN contact ($V_{NNN} = \mathrm{C}_E\delta^{(3)}(\vec{r}_a - \vec{r}_i)\delta^{(3)}(\vec{r}_a - \vec{r}_j)$) is

$$\sum_{ij}\langle ija|V_{NNN}|ijb\rangle = c_e \int d^3r\psi_a^*(\vec{r})\rho^2\psi_b^*(\vec{r}), \tag{5.10}$$

and from the NN spin-orbit potential $C_{ls}(\vec{\sigma}_i + \vec{\sigma}_a)\cdot(\vec{\nabla}_i \times \vec{\nabla}_a)\delta^{(3)}(\vec{r}_i - \vec{r}_a)$ it is

$$\frac{c_{ls}}{r}\frac{\partial\rho(\vec{r})}{\partial r}\vec{l}\cdot\vec{\sigma} \tag{5.11}$$

where $\vec{l}$ is the orbital angular momentum of the incoming nucleon and $\vec{\sigma}$ is its spin. c_s, c_{ls} and, c_e are the LECs in nucleon-nucleus potential, that need to to be optimized to elastic scattering nucleon-nucleus data. There are also contributions from other terms in the short-range NN potential. However, to get started I only did two-parameter optimization using NN contact and the spin-orbit term.

The radius of the core R defines the physical range of the nucleon-nucleus potential and is an important constraint to make elastic scattering calculations that are comparable to experiments. Therefore, we construct the A-body product state in the harmonic oscillator basis with the oscillator frequency of the basis adjusted to the point-proton radius of the core.

5.4 Lippmann-Schwinger equation and differential cross section

In this section, we briefly discuss the method used to compute the differential cross section $\frac{d\sigma}{d\Omega}$ [56]. We begin with the Schrödinger equation in operator form,

$$(E - H_0)|\psi\rangle = V|\psi\rangle.$$

Here, H_0 is the kinetic energy i.e., the unperturbed Hamiltonian in relative momentum $\vec{p}_0$ for the particle of reduced mass $\mu = Am/(A+1)$ with m being the nucleon mass. Multiplying

both sides with $(E - H_0)^{-1}$ we get,

$$|\psi\rangle = (E - H_0)^{-1} V |\psi\rangle.$$

We add $+i\epsilon$ to go around the pole of $1/(E - H_0)$ by including outgoing scattered-bound wave condition through the imaginary part $i\epsilon$:

$$|\psi_{\vec{p}}^{(+)}\rangle = (E - H_0 + i\epsilon)^{-1} V |\psi_{\vec{p}}^{(+)}\rangle.$$

In addition, incoming plane waves $|\phi_{\vec{p}}\rangle$ fulfill $(E - H_0)|\phi_{\vec{p}}\rangle = 0$. Thus, the full scattered solution is,

$$\begin{aligned} |\psi_{\vec{p}}^{(+)}\rangle &= |\psi_{\vec{p}}\rangle + (E - H_0 + i\epsilon)^{-1} V |\psi_{\vec{p}}^{(+)}\rangle \\ |\psi_{\vec{p}}^{(+)}\rangle &= |\phi_{\vec{p}}\rangle + G_E^{(+)} V |\psi_{\vec{p}}^{(+)}\rangle \end{aligned} \tag{5.12}$$

where $G_E^{(+)} = (E - H_0 + i\epsilon)^{-1}$ is the abstract Green's operator for the outgoing waves. This is the Lippmann-Schwinger (LS) equation for two-body scattering.

Next, we define the T-matrix element as

$$T_E(\vec{p}', \vec{p}) = \langle \psi_{\vec{p}'} | V | \phi_{\vec{p}} \rangle. \tag{5.13}$$

Consequently, Eq. (5.12) can be re-written as

$$T_E(\vec{p}', \vec{p}) = V(\vec{p}', \vec{p}) + \int d^3k V(\vec{p}', \vec{k}) G_E^{(+)}(k) T_E(\vec{k}.\vec{p}) \tag{5.14}$$

In the abstract form this is $T_E = V + V G_E^{(+)} T_E$ which gives the Born Series,

$$T = V + VGV + VGVGV + \ldots. \tag{5.15}$$

The partial-wave expansions of V and T are,

$$V(\vec{p}',\vec{p}) = \frac{2}{\pi}\sum_{l=0}^{\infty}\sum_{m=-l}^{l} V_l(p',p)Y^*_{lm}(\Omega_{\vec{p}'})Y_{lm}(\Omega_{\vec{p}}), \tag{5.16}$$

$$T(\vec{p}',\vec{p}) = \frac{2}{\pi}\sum_{l=0}^{\infty}\sum_{m=-l}^{l} T_l(p',p;E)Y^*_{lm}(\Omega_{\vec{p}'})Y_{lm}(\Omega_{\vec{p}}). \tag{5.17}$$

Here, $Y_{lm}(\Omega)$ are spherical harmonics and momentum eigenstates have the normalization,

$$|\vec{p}\rangle = \sqrt{\frac{2}{\pi}}\sum_{l,m} Y^*_{l,m}(\Omega_{\vec{p}})|p,l,m\rangle$$

with

$$\delta(\vec{k}'-\vec{k}) = \frac{\delta(p'-p)}{pp'}\sum_{l,m} Y^*_{lm}(\Omega_{\vec{p}'})Y_{lm}(\Omega_{\vec{p}}),$$

and

$$\langle p'l'm'|plm\rangle = \frac{\pi}{2}\frac{\delta(p'-p)}{pp'}\delta_{ll'}\delta_{mm'}.$$

We are interested in finding one-dimensional LS equation in the radial coordinate. Therefore, we substitute the partial-wave decomposition of T and V matrices to Eq. (5.14) to get,

$$T_l(p',p;E) = V_l(p',p) + \frac{2}{\pi}\int_0^{\infty}\frac{dkk^2V_l(p',k)T_l(k,p;E)}{E-E_k+i\epsilon}, \tag{5.18}$$

using the orthogonality conditions

$$\int_{-1}^{1} dxP_{l'}(x)P_l(x) = \frac{2}{2l+1}\delta_{l'l},$$

$$\int d\Omega Y^*_{lm}(\Omega)Y_{l'm'}(\Omega) = \delta_{ll'}\delta_{mm'}.$$

Thus, we need to solve Eq. (5.18) numerically for a given scattering potential $V_l(p',p)$ in each partial wave l. The details of the numerical solution to LS equation are in Appendix C.

To find the full elastic scattering amplitude,

$$f_E(\theta) = \sum_{l=0}^{l_{\max}} (2l+1) P_l(\cos\theta) \frac{e^{i\delta_l} \sin\delta_l}{p_0} \tag{5.19}$$

we use the relation

$$T_l(p_0, p_0; E_{p_0}) = -\frac{e^{i\delta_l} \sin\delta_l}{2\mu p_0}. \tag{5.20}$$

Here, θ is the angle between incident and outgoing direction in center-of-mass frame and $p_0 = \sqrt{2mE_{\rm lab}}\frac{A}{A+1}$. The scattering amplitude yields the differential cross section,

$$\frac{d\sigma}{d\Omega}(\theta, \phi) = |f_E(\theta)|^2. \tag{5.21}$$

For an incident spin-1/2 neutron interacting with the doubly-magic core with total angular momentum $L_A = 0$ and total spin $S_A = 0$, the $L \cdot S$ coupling can flip the spin-projection $s_z = \pm 1/2$ of the incident neutron. Thus, we need to find scattering amplitude which accounts for all four combinations $\{(+,-),(+,+),(-,-),(-,+)\}$ of incoming and outgoing spins of the neutrons, when spin-orbit coupling is included. The total spin j of the $A+1$ system can take two values, $j = l \pm 1/2$, where l is the partial-wave for the incident neutron. We denote phase shift by $\delta_l^{(+)}$ in $j = l+1/2$ channel and $\delta_l^{(-)}$ in $j = l-1/2$ channel. The scattering amplitude for the spin-up beam scattering into spin-down waves is

$$f_{++}(\theta) = \sum_{l=0}^{\infty} \frac{1}{k} \left[(l+1) e^{i\delta_l^+} \sin\delta_l^+ + l e^{i\delta_l^-} \sin\delta_l^- \right] P_l(\cos\theta) \tag{5.22}$$

and the scattering amplitude from spin-up to spin-down is,

$$f_{+-}(\theta, \phi) = \sum_{l=1}^{\infty} \frac{1}{k} \left[e^{i\delta_l^+} \sin\delta_l^+ - e^{i\delta_l^-} \sin\delta_l^- \right] P_l^1(\cos\theta) e^{i\phi}. \tag{5.23}$$

For an incident spin down beam, the down-to-down amplitude equals the up-to-up one i.e, $f_{--}(\theta) = f_{++}(\theta)$ and, spin flips $f_{+-}(\theta, \phi)$ and $f_{-+}(\theta, \phi)$ only differ by phase factor $e^{-i\phi}$.

Thus, for unpolarized beams (of spin $s = 1/2$ neutrons) the differential cross section is

$$\begin{aligned} \frac{d\sigma}{d\Omega} &= \frac{1}{2s+1}\Big(2|f_{++}(\theta)|^2 + 2|f_{+-}(\theta,\phi)|^2\Big) \\ &= |f_{++}(\theta)|^2 + |f_{+-}(\theta,\phi)|^2. \end{aligned} \tag{5.24}$$

We refer the reader to any standard undergraduate textbook for detailed derivation for scattering amplitudes in the presence of spin-orbit coupling. We follow Ref. [56]. The numerical implementation remains the same, except we solve two on-shell T-matrix elements; one for each of the two total angular momentum ($j = l \pm 1/2$) channels.

Once the parameters in nucleon-nucleus interaction is optimized to data, we used the potential to compute bound states in the harmonic oscillator basis. The interaction matrix elements in the finite harmonic oscillator basis are given by,

$$\langle n', l|V_l|n, l\rangle = \int_0^\infty r^2 \psi_{n,l}(r) V_l(r) \psi_{n',l}(r) \tag{5.25}$$

We gradually increase the harmonic oscillator basis size to obtain converged energy eigenvalues in each partial wave.

In the calculations for bound state and differential cross section, the nucleon-nucleus potential V_l includes a strongly repulsive potential $V_l^{\rm occ} = \sum_{n=core} |n, l\rangle\langle n, l|$ to exclude the harmonic oscillator states occupied by the nucleons in the core in partial wave l. This makes it energetically unfavorable for the incoming nucleon to occupy states that are already occupied by nucleons in the core and thus, accounts for Pauli-exclusion principle.

5.5 Preliminary Results

First we adjusted only the interaction strength of the density term (5.9) to the differential cross section at various incident neutron energies between 4 to 95 MeV. The χ^2-fit was obtained using data points at low-momentum transfer in each case because low-momentum transfers correspond to small angular deviations and thus is more likely to be a result of a less complex neutron-nucleus interaction. Table 5.1 shows the values of LEC c_s obtained by

Table 5.1: The optimized values of coupling coefficient c_s (in fm^2) obtained by fitting theoretical differential cross section for elastic scattering (computed with only the density term in the nucleon-nucleus potential) to experimental data for $^{16}O(n,n)^{16}O$ scattering process, at various incident laboratory energies $E_{\rm lab}$ (in MeV).

$E_{\rm lab}$	c_s
95.0	−1.18
65.0	−0.92
28.0	−1.38
20.0	−1.19
18.0	−1.24
14.0	−1.07
11.6	−1.18
4.0	−2.26

performing a fit to the experimental differential cross section at various energies $E_{\rm lab}$ of the incident neutron beam. The central potential in all cases is not bound enough to yield bound $s_{1/2}, d_{5/2}$ or $d_{3/2}$ states. It is only at $E_{\rm lab} = 4$ MeV, we find $s_{1/2}$ at energy −7.34 MeV, and $d_{3/2}, d_{5/2}$ orbitals at −5.71 MeV. Figure 5.1 compares the theoretical differential cross section (denoted by red triangles) to experimental data in Ref. [45] at 4 MeV. The experimental data on differential cross section at other energies are taken from Refs. [10, 63, 44].

For the reproduction of observed spin-parity of nuclear states, the spin-orbit interaction (5.11) is necessary. So, we perform a two-parameter optimization to the elastic differential cross section at various incident neutron energies. The resultant c_s and c_{ls} values are tabulated in Table 5.2 along side the bound state energies in $d_{5/2}$ and $s_{1/2}$ channels using the optimized nucleon-nucleus potential. It is clear that the central potential term does not have enough strength to give a bound $s_{1/2}$ state with respect to ^{16}O core. The inclusion of a strong spin-orbit coupling makes the $d_{5/2}$ orbital bound at all incident energies we considered, with binding energies ranging between −33 MeV and −4.6 MeV; out of which the result at $E_{\rm lab} = 14$ MeV is closest to the experimental ^{17}O bound state energy with respect to ^{16}O + n threshold.

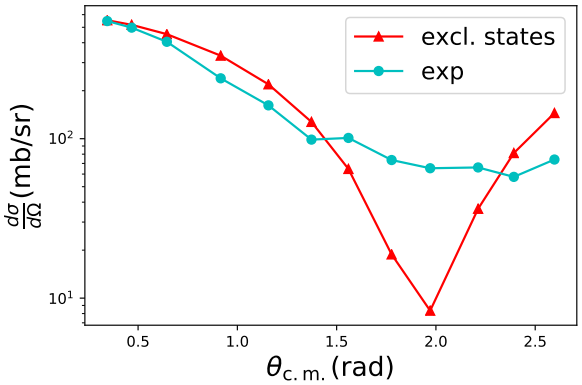

Figure 5.1: The theoretical differential cross section computed using nucleon-nucleus potential $V(r) = c_s\rho(r)$ (marked by red triangles) in comparison to experimental data [45](shown by blue dots) at incident neutron energy $E_{\text{lab}} = 4$ MeV.

In Figure 5.2 we compare the theoretical differential cross section (red triangles), calculated using interaction with the density and spin-orbit coupling terms, to the experimental data from Ref. [10] (marked by blue dots) at $E_{\text{lab}} = 14$ MeV.

5.5.1 Discussion

There are two separate factors at play. One factor is the truncation in complexity of the effective nucleon-nucleus potential. For instance, we did not include $2p$-$1h$ core excitation contributions from the term $\frac{1}{4}\sum_{abci} v_{ci}^{ab} a_a^\dagger a_b^\dagger a_i a_c$. These matrix elements v_{ci}^{ab} can result into off-shell processes which excite nucleon in state i to valence states and scatter it back to the core to yield elastic scattering of the incoming nucleon.

Another factor is the momentum of incident particle which dictates how important the contribution from core excitations will be. A fast incoming particle will be less sensitive to such contributions and clearly just a two-parameter nucleon-nucleus interaction at these energies is too simple to give meaningful calculations for bound states in $A+1$ system. We need to include other effective potential terms at $0p$-$0h$ level to see if the optimization to differential cross section at high incident energies (higher than the neutron separation energy of the core nucleus or its first excitation energy) yield systematically improvable results for low-lying excitations of the $A+1$ system. On the other hand, at very low incident energies

the contributions from np-nh excitations of the core will become non-perturbative which would correspond to scattering via compound-nucleus formation.

To conclude, at this point we have not been able to connect these two layers of the problem to translate it to a nucleon-nucleus interaction with a power counting.

Table 5.2: The optimized values of coupling coefficients c_s (in fm^2) and c_{ls} (both in fm^2) obtained by fitting theoretical differential cross section for elastic scattering (computed with the density and spin-orbit coupling term in the nucleon-nucleus potential) to experimental data for $^{16}\mathrm{O}(n,n)^{16}\mathrm{O}$ scattering process at various incident laboratory energies E_{lab} (in MeV). The corresponding energies (in MeV) of $d_{5/2}$ and $s_{1/2}$ bound states, which corresponds to ^{17}O ground state and its first excitation energy, respectively, are also shown. The dashes denote unbound orbitals with respect to the ground state of ^{16}O core.

E_{lab}	c_s	c_{ls}	$E(d_{5/2})$	$E(s_{1/2})$
95.0	-2.38	7.79	-33.33	-9.54
65.0	-2.53	4.5	-25.3	-12.38
28.0	-1.41	6.15	-8.34	-
20.0	-0.94	8.4	-7.15	-
18.0	-0.95	8.55	-7.75	-
14.0	-1.61	3.71	-4.55	-
11.6	-1.6	4.3	-6.26	-
4.0	-2.22	1.41	-8.79	-6.72

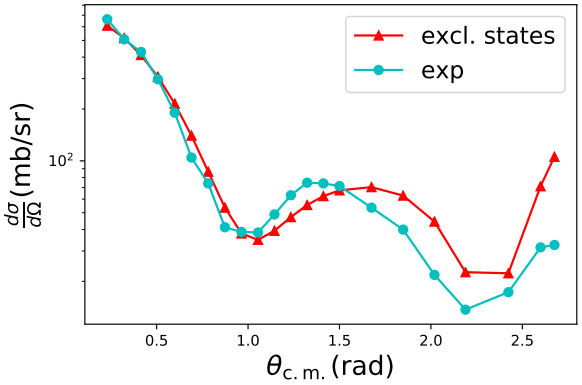

Figure 5.2: The theoretical differential cross section computed using nucleon-nucleus potential $V(r) = c_s\rho(r) + \frac{c_{ls}}{r}\frac{\partial\rho}{\partial r}$ (marked by red triangles) in comparison to experimental data [10] (shown as blue dots) at incident neutron energy $E_{\mathrm{lab}} = 14$ MeV.

Chapter 6

Summary

We performed the first calculations of ^{16}O and ^{40}Ca nuclei with NLO pionless EFT potential. At NLO we find these nuclei to be bound at the physical pion mass and heavier pion mass of ($m_\pi = 806$ MeV). We report that our results for physical ^{16}O and ^{40}Ca nuclei are comparable to the NLO chiral EFT results for these nuclei in Ref. [16]. At the heavier pion mass, we make predictions for the binding energy of ^{16}O and ^{40}Ca nuclei using lattice QCD data for $A = 2, 3$ nuclei as input to optimize the NLO pionless EFT potentials. However we are limited to the cutoff range of 330 to 650 MeV at the physical pion mass and to the range of 600 to 850 MeV at the heavier pion mass, for studying cutoff variation of our binding energy results for these nuclei. For these ranges we find the binding energy of the atomic ^{16}O and ^{40}Ca nuclei vary by roughly 10%, and for the lattice case the variation is roughly 25%. We remind the reader that there is no four-body force at NLO in our calculations; it has recently been shown that a four-body contact force enters at NLO in study of up to six-bosons using short-range interactions [9].

The pionless EFT potentials were regulated directly by the finite harmonic oscillator basis used in many-body methods. To accomplish this we combined the DVR projection of the two- and three-nucleon unregulated momentum space potentials with our technique of infrared improvement. The advantage of this approach lies in ultraviolet convergence of computed observables by construction. In addition, one needs to compute oscillator EFT matrix elements only for one cutoff and nucleon mass due to scaling relations in Eq. (2.53).

These scaling relations also provided a simple explanation of the Tjon correlations between the binding energies of $A = 3$ and $A = 4$ nuclei using LO NN contact potentials.

We showed that the parameter k_∞ in the infrared extrapolations of many-body binding energy is the separation momentum $k_{\rm sep}$ for the lowest-energy break-up channel of that nucleus. The in-built ultraviolet convergence of oscillator EFT potentials yielded k_∞ parameter very close to the corresponding $k_{\rm sep}$ for $A = 3, 4$ nuclei.

In chapter 5, we switched to the study of nucleon-nucleus systems. Our goal is to establish a power counting and build a nucleon-nucleus EFT potential that can simultaneously explain the low-lying excitations of $A+1$ system and the differential cross section data for $A(n,n)A$ scattering process. Inspired by the idea of many-body methods like coupled cluster and IM-SRG, we started by assuming the A-body product state as an exact ground state of the core. The elastic scattering potential, which is referenced to the A-body product state, is active only in the valence space available to the incoming nucleons. Under the assumption that the similarity transformation in the many-body methods renormalize the LECs of the underlying NN EFT, the NN potentials become regulated by the density of the core with new unknown LECs in the effective nucleon-nucleus potential. To begin with, we only considered the central term (which comes from NN contact) and the spin-orbit term (from NN spin-orbit coupling) to study the elastic neutron scattering of ^{16}O nucleus. The optimization was done at various incident neutron energies. For each incident energy, we computed the $d_{5/2}$, $s_{1/2}$ and $d_{3/2}$ orbital energies using the optimized nucleon-nucleus potential. In our simple analysis we found that our central term by itself is not attractive enough to make these orbitals bound with respect to the core. The inclusion of spin-orbit coupling makes the $d_{5/2}$ state bound, but the binding energy varies depending upon the incident energy at which differential cross section was used to optimize the nucleon-nucleus potential. Our current analysis is too simple to identify power counting for effective nucleon-nucleus potentials that are governed by an interplay between the momentum of incoming neutrons, and the complexity of the interaction between the valence- and core-nucleons.

Bibliography

[1] Aoki, S., Doi, T., Hatsuda, T., Ikeda, Y., Inoue, T., Ishii, N., Murano, K., Nemura, H., and Sasaki, K. (2012). Lattice quantum chromodynamical approach to nuclear physics. *Progress of Theoretical and Experimental Physics*, 2012(1):01A105. 3

[2] Aoki, S., Hatsuda, T., and Ishii, N. (2010). Theoretical foundation of the nuclear force in qcd and its applications to central and tensor forces in quenched lattice qcd simulations. *Progress of Theoretical Physics*, 123(1):89–128. 3

[3] Bansal, A., Binder, S., Ekström, A., Hagen, G., Jansen, G. R., and Papenbrock, T. (2018). Pion-less effective field theory for atomic nuclei and lattice nuclei. *Phys. Rev. C*, 98:054301. 14

[4] Barnea, N. (1997). Exact solution of the schrödinger and faddeev equations for few body systems. 31

[5] Barnea, N., Contessi, L., Gazit, D., Pederiva, F., and van Kolck, U. (2015). Effective field theory for lattice nuclei. *Phys. Rev. Lett.*, 114:052501. 4

[6] Bartlett, R. J. and Musiał, M. (2007). Coupled-cluster theory in quantum chemistry. *Rev. Mod. Phys.*, 79:291–352. 64

[7] Baye, D. and Heenen, P.-H. (1986). Generalised meshes for quantum mechanical problems. *J. Physics A: Math. Gen.*, 19(11):2041. 19

[8] Bazak, B., Eliyahu, M., and van Kolck, U. (2016). Effective Field Theory for Few-Boson Systems. *Phys. Rev.*, A94(5):052502. 56, 63

[9] Bazak, B., Kirscher, J., König, S., Valderrama, M. P., Barnea, N., and van Kolck, U. (2019). Four-body scale in universal few-boson systems. *Phys. Rev. Lett.*, 122:143001. 11, 86

[10] Beach, P. L., Finlay, R. W., Cassola, R. L., and Koshel, R. D. (1967). Elastic scattering of neutrons from o and ar at 14.0 mev. *Phys. Rev.*, 156:1201–1206. xiv, 82, 83, 85

[11] Beane, S. R., Chang, E., Cohen, S. D., Detmold, W., Junnarkar, P., Lin, H. W., Luu, T. C., Orginos, K., Parreño, A., Savage, M. J., and Walker-Loud, A. (2013a).

Nucleon-nucleon scattering parameters in the limit of su(3) flavor symmetry. *Phys. Rev. C*, 88:024003. xiii, 10, 39, 44, 47, 70

[12] Beane, S. R., Chang, E., Cohen, S. D., Detmold, W., Lin, H. W., Luu, T. C., Orginos, K., Parreño, A., Savage, M. J., and Walker-Loud, A. (2013b). Light nuclei and hypernuclei from quantum chromodynamics in the limit of su(3) flavor symmetry. *Phys. Rev. D*, 87:034506. 2, 3, 39, 51

[13] Beane, S. R., Chang, E., Detmold, W., Lin, H. W., Luu, T. C., Orginos, K., Parreño, A., Savage, M. J., Torok, A., and Walker-Loud, A. (2012). Deuteron and exotic two-body bound states from lattice qcd. *Phys. Rev. D*, 85:054511. 2

[14] Bedaque, P. F., Hammer, H. W., and van Kolck, U. (1999). Renormalization of the three-body system with short range interactions. *Phys. Rev. Lett.*, 82:463–467. 10, 50, 55

[15] Bertsch, G., Dean, D., and Nazarewicz, W. (2007). Universal Nuclear Energy Density Functional: Computing Atomic Nuclei. *SciDAC Review 6*, page 42. x, 3, 5

[16] Binder, S., Ekström, A., Hagen, G., Papenbrock, T., and Wendt, K. A. (2016). Effective field theory in the harmonic oscillator basis. *Phys. Rev. C*, 93:044332. 13, 18, 19, 39, 42, 46, 67, 71, 72, 86, 104

[17] Bogner, S. K., Furnstahl, R. J., Maris, P., Perry, R. J., Schwenk, A., and Vary, J. P. (2008). Convergence in the no-core shell model with low-momentum two-nucleon interactions. *Nucl. Phys.*, A801:21–42. 62

[18] Borsanyi, S. et al. (2015). Ab initio calculation of the neutron-proton mass difference. *Science*, 347:1452–1455. 1

[19] Chang, E., Detmold, W., Orginos, K., Parreño, A., Savage, M. J., Tiburzi, B. C., and Beane, S. R. (2015). Magnetic structure of light nuclei from lattice qcd. *Phys. Rev. D*, 92:114502. 2

[20] Contessi, L., Lovato, A., Pederiva, F., Roggero, A., Kirscher, J., and van Kolck, U. (2017). Ground-state properties of ^{4}He and ^{16}O extrapolated from lattice QCD with pionless EFT. *Physics Letters B*, 772(Supplement C):839 – 848. 4, 12, 13, 52, 65

[21] Coon, S. A., Avetian, M. I., Kruse, M. K. G., van Kolck, U., Maris, P., and Vary, J. P. (2012). Convergence properties of *ab initio* calculations of light nuclei in a harmonic oscillator basis. *Phys. Rev. C*, 86:054002. 16

[22] Dickinson, A. S. and Certain, P. R. (1968). Calculation of matrix elements for one-dimensional quantum-mechanical problems. *J. Chem. Phys.*, 49:4209–4211. 19

[23] Dumbrajs, O., Koch, R., Pilkuhn, H., Oades, G., Behrens, H., de Swart, J., and Kroll, P. (1983). Compilation of coupling constants and low-energy parameters. *Nuclear Physics B*, 216(2):277 – 335. 39

[24] Dürr, S., Fodor, Z., Frison, J., Hoelbling, C., Hoffmann, R., Katz, S. D., Krieg, S., Kurth, T., Lellouch, L., Lippert, T., Szabo, K. K., and Vulvert, G. (2008). Ab initio determination of light hadron masses. *Science*, 322(5905):1224–1227. x, 1, 2

[25] Efimov, V. N. (1971). WEAKLY-BOUND STATES OF 3 RESONANTLY-INTERACTING PARTICLES. *Sov. J. Nucl. Phys.*, 12:589. 11

[26] Epelbaum, E., Krebs, H., and Meißner, U.-G. (2015). Precision nucleon-nucleon potential at fifth order in the chiral expansion. *Phys. Rev. Lett.*, 115:122301. 43

[27] Epelbaum, E., Nogga, A., Glöckle, W., Kamada, H., Meißner, U.-G., and Witała, H. (2002). Three-nucleon forces from chiral effective field theory. *Phys. Rev. C*, 66:064001. 10, 31

[28] Erkelenz, K., Alzetta, R., and Holinde, K. (1971). Momentum space calculations and helicity formalism in nuclear physics. *Nuclear Physics A*, 176:413–432. 8

[29] Forssén, C., Carlsson, B. D., Johansson, H. T., Sääf, D., Bansal, A., Hagen, G., and Papenbrock, T. (2017). Large-scale exact diagonalizations reveal low-momentum scales of nuclei. *ArXiv e-prints*. 14, 58

[30] Furnstahl, R. J., Hagen, G., and Papenbrock, T. (2012). Corrections to nuclear energies and radii in finite oscillator spaces. *Phys. Rev. C*, 86:031301. 56, 57

[31] Furnstahl, R. J., Hagen, G., Papenbrock, T., and Wendt, K. A. (2015). Infrared extrapolations for atomic nuclei. *J. Phys. G*, 42(3):034032. 16

[32] Furnstahl, R. J., Hagen, G., Papenbrock, T., and Wendt, K. A. (2015). Infrared extrapolations for atomic nuclei. *Journal of Physics G: Nuclear and Particle Physics*, 42(3):034032. 57

[33] Furnstahl, R. J., Klco, N., Phillips, D. R., and Wesolowski, S. (2015). Quantifying truncation errors in effective field theory. *ArXiv e-prints*. 40

[34] Furnstahl, R. J., Papenbrock, T., and More, S. N. (2014). Systematic expansion for infrared oscillator basis extrapolations. *Phys. Rev.*, C89(4):044301. 16, 57

[35] Gradshteyn, I. S. and Ryzhik, I. M. (2007). *Table of integrals, series, and products*. Elsevier/Academic Press, Amsterdam, seventh edition. Translated from the Russian, Translation edited and with a preface by Alan Jeffrey and Daniel Zwillinger, With one CD-ROM (Windows, Macintosh and UNIX). 104, 105, 106

[36] Hagen, G., Papenbrock, T., Dean, D. J., Schwenk, A., Nogga, A., Włoch, M., and Piecuch, P. (2007). Coupled-cluster theory for three-body Hamiltonians. *Phys. Rev. C*, 76:034302. 65

[37] Hagen, G., Papenbrock, T., Hjorth-Jensen, M., and Dean, D. J. (2014). Coupled-cluster computations of atomic nuclei. *Rep. Prog. Phys.*, 77(9):096302. 64, 74

[38] Harris, D. O., Engerholm, G. G., and Gwinn, W. D. (1965). Calculation of matrix elements for one-dimensional quantum-mechanical problems and the application to anharmonic oscillators. *J. Chem. Phys.*, 43:1515–1517. 19

[39] Heller, E. J. and Yamani, H. A. (1974). New L^2 approach to quantum scattering: Theory. *Phys. Rev. A*, 9:1201–1208. 38

[40] Hergert, H., Bogner, S. K., Morris, T. D., Schwenk, A., and Tsukiyama, K. (2015). The In-Medium Similarity Renormalization Group: A Novel Ab Initio Method for Nuclei. *ArXiv e-prints*. 74

[41] Inoue, T., Aoki, S., Charron, B., Doi, T., Hatsuda, T., Ikeda, Y., Ishii, N., Murano, K., Nemura, H., and Sasaki, K. (2015). Medium-heavy nuclei from nucleon-nucleon interactions in lattice qcd. *Phys. Rev. C*, 91:011001. 3, 4

[42] Inoue, T., Aoki, S., Doi, T., Hatsuda, T., Ikeda, Y., Ishii, N., Murano, K., Nemura, H., and Sasaki, K. (2012). Two-Baryon Potentials and H-Dibaryon from 3-flavor Lattice QCD Simulations. *Nucl. Phys.*, A881:28–43. 3

[43] Ishii, N., Aoki, S., and Hatsuda, T. (2007). Nuclear force from lattice qcd. *Phys. Rev. Lett.*, 99:022001. 3

[44] Islam, M., Finlay, R., and Petler, J. (1987). Elastic and inelastic scattering of nucleons from 16o. *Nuclear Physics A*, 464(3):395 – 414. 82

[45] Johnson, C. H. and Fowler, J. L. (1967). Scattering of neutrons from ^{16}O in the 2.2- to 4.2-mev energy range. *Phys. Rev.*, 162:890–899. xiv, 82, 83

[46] Kaplan, D. B., Savage, M. J., and Wise, M. B. (1998). A new expansion for nucleon-nucleon interactions. *Physics Letters B*, 424(34):390 – 396. 9

[47] Kirscher, J. (2015). *Pionless Effective Field Theory in Few-Nucleon Systems*. PhD thesis, George Washington University. 12

[48] Kirscher, J., Barnea, N., Gazit, D., Pederiva, F., and van Kolck, U. (2015). Spectra and scattering of light lattice nuclei from effective field theory. *Phys. Rev. C*, 92:054002. 56

[49] Kirscher, J., Grießhammer, H. W., Shukla, D., and Hofmann, H. M. (2009). Universal correlations in pion-less EFT with the resonating group model: three and four nucleons. In *6th International Workshop on Chiral Dynamics*, page 105. 50

[50] Kirscher, J., Grießhammer, H. W., Shukla, D., and Hofmann, H. M. (2010). Universal correlations in pion-less eft with the resonating group method: Three and four nucleons. *The European Physical Journal A*, 44(2):239–256. 13

[51] Kong, X. and Ravndal, F. (2000). Coulomb effects in low energy proton-proton scattering. *Nuclear Physics A*, 665(1):137 – 163. 11

[52] König, S., Bogner, S. K., Furnstahl, R. J., More, S. N., and Papenbrock, T. (2014). Ultraviolet extrapolations in finite oscillator bases. *Phys. Rev. C*, 90:064007. 16, 56

[53] König, S. and Lee, D. (2017). Volume Dependence of N-Body Bound States. *ArXiv e-prints*. 57

[54] Kowalski, K., Dean, D. J., Hjorth-Jensen, M., Papenbrock, T., and Piecuch, P. (2004). Coupled cluster calculations of ground and excited states of nuclei. *Phys. Rev. Lett.*, 92:132501. 74

[55] Kümmel, H., Lührmann, K. H., and Zabolitzky, J. G. (1978). Many-fermion theory in expS- (or coupled cluster) form. *Physics Reports*, 36(1):1 – 63. 64

[56] Landau, R. (1990). *Quantum mechanics II: a second course in quantum theory*. Number v. 2 in Wiley-Interscience publication. J. Wiley. 77, 81, 110

[57] Lensky, V., Birse, M. C., and Walet, N. R. (2016). Description of light nuclei in pionless effective field theory using the stochastic variational method. *Phys. Rev. C*, 94:034003. 12, 13

[58] Light, J. C. and Carrington, T. (2007). *Discrete-Variable Representations and their Utilization*, pages 263–310. John Wiley & Sons, Inc. 19

[59] Light, J. C., Hamilton, I. P., and Lill, J. V. (1985). Generalized discrete variable approximation in quantum mechanics. *J. Chem. Phys.*, 82:1400–1409. 19

[60] Littlejohn, R. G., Cargo, M., Carrington, T., Mitchell, K. A., and Poirier, B. (2002). A general framework for discrete variable representation basis sets. , 116:8691–8703. 19

[61] Lüscher, M. (1986). Volume Dependence of the Energy Spectrum in Massive Quantum Field Theories. 1. Stable Particle States. *Commun. Math. Phys.*, 104:177. 16

[62] Machleidt, R. (2001). High-precision, charge-dependent Bonn nucleon-nucleon potential. *Phys. Rev. C*, 63:024001. 40

[63] Mermod, P. et al. (2006). 95-MeV neutron scattering on hydrogen, deuterium, carbon, and oxygen. *Phys. Rev.*, C74:054002. 82

[64] Mohr, P. J., Taylor, B. N., and Newell, D. B. (2012). Codata recommended values of the fundamental physical constants: 2010. *Rev. Mod. Phys.*, 84:1527–1605. 39

[65] Montgomery, Jr, H. E., Campoy, G., and Aquino, N. (2008). Exact solutions for the D-dimensional spherical isotropic confined harmonic oscillator. *ArXiv e-prints*. 31

[66] More, S. N., Ekström, A., Furnstahl, R. J., Hagen, G., and Papenbrock, T. (2013). Universal properties of infrared oscillator basis extrapolations. *Phys. Rev. C*, 87:044326. 15, 16, 59

[67] Navratil, P. (2007). Local three-nucleon interaction from chiral effective field theory. *Few Body Syst.*, 41:117–140. 31

[68] Navrátil, P., Quaglioni, S., Stetcu, I., and Barrett, B. R. (2009). Recent developments in no-core shell-model calculations. *Journal of Physics G: Nuclear and Particle Physics*, 36(8):083101. 39

[69] Okubo, S. and Marshak, R. (1958). Velocity dependence of the two-nucleon interaction. *Annals of Physics*, 4(2):166 – 179. 7

[70] Olive, K. and Group, P. D. (2014). Review of particle physics. *Chinese Physics C*, 38(9):090001. 39

[71] Orginos, K., Parreño, A., Savage, M. J., Beane, S. R., Chang, E., and Detmold, W. (2015). Two nucleon systems at $m_\pi \sim 450$ MeV from lattice qcd. *Phys. Rev. D*, 92:114512. 2

[72] Phillips, D. R. and Cohen, T. D. (1997). How short is too short? Constraining contact interactions in nucleon-nucleon scattering. *Phys. Lett.*, B390:7–12. 45

[73] Platter, L., Hammer, H.-W., and Meiner, U.-G. (2005). On the correlation between the binding energies of the triton and the α-particle. *Physics Letters B*, 607(34):254 – 258. 11, 51, 55

[74] Roth, R., Binder, S., Vobig, K., Calci, A., Langhammer, J., and Navrátil, P. (2012). Medium-Mass Nuclei with Normal-Ordered Chiral NN+3N Interactions. *Physical Review Letters*, 109(5):052501. 66, 69

[75] Shirokov, A. M., Mazur, A. I., Zaytsev, S. A., Vary, J. P., and Weber, T. A. (2004). Nucleon-nucleon interaction in the j-matrix inverse scattering approach and few-nucleon systems. *Phys. Rev. C*, 70:044005. 38

[76] Stetcu, I., Barrett, B., and van Kolck, U. (2007). No-core shell model in an effective-field-theory framework. *Phys. Lett. B*, 653(24):358 – 362. 13, 56, 65

[77] Thomas, L. H. (1935). The interaction between a neutron and a proton and the structure of h^3. *Phys. Rev.*, 47:903–909. 53, 55

[78] Tjon, J. A. (1975). Bound states of 4he with local interactions. *Physics Letters B*, 56(3):217 – 220. 11, 53, 55

[79] Tsukiyama, K., Bogner, S. K., and Schwenk, A. (2011). In-medium similarity renormalization group for nuclei. *Phys. Rev. Lett.*, 106:222502. 74

[80] van Kolck, U. (1994). Few-nucleon forces from chiral Lagrangians. *Phys. Rev. C*, 49:2932–2941. 10

[81] Vanasse, J., Egolf, D. A., Kerin, J., König, S., and Springer, R. P. (2014). ^{3}He and pd scattering to next-to-leading order in pionless effective field theory. *Phys. Rev. C*, 89:064003. 11

[82] Wagman, M. L., Winter, F., Chang, E., Davoudi, Z., Detmold, W., Orginos, K., Savage, M. J., and Shanahan, P. E. (2017). Baryon-Baryon Interactions and Spin-Flavor Symmetry from Lattice Quantum Chromodynamics. *Phys. Rev.*, D96(11):114510. 3, 10

[83] Wapstra, A. and Audi, G. (1985). The 1983 atomic mass evaluation. *Nuclear Physics A*, 432(1):1 – 54. 39

[84] Wendt, K. A., Forssén, C., Papenbrock, T., and Sääf, D. (2015). Infrared length scale and extrapolations for the no-core shell model. *Phys. Rev. C*, 91:061301. 16, 57, 59

[85] Wigner, E. P. (1955). Lower limit for the energy derivative of the scattering phase shift. *Phys. Rev.*, 98:145–147. 45

[86] Yang, C.-J. (2016). Chiral potential renormalized in harmonic-oscillator space. *Phys. Rev. C*, 94:064004. 42

Appendices

A Regulator Effects

We can change regulator tailored to oscillator basis with cutoff (2.2) by varying either size of model space N or $\hbar\omega$. In this Appendix we consider different combinations of oscillator parameters $(N, \hbar\omega)$ that correspond to same ultraviolet cutoff i.e., we consider model spaces with combinations $N = 6$, $\hbar\omega = 26.63$ MeV, $N = 8$, $\hbar\omega = 22$ MeV, and $N = 10$, $\hbar\omega = 18.74$ MeV; all which have cutoff $\Lambda \approx 487$ MeV.

We start by comparing LO and NLO interaction in the three model spaces in Figure A.1. The curves in panel (a) are infrared-improved DVR implementation of LO function $v(k) = 1$ and in panel (b) we plot the same for NLO function $w(k) = k^2$. We note that LO and NLO functions in different model spaces have identical behavior at low-energy. This behavior of oscillator regulator is consistent with the expectation one has from EFT potentials. The differences only become visible at higher momenta as smaller N translate to less number of DVR points, leading to longer tails of infrared-improved potentials with decreasing N. It appears that different model spaces are basically equivalent to different regulators in momentum space. To confirm this we use the three oscillator regulators to compute $A = 3, 4$ nuclei at LO and NLO.

We begin by optimizing LO ${}^3S_1$ LEC to deuteron binding energy and ${}^1S_0$ LEC to scattering length a_s. Table A.1 shows the NN LECs optimized in different model space. The small variations at higher momenta in the interactions (that have same cutoff) reflect in small differences between the LO LECs; as expected from an EFT.

Similarly, we optimize the singlet and triplet S NLO LECs to deuteron binding and respective effective range expansion. Table A.2 show the values of NLO LECs that we get in different model spaces. We find that LECs have small differences which can be attributed to different regulators with same ultraviolet cutoff.

Now, we turn to NNN contact. As we discussed in the main text, there are two possible non-local regulators for NNN contact. We use make separate computations of $A = 3, 4$ in hyper-spherical and square regulators. We compare NNN contact in different model spaces when regulated in hyper-spherical oscillator basis in Figure A.2 which plots the function $\bar{u}(k, p)$ in Jacobi momentum space. Just like the case of NN potentials, all three oscillator

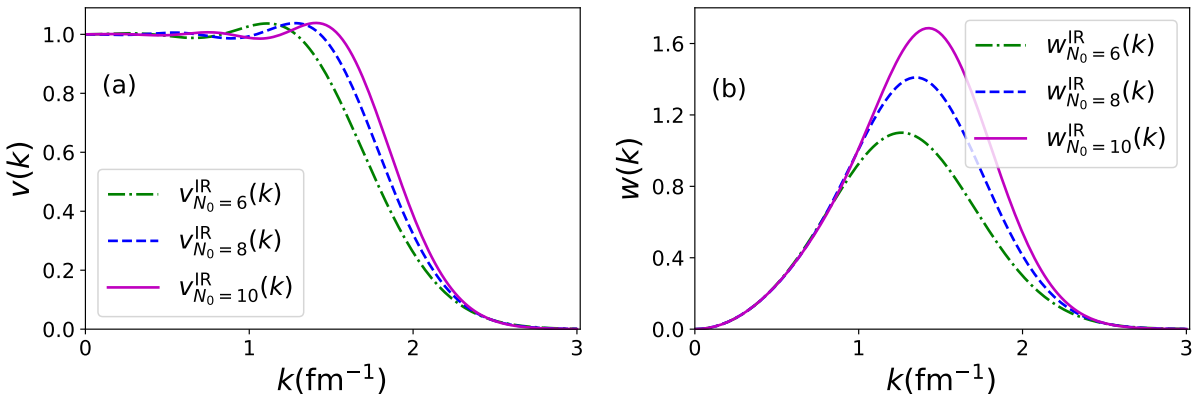

Figure A.1: (Color online) The dash-dotted green (solid magenta) curve shows the NN interaction in model space $N = 6, \hbar\omega = 26.63$ MeV, ($N = 10, \hbar\omega = 18.74$ MeV). The dashed blue curve shows the same interactions in model space $N = 8, \hbar\omega = 22$ MeV. Panel (a) and panel (b) correspond to NN interaction at LO and NLO, respectively. All three cases have a momentum cutoff $\Lambda \approx 487$ MeV.

regulator functions are similar are low momenta with slightly different tails. We find the same result holds for "square" NNN contact function as it is basically infrared-improved DVR implementation of $v(k) = 1$ in individual Jacobi momenta. In each case, we optimize NNN LEC to reproduce binding energy.

Table A.3 shows NNN contact LECs in different hyper spherical model spaces along with binding energy and radius for $A = 3, 4$ atomic nuclei at LO and NLO. Similarly, Table A.4 shows the same for NNN contact regulator with cutoff on each Jacobi momentum separately (We note that for square regulator truncation (2.50) is removed while performing the no-core shell model calculations).

In Tables A.4 and A.3, binding energy and radius results for ^{3,4}He nuclei have very similar results which one would expect from an EFT potential with same ultraviolet cutoff. The small differences, in going from model space $N = 6$ to 8, can be considered to be the effect of different regulators as at LO these variations are within LO EFT uncertainty estimate of 30% and at NLO within the expected 10%.

Table A.1: The LECs of the NN potential at LO for physical nuclei at constant $\Lambda \approx 487$ MeV and varying model space size.

N	$\hbar\omega$	$\tilde{C}_{^3s_1}$	$\tilde{C}_{^1s_0}$
6	26.63	-0.407880	-0.313361
8	22	-0.379465	-0.296100
10	18.74	-0.360988	-0.284491

Table A.2: NN LECs at NLO for physical nuclei at constant $\Lambda \approx 487$ MeV and varying model space size.

N	$\hbar\omega$	$\tilde{C}_{^3s_1}$	$C_{^3s_1}$	$\tilde{C}_{^1s_0}$	$C_{^1s_0}$
6	26.63	-0.792415	0.834806	-0.571535	0.469715
8	22	-0.809378	0.772254	-0.612966	0.691221
10	17.84	-0.798677	0.693435	-0.587451	0.614043

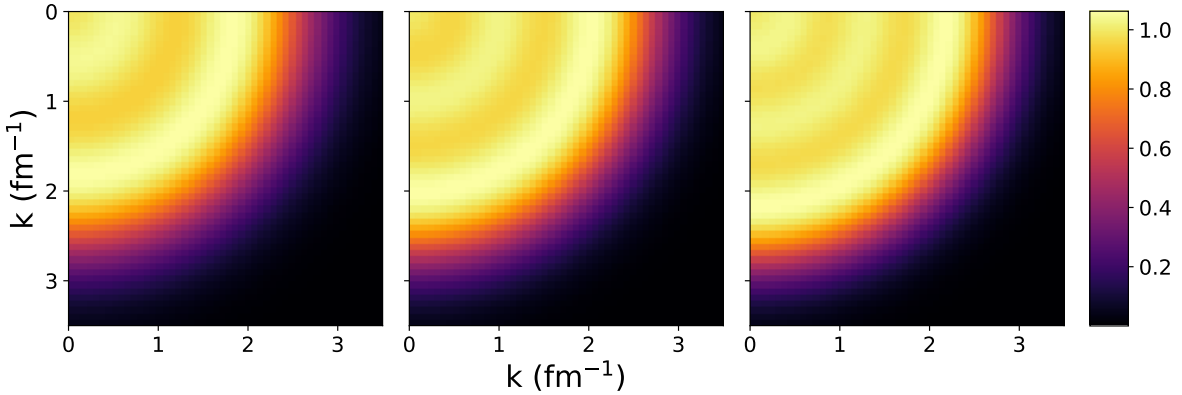

Figure A.2: (Color online) Momentum space matrix elements $\bar{u}(k,p) = c_{\mu,0}c_{\nu,0}u^{\mathrm{IR}}_{\mathrm{DVR}}\left(\sqrt{k^2+p^2}\right)$ in harmonic oscillator basis with $N = 6$ (left), 8 (center) and10 (right) with identical ultraviolet cutoff. The x and y axes represent Jacobi momenta in fm^{-1}.

Table A.3: Binding energies and radii for $A = 3, 4$ nuclei at constant $\Lambda \approx 487$ MeV and different model spaces employing a hyperspherical regulator for the NNN contact. The NNN coupling c_E is adjusted to reproduce the triton binding energy $B_t = 8.482$ MeV.

$E_{3\max} = N$ (hyper spherical)						
LO						
N	c_E	$r(^3\mathrm{H})$	$E(^3\mathrm{He})$	$r(^3\mathrm{He})$	$E(^4\mathrm{He})$	$r(^4\mathrm{He})$
6	-0.269308	1.30	7.55	1.47	18.28	1.45
8	-0.238514	1.29	7.52	1.46	17.66	1.46
10	-0.218702	1.28	7.50	1.45	17.27	1.46
NLO						
N	c_E	$r(^3\mathrm{H})$	$E(^3\mathrm{He})$	$r(^3\mathrm{He})$	$E(^4\mathrm{He})$	$r(^4\mathrm{He})$
6	-0.073289	1.58	7.71	1.77	28.39	1.36
8	-0.008170	1.63	7.77	1.83	29.30	1.44
10	-0.024851	1.63	7.77	1.82	27.90	1.51

Table A.4: Same as Table A.3 but for regulators in each Jacobi coordinate of the NNN force.

$E_{3\max} = 2N$ (square)						
LO						
N	c_E	$r(^3\mathrm{H})$	$E(^3\mathrm{He})$	$r(^3\mathrm{He})$	$E(^4\mathrm{He})$	$r(^4\mathrm{He})$
6	-0.224040	1.33	7.58	1.49	21.28	1.51
8	-0.191847	1.32	7.56	1.48	20.82	1.40
10	-0.171713	1.31	7.55	1.47	23.07	1.38
NLO						
N	c_E	$r(^3\mathrm{H})$	$E(^3\mathrm{He})$	$r(^3\mathrm{He})$	$E(^4\mathrm{He})$	$r(^4\mathrm{He})$
6	-0.059819	1.58	7.71	1.78	28.34	1.40
8	-0.006553	1.68	7.77	1.83	29.27	1.45
10	-0.020162	1.63	7.77	1.66	28.13	1.51

B Oscillator DVR with $k = 0$ DVR point

It is important to note that there exist many DVRs for the same finite oscillator basis. In our work, we used DVR basis formed by diagonalizing kinetic energy operator in finite oscillator basis. The projection of interaction using this DVR led to large oscillations, leading to wrong behavior of the original function at momenta smaller than lowest DVR point. This is a problem because in an EFT framework, the low-energy observables are dependent on the behavior of projected interaction at low momenta. In this Appendix, we seek an alternative to infrared improvement by developing an oscillator DVR for which $k = 0$ is a DVR point.

Using Eq. (2.9) and Christoffel-Darboux formula for orthogonal polynomials one gets,

$$\begin{aligned}\langle \phi_{\mu,l} | \phi_{\nu,l} \rangle &= c_{\mu,l} c_{\nu,l} \sum_{n=0}^{N_l} \tilde{\psi}_{n,l}(k_\mu, l) \tilde{\psi}_{n,l}(k_{\nu,l}) \\ &= c_{\mu,l} c_{\nu,l} \sqrt{(N_l+1)(N_l+l+3/2)} \times \\ &\frac{\tilde{\psi}_{N_l,l}(k_{\mu,l}) \tilde{\psi}_{N_l+1,l}(k_{\nu,l}) - \tilde{\psi}_{N_l+1,l}(k_{\mu,l}) \tilde{\psi}_{N_l,l}(k_{\nu,l})}{b^2 \left(k_{\mu,l}^2 - k_{\nu,l}^2\right)}. \end{aligned} \tag{B.1}$$

For $k_{\mu,l} \neq k_{\nu,l}$, the orthogonality condition implies,

$$\frac{\tilde{\psi}_{N_l+1,l}(k_{\mu,l})}{\tilde{\psi}_{N_l,l}(k_{\mu,l})} = \frac{\tilde{\psi}_{N_l+1,l}(k_{\nu,l})}{\tilde{\psi}_{N_l,l}(k_{\nu,l})}. \tag{B.2}$$

From Eq. (B.2) it follows that for every

$$\frac{\tilde{\psi}_{N_l+1,l}(k_{\mu,l})}{\tilde{\psi}_{N_l,l}(k_{\mu,l})} \equiv R, \tag{B.3}$$

we get a different discrete mesh of momenta, where R is a constant of our choice. Therefore, it is interesting to consider a DVR which has $k = 0$ DVR point i.e.,

$$R_0 = \frac{\tilde{\psi}_{N_l+1,l}(0)}{\tilde{\psi}_{N_l,l}(0)} = \sqrt{\frac{N_l + l + 3/2}{N_l + 1}} \tag{B.4}$$

To find remaining DVR points, we use,

$$\begin{aligned} 0 &= \sqrt{\frac{N_l + l + 3/2}{N_l + 1}}\tilde{\psi}_{N_l,l}(k) - \tilde{\psi}_{N_l+1,l}(k) \\ &= (N_l + l + 3/2)L_{N_l}^{l+1/2}(k^2b^2) - (N_l + 1)L_{N_l}^{l+1/2}(k^2b^2) \end{aligned}$$

Formula 8.971(4) from Ref. [35] simplifies above equation to give

$$L_{N_l}^{l+3/2}(k^2b^2) = 0 \tag{B.5}$$

Thus, $\kappa_0 = 0$ and the roots of the Laguerre polynomial $L_{N_l}^{l+3/2}(k^2b^2)$ constitute the $(N_l + 1)$ DVR points which we denote by κ_μ. We suppress the partial-wave dependence of DVR points in the notation here to keep equations simple.

Figure B.1 shows the two sets of discrete momenta in model space $N = 8, \hbar\omega = 22$, and $l = 0$. The dashed-dotted line denotes $R = 0$ and the dashed line represents $R_0 = \sqrt{(N_l + 1)/(N_l + l + 3/2)}$, where circles and triangles mark discrete momentum eigenvalues in each case, respectively.

Following Ref. [16], we find the normalization coefficients $d_{\mu,l}$'s (for $\mu = 0, 1, ..., N_l$) using orthonormality of discrete momentum eigenfunctions,

$$|\phi_{\kappa_\mu,l}\rangle = d_{\mu,l}\sum_{n=0}^{N_l}\tilde{\psi}_{n,l}(\kappa_\mu)|n, l\rangle. \tag{B.6}$$

It follows that,

$$
\begin{aligned}
d_{\mu,l}^{-2} &= \sum_{n=0}^{N_l} \tilde{\psi}_{n,l}^2(\kappa_\mu) \\
&= -\sqrt{(N_l+1)(N_l+l+3/2)}[\tilde{\psi}_{N_l,l}(\kappa_\mu)\tilde{\psi}'_{N_l+1,l}(\kappa_\mu) - \tilde{\psi}'_{N_l,l}(\kappa_\mu)\tilde{\psi}_{N_l+1,l}(\kappa_\mu)] \qquad \text{(B.7)} \\
&= \sqrt{(N_l+1)(N_l+l+3/2)}\tilde{\psi}'_{N_l,l}(\kappa_\mu)\tilde{\psi}_{N_l+1,l}(\kappa_\mu, l) \\
&= -\sqrt{(N_l+1)(N_l+l+3/2)N_l}\frac{\tilde{\psi}_{N_l-1,l+1}(\kappa_\mu)\tilde{\psi}_{N_l+1,l}(\kappa_\mu)}{\kappa_\mu b} \qquad \text{(B.8)} \\
&= (N_l+l+3/2)[\tilde{\psi}_{N_l,l}(\kappa_\mu)]^2 \qquad \text{(B.9)} \\
&= (N_l+1)[\tilde{\psi}_{N_l+1,l}(\kappa_\mu)]^2, \qquad \text{(B.10)}
\end{aligned}
$$

where, primes ($'$) denote derivate only of the Laguerre polynomial in the oscillator eigenfunctions in Eq. (2.6) (because other terms that arise from chain rule in Eq. (B.7) vanish). We use formulas 8.902(2), 8.971(2) of Ref. [35] and Eq. (B.5) to obtain equivalent form of $d_{\mu,l}$ in Eqns. (B.8), (B.9) and (B.10) where $\mu = 1, 2, ..., \mu$. It is important to note that one needs to solve for normalization coefficient $d_{0,l}$ seperately because $\kappa_0 = 0$ is not a root of Laguerre polynomial $L_{N_l}^{l+3/2}(k^2b^2)$. So, restarting from Eq. (B.7) we get,

$$
\begin{aligned}
d_{0,l}^{-2} &= \frac{2b^3(N_l+1)!(\kappa_0 b)^{2l}}{\Gamma(N_l+l+3/2)}\left(L_{N_l}^{l+1/2}(0)L_{N_l}^{l+3/2}(0) - L_{N_l-1}^{l+3/2}(0)L_{N_l+1}^{l+1/2}(0)\right) \\
&= \frac{2b^3\Gamma(N_l+l+5/2)(\kappa_0 b)^{2l}}{N_l!\Gamma(l+3/2)\Gamma(l+5/2)}. \qquad \text{(B.11)}
\end{aligned}
$$

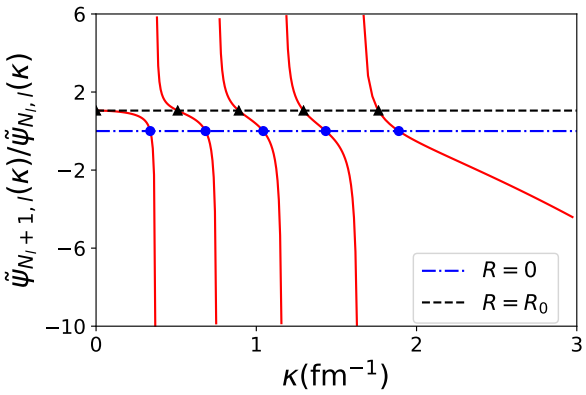

Figure B.1: (Color online) The ratio R of Eq. (B.2) as a function of the momentum in model space $N = 8$, $\hbar\omega = 22$ MeV, and $l = 0$. The dashed-dotted and dashed horizontal line corresponds to $R = 0$, and $R = R_0$, respectively. Their intersection with the red curve give DVR points in each case.

To derive the discrete momentum eigenfunctions in momentum space, we begin by using Christoffel-Darboux formula [35], i.e.,

$$\begin{aligned}
\phi_{\kappa_\mu,l}(k) &= d_{\mu,l}\sum_{n=0}^{N_l}\tilde{\psi}_{n,l}(\kappa_\mu)\tilde{\psi}_{n,l}(k)\\
&= d_{\mu,l}\frac{\sqrt{(N_l+1)(N_l+l+3/2)}}{(k^2-\kappa_\mu^2)b^2}\left(\tilde{\psi}_{N_l+1,l}(\kappa_\mu)\tilde{\psi}_{N_l,l}(k)-\tilde{\psi}_{N_l,l}(\kappa_\mu)\tilde{\psi}_{N_l+1,l}(k)\right)\\
&= d_{\mu,l}\frac{\sqrt{N_l+1}}{(k^2-\kappa_\mu^2)b^2}\tilde{\psi}_{N_l+1,l}(\kappa_\mu)\left(\sqrt{N_l+l+3/2}\tilde{\psi}_{N_l,l}(k)-\sqrt{N_l+1}\tilde{\psi}_{N_l+1,l}(k)\right)\\
&= d_{\mu,l}\frac{\sqrt{N_l+1}}{(k^2-\kappa_\mu^2)b}k\tilde{\psi}_{N_l+1,l}(\kappa_\mu)\tilde{\psi}_{N_l,l+1}(k),
\end{aligned}$$

where in step two and three we use Eqn. (B.4) and formula 8.971(4) of Ref. [35], respectively. Therefore, using Eqs. (B.10) and (B.11) we get,

$$\phi_{\kappa_\mu,l}(k)=\begin{cases}\frac{k}{(k^2-\kappa^2)b}\tilde{\psi}_{N_l,l+1}(k), & \text{if} 0<\mu\leq N_l\\ \sqrt{\frac{N_l!\Gamma(l+5/2)}{\Gamma(N_l+l+5/2)\Gamma(l+3/2)}}\sum_{n=0}^{N_l}\sqrt{\frac{\Gamma(n+l+3/2)}{n!}}\tilde{\psi}_{n,l}(k^2b^2), & \mu=0.\end{cases}$$

In Figure B.2 we see that the discrete momentum eigenfunctions $\phi_{\kappa_\mu,l}$ form a DVR for which $k = 0$ is a constituent of the discrete mesh in momentum space. Also, it is clear from

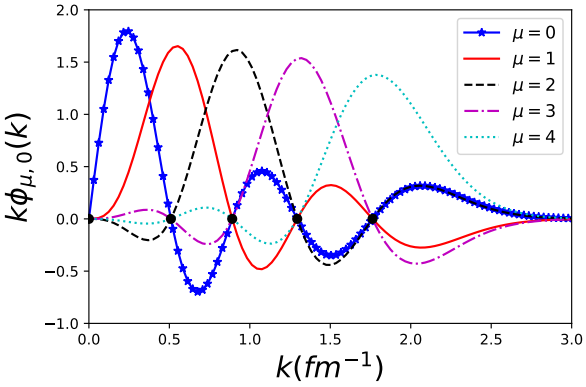

Figure B.2: The S wave eigenfunctions $\phi_{\mu,0}(k)$ of the squared momentum operator [plotted as $k\phi_{\kappa_\mu,0}(k)$] for $(\mu = 0, 1, ..., N_0)$ corresponding to discrete momentum eigenvalues for $R = R_0$, shown as a function of momentum. The solid black dots again indicate discrete momenta κ_μ in model space $N = 8$, $\hbar\omega = 22$ MeV, and $l = 0$. Clearly, $\phi_{\kappa_\mu,l}(k)$ form a DVR.

the figure that for $R > R_0$ one gets only N_l discrete momenta. For example, in the limit $R \to \infty$ the N_l solutions are zeros of Laguerre polynomial $L_{N_l}^{l+1/2}(k^2b^2)$. It is important to note that the remaining basis function is $\tilde{\psi}_{N_l+1,l}(k)$, but the resultant (N_l+1)-size basis is no longer a DVR. For $R = 0$ DVR (which we use in rest of our work), the DVR wave function for DVR momentum $k_{\mu,0}$ is a spherical bessel function $j_0(k_{\mu,0}r)$ which satisfies Dirichlet boundary condition at $r \approx L$ as $k_{\mu,0} \approx \mu\pi/L$. On the other hand for DVR discussed in this appendix i.e., $R = R_0$, we find that wave function $\phi_{\kappa_\mu,0}(r)$ corresponding to DVR point κ_μ approaches Neumann boundary condition at L where $\kappa_\mu \approx (2\mu + 1)\pi/(2L)$.

Now that we have the new DVR eigenvalues and eigenstates, we project the LO function $v(k) = 1$ and NLO function $w(k) = k^2$ using this DVR. The results are shown as solid red lines in panel (a) and panel (b), respectively of Fig. B.3, respectively. The coincide with the original momentum-space functions (shown by black dashed-dotted line) at solid dots representing the new discrete momenta (κ_μ) in model space $N = 8$, $\hbar\omega = 22$ MeV and $l = 0$. At $k = 0$ the projected interaction has correct value in the new DVR. Yet, the new DVR potential is more oscillatory, due to the wrong curvature at $k = 0$, in comparison to the infrared-improved DVR potentials shown as solid curves in Figs. 2.3 and 2.5.

Nevertheless, projected functions represent the original function $v(k)$ and $w(k)$ in comparison to DVR projected functions in the other DVR (shown by red dashed curves

in Figs. 2.3 and 2.5). Therefore, we continue to optimize S-wave LECs to effective range expansion at LO and NLO using DVR developed in this Appendix. Panel (a) (panel (b)) in Figure B.4 shows the LO and NLO np phase shifts from optimized interaction using new DVR in ${}^1S_0$ (${}^3S_1$) partial wave channel. As expected from the potential, at NLO we find small oscillations in phase shifts. So, it does not have as good an overlap with phase shifts from CD Bonn potential as we got earlier (in the main text) using infrared-improved DVR potential in the other DVR. Nonetheless, we find DVR with $k = 0$ point to be a promising alternative for infrared improvement.

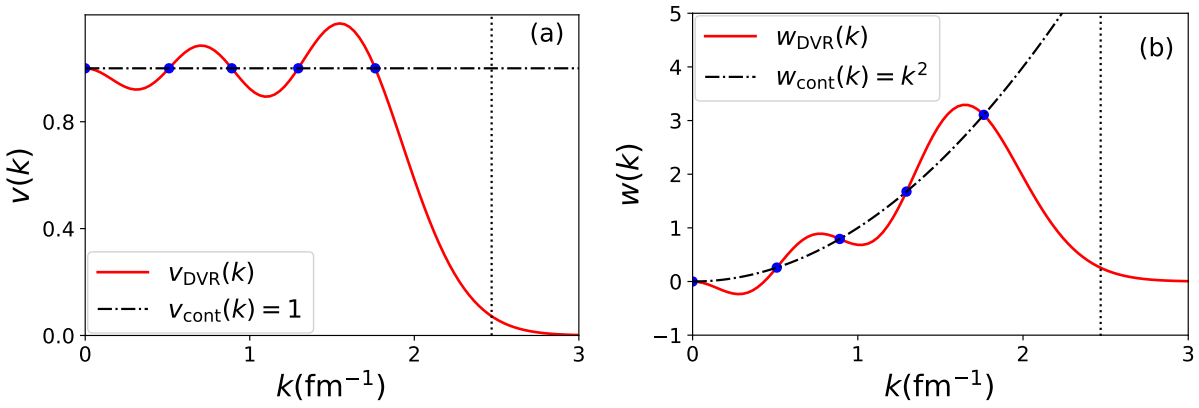

Figure B.3: (Color online) The red curve shows the contact realized in a DVR with a zero-momentum point, in comparison with the original momentum-space contact shown as a dashed-dotted black line. The solid dots represent the DVR momenta. Note that $k = 0$ is a DVR point. Panel (a) (panel (b)) is for NN LO (NLO) interaction in pionless EFT. The vertical black dotted line depicts the ultraviolet cutoff introduced by finite harmonic oscillator basis space $l = 0$, $N = 8$, and $\hbar\omega = 22$ MeV.

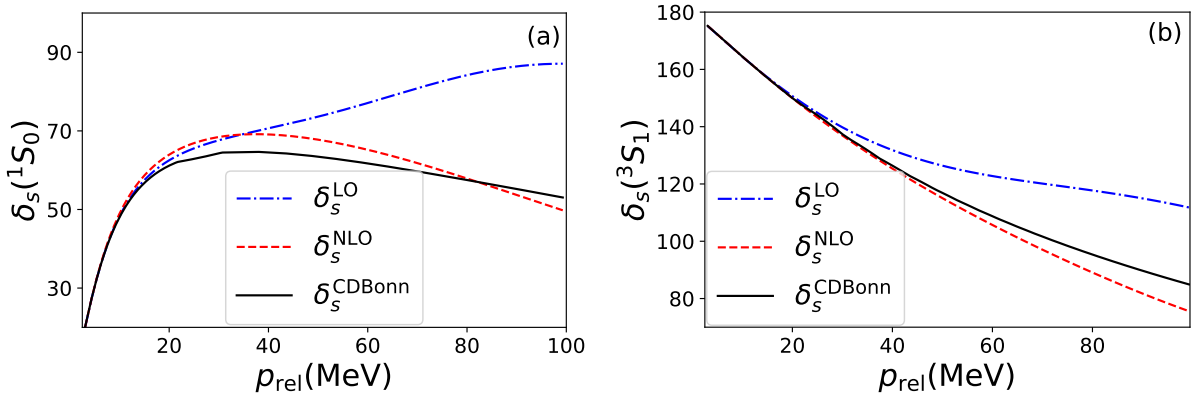

Figure B.4: (Color online) The $^1S_0$ (panel (a)) and $^3S_1$ phase shifts (panel (b)) from a DVR potential at NLO (LO) in pionless EFT in a model space $N = 8, \hbar\omega = 22$ MeV at NLO (red dashed line) and LO (blue dot-dashed line). The black curve shows the neutron-proton phase shifts of the CD-Bonn potential.

C Numerical solution to Lippmann Schwinger equation

We follow numerical implementation of partial Lippmann-Schwinger equation in Ref. [56] for the most part. In order to implement this, we begin with Gauss-Legendre quadrature

$$\int_{-1}^{1} dk f(k) \simeq \sum_{j=1}^{N} w_j f(k_j). \tag{C.1}$$

Here, $\{k_j; j = 1, 2, \ldots N\}$ are the N Gauss quadrature points, each weighted by w_j. For integration from -1 to 1, the quadrature points and weights are widely available. We make a linear transformation to map the known (k_j, w_j) to (p_j, w'_j)

$$p_j = \frac{1}{2}(B + A) + \frac{1}{2}(B - A)k_j, \tag{C.2}$$

$$w'_j = \frac{1}{2}(B - A)w_j, \tag{C.3}$$

to perform integration on the interval $[A, B]$ i.e.,

$$\int_{A}^{B} dp f(p) \simeq \sum_{j=1}^{N} w'_j f(p_j). \tag{C.4}$$

We rewrite principal part in a form which can be computed numerically,

$$\begin{aligned} T_l(p', p; E) &= V_l(p', p) + \frac{2}{\pi} \int_0^\infty dk \frac{k^2 V_l(p', k) T_l(k, p; E)}{E - E_k + i\epsilon} \\ &= V_l(p', p) + \frac{2}{\pi} \mathcal{P} \int_0^\infty dp \frac{k^2 V_l(p', k) T_l(k, p; E)}{E - E_k} - 2i\mu p_0 V_l(p', p_0) T_l(p_0, p; E) \\ &= V_l(p', p) + \frac{4\mu}{\pi} \int_0^\infty dp \frac{k^2 V_l(p', k) T_l(k, p; E) - p_0^2 V_l(p', p_0) T_l(p_0, p; E)}{p_0^2 - k^2} \\ &- 2i\mu p_0 V_l(p', p_0) T_l(p_0, p; E) \end{aligned} \tag{C.5}$$

In practice, we restrict the integration to a highest momentum Λ, such that it is much higher than the interaction cutoff of the nucleon-nucleus potential. This introduces the logarithmic term in the following steps.

We convert the integral equation into simultaneous set of linear equations by approximating the integral as a sum over N Gaussian quadrature points,

$$T_l(p,p_0) = V_l(p,p_0) \quad + \quad \frac{4\mu}{\pi}\sum_{j=1}^{N}\frac{w_j' p_j^2 V_l(p,p_j)T_l(p_j,p_0)}{p_0^2-p_j^2} - \frac{4\mu}{\pi}\Bigg[p_0^2\sum_{m=1}^{N}\frac{w_m'}{p_0^2-p_m^2} + \frac{1}{2}p_0\ln\Big(\frac{\Lambda+p_0}{\Lambda-p_0}\Big) - i\frac{\pi}{2}p_0\Bigg]V_l(p,p_0)T_l(p_0,p_0) \tag{C.6}$$

To compute differential cross-section, we need to compute phase shifts in each partial wave which is related to the on-shell matrix element $T_l(p_0,p_0)$. Thus, we need to solve half-off-shell $T_l(p_j,p_0)$ for all p_j, done by evaluating Eq. (C.6) for the $(N+1)$-size grid formed by,

$$p_i = \begin{cases} p_j, & j = 1,2,\ldots N \text{(quadrature points)} \\ p_0, & i = 0, \text{ momentum of the incident particle} \end{cases}$$

We define $V_l(p_i,p_j) \equiv V_l^{ij}$ and $V_l(p_i,p_0) \equiv V_l^i$. There are $N+1$ unknowns $T_l(p_i,p_0) \equiv T_l^i$ in the same number of linear equations, i.e,

$$T_l^i + \sum_{j=0}^{N} V_l^{ij} D_j T_l^j = V_l^j, \tag{C.7}$$

where,

$$D_i = \begin{cases} +2\mu\frac{2}{\pi}\frac{w_i' p_i^2}{p_i^2-p_0^2}, & i = 1,2,\ldots N \\ -2\mu\frac{2}{\pi}\Bigg[p_0^2\sum\limits_{j=1}^{N}\frac{w_j'}{p_j^2-p_0^2} + \frac{1}{2}p_0\ln\Big(\frac{\Lambda+p_0}{\Lambda-p_0}\Big) - \frac{\pi}{2}ip_0\Bigg], & i = 0 \end{cases}$$

Eq. (C.7) can be rewritten in the matrix form,

$$[F_l]_{N+1\times N+1}[T_l]_{N+1} = [V_l]_{N+1}, \tag{C.8}$$

where the matrix element $F_l^{ij} = \delta_{ij} + D_j V_l^{ij}$ (there is no implied sum over j), and $[T_l]$ and $[V_l]$ are column vectors. Thus, the solution for the column vector $[T_l]$ is

$$[T_l] = [F_l]^{-1}[V_l] \tag{C.9}$$

Vita

Aaina Bansal is the eldest of Sushil and Anju Bansal's two children. Her younger brother, Anurag, is an entrepreneur. She was born in Kaithal, Haryana, India. She graduated high school from Birla Balika Vidyapeeth (in Pilani, India), where she was deeply influenced by her Physics teacher. This pushed her to pursue Bachelor of Science (Honors) in Physics from University of Delhi. In Summer of 2019, Aaina earned a PhD in nuclear physics, after working as a doctoral student and research assistant in the Physics and Astronomy Department at the University of Tennessee, Knoxville (UTK). She joined UTK in 2014 as a graduate teaching assistant. In the Fall of 2015, Aaina joined Professor Thomas Papenbrock's research group which focuses on low-energy nuclear theory. As a member of this group, she worked on several projects involving effective field theories for nuclei and published findings in the peer reviewed journal Physical Review C. She was awarded 2018 Fowler-Marion Award in the Department.